Multichannel decay dynamics of Rydberg atoms and molecules

VRIJE UNIVERSITEIT

Multichannel decay dynamics of Rydberg atoms and molecules

ACADEMISCH PROEFSCHRIFT

ter verkrijging van de graad van doctor aan
de Vrije Universiteit Amsterdam,
op gezag van de rector magnificus
prof.dr. T. Sminia,
in het openbaar te verdedigen
ten overstaan van de promotiecommissie
van de faculteit der Exacte Wetenschappen \ Natuurkunde
op woensdag 30 mei 2001 om 13.45 uur
in het hoofdgebouw van de universiteit,
De Boelelaan 1105

door

Jan Bertus Marten Warntjes

geboren te Stadskanaal

Promotor: prof.dr. L.D. Noordam

Aan Adam,

'Want het daglicht wordt afgelost door de nacht,
maar de wijsheid wordt niet overmeesterd door de slechtheid.'

Wijsheid 7;30

Promotiecommissie:

dr. H.J. Bakker
prof.dr. W. Hogervorst
prof.dr. D.H. Parker
prof.dr. F. Robicheaux
prof.dr. S. Stolte
dr. M.J.J. Vrakking

Faculteit der Exacte Wetenschappen \ Natuurkunde.

The work described in this thesis was performed at FOM Institute for Atomic and Molecular Physics (AMOLF), Kruislaan 407, 1098 SJ, Amsterdam, the Netherlands. www.amolf.nl.

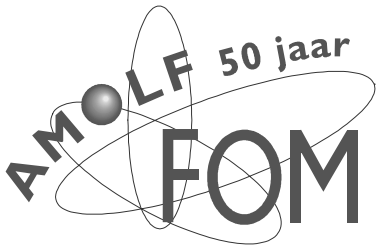

This work is part of the research program of the Stichting voor Fundamenteel Onderzoek der Materie (Foundation for Fundamental Research on Matter) and was made possible by financial support from the Nederlandse Organisatie voor Wetenschappelijk Onderzoek (Netherlands Organization for the Advancement of Research).

This thesis is based on the following publications:

Chapter 2 *Autoionizing Rydberg states of NO in strong electric fields.*
J.B.M. Warntjes, F. Robicheaux, J.M. Bakker and L.D. Noordam,
Journal of Chemical Physics **111**, 2556 (1999).

Chapter 3 *Measuring the predissociation and autoionization of the vibrationless Rydberg series in ammonia.*
J.B.M. Warntjes and L.D. Noordam,
Journal of Chemical Physics, submitted for publication.

Chapter 4 *Two-channel competition of autoionizing Rydberg electrons in an electric field.*
J.B.M. Warntjes, C. Nicole, F. Rosca-Pruna, I. Sluimer, M.J.J. Vrakking and L.D. Noordam, Physical Review A, accepted for publication (2001).

Chapter 5 *Stepwise electron emission from autoionizing magnesium Stark states.*
J.B.M. Warntjes, C. Wesdorp, F. Robicheaux, and L.D. Noordam,
Physical Review Letters **83**, 512 (1999).

Chapter 6 *Isolated core excitation in strong electric fields II: Experimental results in magnesium.*
J.B.M. Warntjes, C. Wesdorp, F. Robicheaux, and L.D. Noordam,
Physical Review A **62**, 033407 (2000).

Chapter 7 *Atomic spectral detection of tunable XUV pulses.*
J.B.M. Warntjes, A. Gürtler, A. Osterwalder, F. Rosca-Pruna, M.J.J. Vrakking and L.D. Noordam,
Optics Letters, submitted for publication.

chapter 8 *Atomic streak camera operating in the XUV.*
J.B.M. Warntjes, A. Gürtler, A. Osterwalder, F. Rosca-Pruna, M.J.J. Vrakking and L.D. Noordam,
Review of Scientific Instruments, submitted for publication.

In addition, the author participated in the following publications:

Slow photoelectron imaging.
Celine Nicole, Ingrid Sluimer, Florentina Rosca-Pruna, Marcel Warntjes, Marc Vrakking, Christian Bordas, Frederic Texier and Francis Robicheaux,
Physical Review Letters **85**, 4024 (2000).

Supersnelle meting van stapsgewijze elektronen emissie.
Marcel Warntjes, Kees Wesdorp, Francis Robicheaux en Bart Noordam,
Nederlands Tijdschrift voor Natuurkunde (NTvN), jaargang 65, 9, 266 (1999).

Contents

Chapter 1

Introduction.

1.1 Multichannel decay dynamics of Rydberg atoms and molecules.

The characteristic feature of a Rydberg atom or molecule is that there is at least one electron of the atom or molecule in a highly excited state. These Rydberg states can be described by quantum numbers of which the principle quantum number n is most important; n runs from 1 for the ground state to infinity for the ionic state where the electron is so far from its parent ion that it practically escaped. The study of Rydberg atoms and molecules is triggered by some amazing features of these systems. For example, their size: A typical ground state has dimensions in the order of Ångstroms (10^{-10} m), whereas in a Rydberg atom or molecule with, say, n =100, the electron has an outer turning point of its classical orbit at 1 μm. The classical roundtrip time of such an electron is 150 ps, well within reach of laboratory detectors. The weak interaction of the excited electron with its parent ion makes the Rydberg atom or molecule an excellent playground for experiments. Even relative small laboratory fields can influence the dynamics of Rydberg electrons significantly.

The dynamics and the decay of an excited electron can be described by multichannel quantum defect theory (MQDT). A channel is defined as a set of Rydberg states and the associated continuum, both having the same angular momentum and spin. The parent ion of one channel has a well defined eigenstate of electron configuration and, for a molecule, rotation and vibration. For the Rydberg states the energy E is negative, for the continuum E is positive. In the most simple system, a hydrogen atom, consisting of one proton and one electron, the dynamics of the excited electron can be calculated exactly. The electron potential is a Coulomb potential and the wavefunction has two independent solutions, $f(E, \ell, r)$ and $g(E, \ell, r)$, the regular and irregular Coulomb wavefunctions [1]. For hydrogen the energy of the Rydberg states is described by

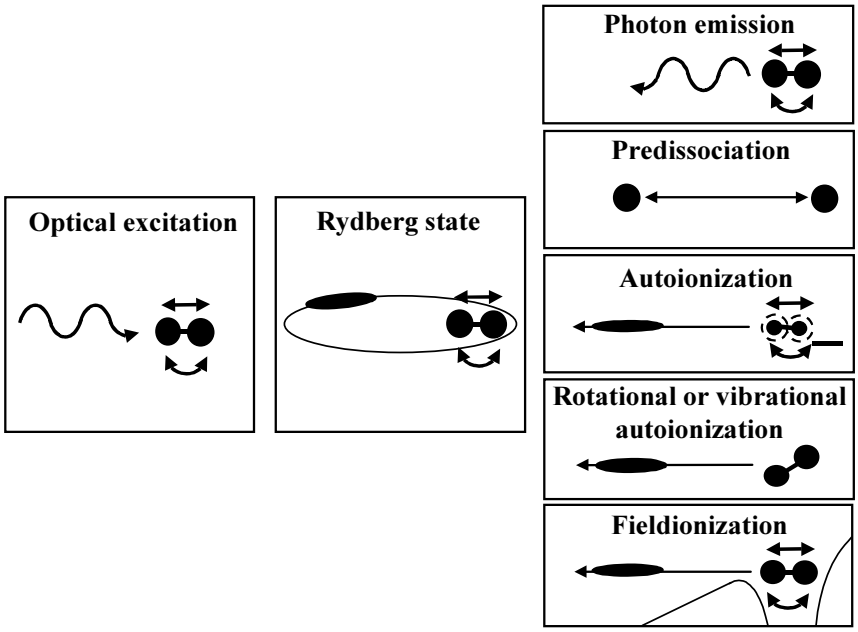

Figure 1.1: *After optical excitation of a diatomic molecule one electron is in a highly excited Rydberg state. There are five ways of decay relevant for this thesis: 1. The electron relaxes to a lower state under emission of a photon. 2. The electron transfers its energy to the core that fragments (predissociation). 3. The electron receives energy of an inner electron and autoionizes. 4. The electron receives rotational or vibrational energy of the molecular core and autoionizes. 5. The electron is pulled off the molecule with the help of an electric field.*

$$E = \frac{-1}{2n^2} \tag{1.1}$$

For any other atom it is only at a large distance from the ionic core that the potential of an electron in a Rydberg state is a Coulomb potential. Close to the core region the electron may penetrate the core and will experience a different potential, usually deeper than that of a single proton. The effect of the deeper potential is that the reflected electron wave has a phase shift as compared to the phase of the wave, scattered off a proton. This phase shift is described by the quantum defect δ. A solution of the standing wave function in an atom is given by:

$$\Psi = \frac{1}{r}\left[f(E,\ell,r)\cos\pi\delta + g(E,\ell,r)\sin\pi\delta\right] \tag{1.2}$$

a superposition of the regular and irregular Coulomb wavefunctions with a phaseshift $\pi\delta$. The phase shift of the electron wave, or else, the quantum defect causes the

eigenstates in a channel to shift in energy as compared to the hydrogen eigenstates. In an atom the energy levels are shifted as compared to hydrogen with the quantum defect δ_ℓ:

$$E = \frac{-1}{2(n-\delta_\ell)^2} \tag{1.3}$$

where δ_ℓ is constant for each angular momentum wave ℓ. Note that high angular momentum waves do not penetrate the core and will be similar to hydrogen ($\delta_\ell \cong 0; \ell \geq 5$).

The core of an atom or molecule not only causes a phase shift of the electron wave but also couples the wave's channel to other channels. In order to unravel the dynamics of an excited electron one tries to find the relevant channels where the electron has a non-zero excitation amplitude and the channels that are coupled to them. Some of these channels form bound states at the excitation energy, the closed channels, others are in the continuum at the excitation energy, the open channels. The latter channels are responsible for the decay of the excited electron. The coupling between channels only occurs at the core: The electron approaches the core after a round trip and scatters, partly back into its original orbit, partly into the open decay channels.

In Fig. 1.1 the various decay channels of an highly excited molecule are schematically addressed. After optical excitation the electron is in a Rydberg state. The excited electron can loose its energy by emission of a photon. This radiative decay sets an upper limit to its lifetime. This limit is not so severe, since radiative decay is improbable, in the order of 10^{-7} per electron round trip. If the electron donates its energy to its ionic core, the molecule may fragment; this decay mechanism is known as predissociation. For the other three decay channels the electron absorbs a little extra energy after which it escapes the ionic core. If the extra energy is taken from the inner electrons the mechanism is called autoionization, energy from rotational or vibrational motion of the molecular core leads to rotational or vibrational autoionization and finally an applied laboratory field can pull the electron of the core. In an atom there is of course no predissociation and rotational or vibrational autoionization.

Note that the decay pathways can also proceed in the reverse direction; a free electron interacts with an ion to recombine to a highly excited state. This state still has positive energy and hence a very short lifetime unless some energy is directed elsewhere. The reverse decay pathways of Fig. 1.1 are photoexcitation, associative recombination, dielectronic recombination, rotational and vibrational recombination and field-enhanced recombination.

In this thesis one or two electrons are excited in a controlled way. If the electron decays, it may follow various decay channels. All these decay channels compete and result in complicated, yet fascinating dynamics. It is the aim of this thesis to investigate the dynamics of the Rydberg electron as it is influenced by the coupling of all relevant channels.

1.2 Frequency versus time domain studies.

The dynamics of a Rydberg atom or molecule can be investigated in the frequency or in the time domain. These ways of detection are complementary. This will be explained with a two-level, two-channel atom. Imagine an atom with a closed channel having two states with energy E_1 and E_2 and an open channel with a continuum around that energy. If the atom is exited from the ground state with a short laser pulse with a spectrum that straddles the two states in the closed channel, both states are coherently excited. The phase of the wavefunction of a state i evolves with a frequency $\omega_i = E_i/\hbar$, where $\hbar$ is Planck's constant divided by 2π. Hence, the time dependent amplitude of the wavefunction $\phi_i(r,t)$ at the core is $a_i \exp(-iE_i t/\hbar)$ where a_i is the initial excitation amplitude of level i. Since both states are coherently excited, they form a wavepacket. The two-level wavepacket $\Psi(t)$ is described by

$$\Psi(r,t) = \sum_i a_i \phi_i(r,t) = a_1 e^{-iE_1 t/\hbar}\phi_1(r) + a_2 e^{-iE_2 t/\hbar}\phi_2(r) \tag{1.4}$$

If we assume that the excitation amplitude is equal, $a_1 = a_2$, the electron density at the core (defined as $|\Psi(0,t)|^2$) fluctuates. The minimum electron density at the core is zero, when the wavepacket is somewhere in an orbit around the nucleus. The maximum electron density at the core is $4a^2$, when the wavepacket has returned to the core. The electron density fluctuates with the beat frequency $\omega_2 - \omega_1$ imposed by the energy difference of the two levels.

Now suppose the two-level system is coupled to the continuum of the open channel. An electron can only autoionize via scattering off the core. Scattering occurs only when there is density at the core and one expects electron emission in the continuum with the same period as the beating frequency between the two states. The electron emission yield thus depends on both the electron density at the core and the scattering probability into the open channel.

How to detect electron decay dynamics of such a two-level system in practice? There are two ways of approach: Detection in the time domain and detection in the frequency domain. For a detection in the time domain we excite the atom with a short laser pulse. The bandwidth of the pulse is larger than the spacing of the two states. As explained, in this way a wavepacket is created that autoionizes with the beat frequency. The electron emission of the atom is monitored in time after the excitation. The complementary approach is excitation of the atom with a long, narrowband laser pulse, while detecting the total electron emission. By scanning the laser frequency we find the energy and the width of the two states. Fourier-transformation of such a frequency spectrum yields the electron density at the core. Using both ways enables us to combine the knowledge of electron density at the core with the electron emission so that we gain information about the scattering of an electron of the core. Throughout this thesis we will make use of both approaches.

The challenge in detecting electron emission in time is that the time scales of the atom are extremely short. Therefore, the streak camera [17] has been developed to

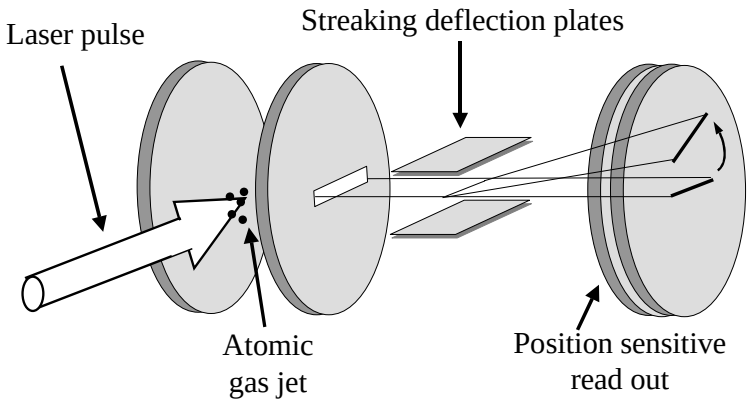

Figure 1.2: *A schematic drawing of the streak camera. Atoms are ionized by a laserpulse between two electrically charged plates. Electrons are accelerated towards a set of multichannel plates and a phosphorscreen which is viewed by a CCD camera. In the electron trajectory two deflection plates change field rapidly to convert arrival time of the electrons at the deflection plates into a position coordinate on the CCD image.*

be able to detect electron emission from an atomic or molecular system even on a picosecond (10^{-12} s) time scale. A schematic picture of the camera is drawn in Fig. 1.2. A laser pulse excites the atoms in a gas jet inside an interaction region between two electrically charged plates. Electrons that are released will be accelerated towards a position sensitive read out (a set of multichannel plates and a phosphorscreen, viewed by a CCD camera). In the trajectory of the electron two streaking deflection plates are placed. The field between these deflection plates is rapidly switched from a positive to a negative value perpendicular to the direction of the electrons. In this way the arrival time of an electron at the deflection plates is converted to a position coordinate on the read-out. Hence the height on the read-out relates to the emission time in the interaction region. Actually the signal is not a point, but a line of electrons that passes through a slit in the acceleration plates. Because of the finite speed of light, this line exhibits a slant upon deflection. A more detailed explanation of the slope of the signal line is given in chapter 8. The slope is useful, since it offers a calibration of the apparatus. The temporal resolution is around 1 ps, but depends on a number of experimental parameters such as the excitation volume, the acceleration field, the excess kinetic energy of the electrons and the voltage ramp on the deflection plates.

A dedicated circuit has been designed to make the streaking deflection plates switch fast. The circuit is explained in detail in the appendix. In short, one of the deflection plates is on ground, the other is positively biased. A laser pulse triggers a photosensitive switch that discharges a negatively charged capacitor. This creates a fast voltage ramp between the two deflection plates. The voltage ramp is determined by the residual resistance and self inductance of the streak circuit. Typical values are +900 V to -

1200 V in 300 ps. Actually the ramp can be faster but this creates problems with the uniformity of the deflection field. By carefully delaying the trigger pulse compared to the excitation pulse, the ramp can be applied at the very moment that the electrons from the interaction region pass the deflection plates.

1.3 Outline of this thesis.

The physicist's approach to a complex problem is to solve a simple problem and perturb that system such that it approaches the complex one. As we have seen, in atomic physics one starts with the solution of the dynamics of an excited electron that orbits around a proton; the hydrogen atom. Placing hydrogen in an electric field changes the dynamics of the electron, but this can still be mathematically solved. For all other elements this is no longer true, but we can regard the atom as a hydrogen atom with a core that can scatter the electron into other channels.

This thesis is divided into three parts:

In the first part, the hydrogen model is stretched further by replacing the proton by a small, closed shell, molecular ion. Even though a molecular ion is far more complicated than a simple proton, the dynamics of the highly excited electron can still be understood by imagining the molecular ion as an atomic ion. Additionally the molecular core can donate rotational or vibrational energy to the electron or absorb all the electronic energy for predissociation. We unravel the competition of these decay channels with fieldionization in chapter 2 with nitric oxide and in chapter 3 with ammonia.

In the second part, we consider an atomic ion with no closed shell structure. Solving the dynamics of an excited electron that interacts with the hole it leaves behind in the closed shell upon excitation is regarded in chapter 4: The competition between fieldionization and autoionization in xenon is explained both with full quantum calculations and a simple, intuitive picture, developed in chapter 2 and 3. Finally, the most challenging problems, involving two interacting electrons and a core, will be addressed in chapter 5 and 6 where an highly excited electron in magnesium interacts with the subsequently excited inner, isolated core electron.

In the third and final part of this thesis, the acquired knowledge of atoms under the influence of laser pulses is used to measure the temporal and spectral profile of the laser pulses themselves. In chapter 7 the photoionization cross section of neon as a function of an electric field is used to retrieve the spectrum of an XUV pulse. In chapter 8 neon is used as a fast photocathode with no inherent energy spread to detect the temporal profile of an XUV pulse.

'And still we stayed near the waves
and dreamed like the man who wants to travel,
whose heart is on the way, though his feet linger.'

Dante Alighieri, Divina Commedia, Purgatorio.

Part 1

The excited electron coupled to a molecular core.

The dynamics of a highly excited electron can be understood by assuming that the electron is making large orbits around a point like charge. If the point like charge is a proton, the dynamics can be mathematically solved. In case of an electron with an atomic ion, the energies of the excited electron change as compared to the energies in hydrogen. Can this model be stretched further and is it applicable for molecules? The molecular core is far more complicated than the atomic core because it has rotational and vibrational energies that can be exchanged with the electron. In the following two chapters frequency-resolved photoionization spectra are taken of nitric oxide and ammonia in an electric field. These molecules have a closed shell molecular core with one valence electron. It turns out that the spectra are reminiscent of multiple atomic spectra, shifted compared to each other with the rotational energy spacing of the molecular core. Moreover, close to the saddlepoint, induced by the electric field, the lifetime of the excited electron becomes comparable to the typical times of predissociation and rotational autoionization. These latter processes can quench the photoionization yield. For both molecules qualitative equations are derived to understand the overall photoionization yield as a function of excitation energy.

Chapter 2

Autoionizing Rydberg states of NO in strong electric fields.

An investigation on autoionization of Rydberg electrons of the nitric oxide molecule in strong, static electric fields is reported. The excitation is done via various rotational states of the $A^2\Sigma^+$ intermediate state (v' = 0) and with polarization parallel or perpendicular to the electric field. The splitting of the autoionizing Rydberg states into overlapping Stark manifolds is resolved for excitation above the saddlepoint created by the field. We observe that the competing decay between photoionization and predissociation can lead to an incorrect interpretation of threshold energy. The photoionization spectrum of NO Rydberg series attached to various rotational thresholds are very similar owing to weak rotational coupling. The experimental results are accurately simulated by quantum calculations based on MQDT. A more intuitive formulation of the average behavior of the photoionization cross section is developed that accounts for the suppression of ionization near the threshold due to competing predissociating channels.

2.1 Introduction.

An optical pulse can pump the outer electron of an atom or molecule towards quantized, highly excited states, so-called Rydberg states, with energies described by the Rydberg formula E = IP - 1/2(n-μ)^2 (in atomic units), where IP is the ionization potential, n is the principle quantum number ranging from one to infinity and μ is the quantum defect [1]. The classical outer turning point of the electron orbit of such a Rydberg state is rather large (for instance 660 Å for $n = 25$, $\ell = 0$; 800 times the internuclear distance of the diatomic molecule NO) and the time it takes to complete the orbit is relatively long (2.4 ps for $n = 25$; the same time scale as the lowest rotations of the NO core). Upon applying a static electric field to the system, the Rydberg levels experience a Stark splitting and the angular momentum of the orbiting electron is no longer conserved. Hence, in addition to the oscillation along the radial coordinate, there is also an oscillation in the angular momentum of the electron between $\ell = 0$ up to $\ell =$

n - 1 and back. For $n = 25$ with a field strength of 1 kV/cm the angular momentum period is 10.4 ps. In that case, the electron makes about four radial oscillations during one complete angular oscillation.

A simultaneous effect of the electric field is a suppression, in the opposite direction of the field, of the Coulomb potential experienced by the outer electron. In this direction the electron can escape over the created saddlepoint with a lower energy than in zero-field. In fact, at a field strength of 1 kV/cm the potential is suppressed so much that the $n = 25$ Rydberg level, in zero-field bound by 176 cm^{-1}, can classically escape over the saddlepoint (field-induced autoionization). For the NO molecule the time scale on which this electron emission process takes place is on the same order as fragmentation of the core (predissociation). Each time an electron returns to the ionic core there is a probability that it scatters and autoionizes and there is a probability that the energy of the electron is transferred back to the core leading to fragmentation into a neutral nitrogen and oxide atom.

In addition to autoionization and predissociation, coupling of the electron to the molecular core can lead to an exchange of core rotational or vibrational energy to the electron. We refer to the case that the Rydberg electron gains rotational or vibrational energy sufficient to escape the ionic core as rotational or vibrational autoionization respectively.

In order to unravel the influence of the various decay mechanisms of Rydberg electrons in a static electric field we monitor the photoionization of NO at various field strengths. Nitric oxide has been selected as an example to study these dynamics, since the molecule has a convenient and established laser excitation scheme. The excitation pathway is schematically depicted in Fig. 2.1. The molecule is excited from the $^2\Pi$ ground state via a selected rotational state of the $A^2\Sigma^+$ intermediate state (v' = 0) to the Rydberg series. A static electric field is present that lowers the potential energy of the Rydberg electron in the direction of the field. The photoionization yield is monitored as a function of excitation frequency of the second laser step.

2.2 Theory.

In this section we will describe the full MQDT calculations that give excellent agreement with the observed spectra. However, we will begin with the physical mechanisms starting from a hydrogen atom in a static electric field.

2.2.1 Influence of a static electric field.

A static electric field has various effects on a molecule. As mentioned already it creates a suppression of the Coulomb potential of the molecular core in the direction of the field. The potential energy of the Rydberg electron, when far from the core, can be described as the sum of the Coulomb potential and the potential created by the a field

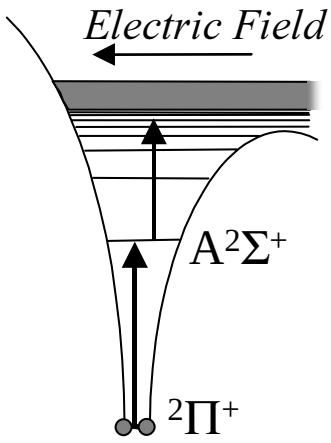

Figure 2.1: *Excitation scheme of nitric oxide in a static electric field. The molecule is excited with 1 + 1' REMPI from the* $^2\Pi$ *ground state via the* $A^2\Sigma^+$ *intermediate state to the Rydberg series. The static electric field lowers the potential energy of the Rydberg electron on one side.*

strength F pointing in the direction z:

$$E = \frac{-1}{|r|} - Fz \tag{2.1}$$

The Coulomb potential is raised on one side and lowered on the other by the electric field. The energy of the local maximum on the lowered side (the saddlepoint) as a function of field strength F is then:

$$E = -\alpha\sqrt{F} \tag{2.2}$$

with $\alpha = 2$ in atomic units, or $\alpha = 6.12$ cm^{-1} if the field is given in V/cm.

In a typical photoionization measurement the photoelectron yield is detected as a function of excitation energy. One would expect a signal with a stepfunction-like appearance: no signal below the saddlepoint and electron autoionization yield from the quantized states above the saddlepoint [18]. The threshold can, in a series of such measurements, be tracked as a function of field strength yielding the experimental value of α.

Another effect of a static electric field F is that it breaks the conservation of angular momentum of the Rydberg electron or, equivalently, the n-fold degeneracy of a Rydberg state n is lifted and splits into a Stark manifold of n separate k-states. The energy of the Rydberg Stark states to lowest order in the field strength F is:

$$E = \frac{-1}{2n^2} + \frac{3}{2}Fnk \tag{2.3}$$

where the quantum number k runs from (n - 1, n - 3 .. - n + 1) for the azimuthal angular momentum $m = 0$. The states that increase in energy compared to the zero-field value (positive k) are called blue states; those that decrease in energy (negative k) are called red states. Note that above the saddlepoint energy the manifolds of adjacent n always overlap because the spread in energy of the manifolds is so large.

So far these consideration are general for atoms and molecules. Molecules have internal degrees of freedom, and each of these rotations and vibrations have their own Rydberg series, hence we have to consider a far larger number of states than for atoms. The rotational series are separated by the rotational energy E_{rot} which is given in first order for Hunds case b (intermediate Σ state) and case d (Rydberg state) by:

$$E_{rot} = BN(N+1) \tag{2.4}$$

with B the rotational constant and N the rotational angular momentum of the molecular core (note: we use N' for the $A^2\Sigma^+$ state and N^+ for the ionic state). Throughout these experiments, we excite Rydberg series attached to the lowest rotational states of the zeroth vibration of NO. In a static electric field where every Rydberg level splits up into n k-states the system is more prone to accidental degeneracy of states of different rotation leading to a coupling of several rotational series. These arguments are well known from ZEKE spectroscopy [6]. Series that couple to continuum states, either directly, or via lower rotational series induce rotational autoionization [20–23].

The Rydberg series in NO and their lifetimes and couplings are quite well known [27–33]. Also other decay channels like predissociation are reported [24–28]. However, important features of Rydberg electrons in a strong electric field have received little attention.

2.2.2 Quantum calculation of the photoionization spectra.

We have based our simulations of the photoionization spectra of NO in a static field on the multichannel Stark theory [34]. This formulation uses the WKB treatment of the Stark problem to describe alkali atoms in static electric fields [35], in order to include the possible exchange of energy and angular momentum between the Rydberg electron and the molecular ion core. Our formalism is very similar in spirit to the treatment presented in Ref. [36] but also allows the calculation of the partial excitation amplitudes into all of the channels enabling us to distinguish between the photoionization and photodissociation channels in our calculation.

The treatment in Ref. [34] uses a separation of quantum numbers into those appropriate in zero field and those appropriate in an electric field. The reason for this separation is that when the Rydberg electron is near the ion (within 10-20 Bohr radii) the static field plays no role compared to the electron-ion interaction. Within this small volume, complicated molecular processes can occur (coupling between different rotational and vibrational channels and between Rydberg channels and predissociation channels), but these processes are completely unaffected by the field. Thus, field-free channel couplings (parameterized by K-matrices) and dipole matrix elements can be

used to describe the small r behavior of the Rydberg electron. When the electron is further out than 10-20 Bohr radii from the ion, the potential is nearly identical to that of a H atom in a static field. We neglected any long-range interactions. In this outer region, the electron moves in uncoupled channels in parabolic coordinates. It is the connection between these two regions that gives the full wavefunction and allows us to obtain the full multichannel wave function in the field.

Another, more practical, reason for the separation of quantum numbers is that the formulation distinguishes between the channels which have non-zero scattering and those which have roughly zero scattering in zero field. Since the channels that do not have scattering (i.e. quantum defects that are effectively zero) behave like H, we can account for them implicitly without the need for including them in our matrix manipulations. This substantially improves the efficiency of the calculation which is important because it is necessary to calculate the cross sections at 16,000 to 32,000 different energies for many different field strengths and initial states.

We will sketch the series of transformations that connect the wavefunction across different regions of space where different physical processes dominate. Let the parameter γ indicate all of the zero-field channels that have non-zero K-matrix elements (i.e. these are the channels for which the Rydberg electron experiences non-Coulombic potential). In general, γ describes five quantum numbers and for this molecular situation

$$\gamma = \{v, N^+, M_N, \ell, m\} \tag{2.5}$$

where v is the vibrational state of NO which is 0 for the cases we investigated, N^+, M_N are the total and z-component of all nuclear angular momenta, and ℓ, m are the orbital angular momentum and the z-component of the orbital angular momentum for the Rydberg electron. Note there is no coupling between states for which $M_N + m = M_{tot}$ changes.

The quantum numbers in the field have a form similar to those in zero field. We define the parameter $\tilde{N}$ to be the quantum numbers in parabolic coordinates,

$$\tilde{N} = \{v, N^+, M_N, n_1, m\} \tag{2.6}$$

which are similar to the γ quantum numbers but with the angular momentum of the Rydberg electron replaced with the quantum number in the electric field, n_1, which is the number of nodes in the up-potential parabolic coordinate.

The formulation of Robicheaux in Ref. [34] is general in the sense that it applies equally well to atoms or molecules in an electric field. The field dependent transformation between spherical and parabolic coordinates and the field dependent phases are independent of the short range interactions between the atomic or molecular ion and the Rydberg electron. The only input into the Stark calculations that distinguish between different ions are three kinds of body frame parameters: the zero field threshold energies, the zero field K-matrices in the g quantum numbers and the zero field dipole matrix elements in the γ quantum numbers. In Table I are the last two body

frame parameters we used in the calculation. For single channels the K-matrices are $\tan(\pi\mu)$ with the quantum defects μ taken from Ref. [28]. The $\ell = 0$, $\Lambda = 0$ and $\ell = 2$, $\Lambda = 0$ channels are coupled in the body frame; for these two channels, the K-matrix is given as K_{ss} and K_{sd} in the first row and K_{ds} and K_{dd} in the second row. To obtain the lab frame parameters we use the frame transformation applied to molecular rotations [37, 38].

The frame transformation from the body frame to the (zero-field) lab frame is not sufficient to obtain quantum numbers in the form γ of Eq. (2.5) The transformation gives the channel couplings in terms of the quantum numbers $\{v, N^+, \ell, J, M\}$, where J is the total angular momentum and M its z-component. We need to separate the total angular momentum J into the nuclear rotational angular momentum and the angular momentum of the Rydberg electron. This is accomplished through one last recoupling that uncouples the N^+ and ℓ angular momenta. The unitary matrix that performs this recoupling is simply a Clebsch-Gordon coefficient:

$$\langle JM|\, M_N, m\rangle = \left\langle N^+ M_N \ell m \right|\, N^+ \ell J M\} \tag{2.7}$$

After this sequence of recouplings, the K-matrices and dipole matrix elements have the correct form.

There is one last important ingredient that still needs to be incorporated. This is the possibility that the electron can be converted from its nearly free Rydberg character into a tightly bound electron in a predissociating orbital. Thus each time the electron returns to the region near the nucleus there is an ℓ dependent probability that it will be captured and disappear in a predissociating channel. We include this effect by extending the zero field K-matrix so that each channel is coupled to an open channel with a strength that reproduces the zero field predissociation rate. The electric field does not affect these extra channels so they are treated as completely open in our formulation. This channel provides extra width to each resonance and causes a reduction of the photoionization cross section since the predissociation is another pathway for decay.

1	Λ	K	K	D
0	0	0.395	-0.459	0.0
2	0	-0.459	0.223	0.0
1	0	-1.342		1.3
1	1	-1.058		1.0
2	1	-0.168		0.0
2	2	0.287		0.0

Table 2.1. *Body frame parameters for NO. l is the orbital angular momentum of the Rydberg electron, Λ is the projection of the angular momentum on the internuclear axis, K are the K-matrix elements, and D are the dipole matrix elements. The $\ell = 0$, $\Lambda = 0$ and $\ell = 2$, $\Lambda = 0$ channels are coupled in the body frame and the K-matrix is given as K_{ss} and K_{sd} in the first row and K_{ds} and K_{dd} in the second row.*

2.3 Overall behavior of the photoionization cross section.

To focus on the overall, average shape of the photoionization spectrum, including the dramatic effect of predissociation, we assume that the Stark spacing between Rydberg states of one manifold are not resolved. The basic idea is that by averaging over the Stark spacing almost all of the quantum standing wave behavior is lost. Therefore, the amount of flux into the ionization channel or detachment channel can be found by investigating how much each partial wave scatters into each channel. This works because on average the partial waves are equally populated over the energy range and they each scatter independently; for some Stark resonance states, the partial waves scatter constructively but for other states they scatter destructively so that on average they behave as if they scatter independently. The average photoionization cross sections, modified due to the competing mechanism of predissociation, can give accurate information about dissociation rates of Rydberg states.

We will treat the simplest situation in detail; the extension to more complex situations is straightforward (see chapter 3). The probability for direct electron ejection down potential depends on the function:

$$\Phi_{\ell m}(\cos\theta_s) = 2\pi \int_{-1}^{\cos\theta_s} |Y_{\ell m}|^2 d\cos\theta \tag{2.8}$$

where θ_s is the maximum escape angle of the electron with respect to the direction of the field (the -1 direction), ℓ is the angular momentum of the Rydberg electron and m its projection on the field axis [1]. We assume that the initial excitation to the Rydberg state is mainly into one partial angular momentum wave, ℓ_0. The probability for the direct ejection of the electron from the molecule is

$$\eta = \Phi_{\ell_0 m}(\cos\theta_s) \tag{2.9}$$

The remaining fraction 1-η is bound but can still ionize by scattering of the molecular core. We define the branching ratio for ionization, $B_{\rm FI}$, as the probability for the bound electron to elastically scatter into the open region of space, $S_{\rm FI}$, divided by the sum of the probabilities to elastically scatter into the open region $S_{\rm FI}$ and to scatter

[1] For the lowest ℓ's the explicit form of $\Phi_{\ell m}(\cos\theta_s)$ is:
$\Phi_{00}(\cos\theta_s) = \frac{1}{2}(1+\cos\theta_s)$
$\Phi_{10}(\cos\theta_s) = \frac{1}{2}(1+\cos^3\theta_s)$
$\Phi_{11}(\cos\theta_s) = \frac{1}{2}(1+\frac{3}{2}\cos\theta_s - \frac{1}{2}\cos^3\theta_s)$
$\Phi_{20}(\cos\theta_s) = \frac{1}{2}(1+\frac{5}{4}\cos\theta_s - \frac{5}{2}\cos^3\theta_s + \frac{9}{4}\cos^5\theta_s)$
$\Phi_{21}(\cos\theta_s) = \frac{1}{2}(1+\frac{5}{2}\cos^3\theta_s - \frac{3}{2}\cos^5\theta_s)$
$\Phi_{22}(\cos\theta_s) = \frac{1}{2}(1+\frac{15}{8}\cos\theta_s - \frac{5}{4}\cos^3\theta_s + \frac{3}{8}\cos^5\theta_s)$
The Φ_{10} and Φ_{11} are used for the one-photon excitation in NO in this chapter and for NH_3 in chapter 3. The Φ_{20} and Φ_{22} are used in chapter 4 for the two-photon excitation in Xe.

into dissociation, $S_{\rm DIS}$.

$$B_{\rm FI} = \sum_{\ell=|m|}^{\ell=n-1} S_{\rm FI}(\ell) / \sum_{\ell=|m|}^{\ell=n-1} \left[S_{\rm FI}(\ell) + S_{\rm DIS}(\ell)\right] \tag{2.10}$$

We assume that the electric field thoroughly mixes the ℓ's so that all of them are equally likely. For the ℓ partial wave, the probability to scatter and leave the molecule is

$$S_{\rm FI}(\ell) = 4\Phi_{\ell m}(\cos\theta_s)\sin^2(\pi\mu_\ell) \tag{2.11}$$

where μ_ℓ is the quantum defect, and the probability to dissociate is

$$S_{\rm DIS}(n\ell) = 2\pi\Gamma_0(\ell) = 2\pi(n-\mu_\ell)^3\Gamma_{\rm DIS}(n\ell) \tag{2.12}$$

where $2\pi(n-\mu_\ell)^3$ is the Rydberg period in atomic units and $\Gamma_{\rm DIS}(n\ell)$ is the zero field dissociation rate of the $n\ell$ state in atomic units.

Finally we define $D_{\rm FI}$ to be the direct excitation amplitude into the electron excitation channel. The energy averaged *ionization* cross section is in terms of these parameters is

$$\sigma_{\rm FI} \propto |D_{\rm FI}|^2 \left(\eta + [1-\eta]\, B_{\rm FI}\right) \tag{2.13}$$

We define $D_{\rm DIS}$ as the direct excitation amplitude into the molecular dissociation channel and the energy averaged *dissociation* cross section is

$$\sigma_{\rm DIS} \propto |D_{\rm DIS}|^2 + |D_{\rm FI}|^2 (1-\eta)(1-B_{\rm FI}) \tag{2.14}$$

There are two points to notice about these cross sections. The first is that the sum of the ionization and dissociation cross sections in the field equals the sum of the two cross sections in zero field. The second is that the ionization cross section goes to zero in a smooth manner as E decreases to $-2\sqrt{F}$; the exact manner it decreases to zero depends on how well the electron can elastically scatter down potential compared to how well it can cause dissociation.

2.4 Experimental set-up.

For nitric oxide, the $n = 25$ manifold of the Rydberg series converging to the lowest rovibrational state has an energy around 74546 cm^{-1} above the ground state (lowest ionization potential is 74721.7 cm^{-1}, [39]) which we can, in principle, reach with one photon of 134 nm. However, since we start at a finite temperature there is a rotational and vibrational ground state population distribution, which can all be excited by that

wavelength. The result of excitation will be a whole distribution of excited Rydberg levels on many rotational states close to the ionization potential. Consequently, we employed the following 1 + 1' photon excitation scheme. First we excite from the ground state to an intermediate $A^2\Sigma^+$ state (v' = 0) with a narrowband ultraviolet pulse in the region 225-227 nm. The rotational structure of the $A^2\Sigma^+$ state is well known [40–42]. The wavelength of the first laser pulse is set to populate a specific rotation of the zeroth vibration of the molecular core. From there on we excite with another narrowband UV pulse in the region 320-330 nm towards the Rydberg states. In this way we populate Rydberg states from only one initial rotation and vibration.

The experiments were performed with the set-up schematically depicted in Fig. 2.2. A supersonic jet expansion of pure nitric oxide gas was used from a pulsed valve with a backing pressure of one atmosphere into the vacuum chamber with a typical background pressure of 10^{-6} mbar. The pulsed valve is placed 4 cm from the interaction region, where the two UV pulses with a delay of 5 ns excite the molecules from their ground state to the Rydberg series. For the excitation step from the NO $^2\Pi$ ground state towards the $A^2\Sigma^+$ intermediate state (v' = 0) the output of a 10 Hz Nd:YAG laser pumped DCM dye (1) laser (tunable in the range 615-630 nm) was mixed in a BBO crystal with the Nd:YAG's third harmonic (355 nm). The resulting UV pulse (duration 7 ns, bandwidth 0.5 cm^{-1}), is tunable over the range 225-227 nm and separated in a set of 4 prisms. The pulses have a typical energy of 50 μJ.

The output of a second Nd:YAG pumped DCM dye (2) laser in the range 640-660 nm, is frequency-doubled in a KDP crystal resulting in a UV pulse with a bandwidth of 0.3 cm^{-1} and tunable in the range 320-330 nm. This second UV pulse is used for the excitation from the $A^2\Sigma^+$ intermediate state to the Rydberg series converging towards the NO^+ $^1\Sigma^+$ ionic ground state. The typical energy of the pulse is 150 μJ. The field direction between the two metal plates in Fig. 2.2 is chosen such that the electrons are accelerated toward a microspheroid plate below and the total photoionization yield is detected as a function of excitation frequency. Simultaneously the laser intensity is monitored with a photodiode.

2.5 Results and discussion.

Before employing the 1 + 1' excitation scheme we used 1 + 1 REMPI. The purpose of the measurement is to select appropriate rotational states for excitation to the Rydberg series and to check the influence of the static electric field on the position of the intermediate state. The rotational spectrum of the $A^2\Sigma^+$ intermediate state is well known [40,41] and we will not go into detail about this experiment. Resonant two-photon ionization via the $A^2\Sigma^+$ intermediate state (v' = 0) is detected by focussing a UV pulse in a wavelength range of 223-230 nm and monitoring the total electron yield as a function of excitation frequency.

The selection of pure rotational states N' from this spectrum is complicated by the presence of bandheads, i.e. higher rotational quanta overlap with lower ones and

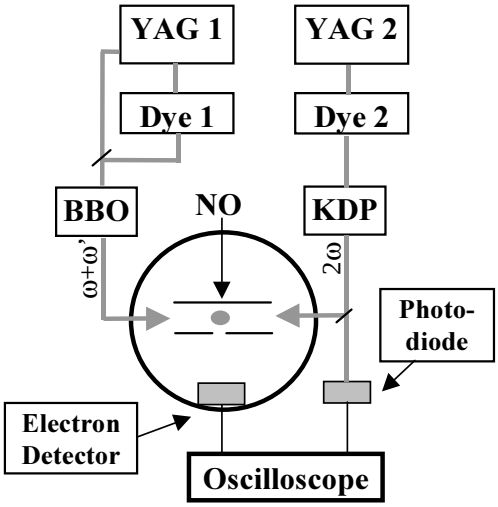

Figure 2.2: *Schematic overview of the experimental set-up. The output of the Nd:YAG-pumped dye laser 1 is mixed with the third harmonic of the Nd:YAG laser in a BBO crystal. The resulting UV pulse (wavelength region 225 - 227 nm) excites the outer electron of NO from the ground state to a specific rotational level the $A^2\Sigma^+$ intermediate state (v' = 0). The output of the Nd:YAG-pumped dye laser 2 is frequency doubled in a KDP crystal (wavelength region 320 - 330 nm) which excites the electron to Rydberg states. The interaction region of the NO beam and the laser pulses lies between two plates with a homogeneous static electric field. The total electron yield is detected by an electron detector and oscilloscope. Simultaneously the laser intensity is monitored by a photodiode.*

furthermore the P, Q and R (corresponding to ΔJ = -1,0,1 respectively) branches overlap. In fact, the only rotational sequence that we found usable is the P_{12} series on the very end of the low-energy side of the spectrum. This series does not have any overlap with other branches. It does show a bandhead structure but the relative population of higher rotational quanta compared to lower ones is minor at a low temperature. We estimate the temperature of the NO gas jet by fitting a Boltzmann distribution multiplied by the Höhn-London factors for a $\Sigma - \Pi$ transition to the 1 + 1 REMPI spectrum. The temperature is about 130 K for all our experiments. This high temperature for a supersonic jet can be explained by the large fraction of molecules that bounce into the interaction region via the (room temperature) electric field plates. At the estimated 130 K the selected $P_{12}(3/2)$ to $P_{12}(9/2)$ (where 3/2 and 9/2 is the total ground state angular momentum J), corresponding to rotational angular momenta of N' = 0, 1, 2, and 3, respectively, have a little overlap with higher angular momenta, with a maximum of 0.5%.

The 1+1 REMPI spectrum was measured at various field strengths. In the range 0-2000 V/cm no broadening of the lines was observed, only a slight shift on the order of the experimental bandwidth. This is not surprising in view of the small dipole moment

of this state.

From now on the first UV pulse is set to excite one specific rotational state with decreased fluence. In this way we create some population in the intermediate state and suppress direct 1 + 1 photoionization. The polarization of the laser is perpendicular to the electric field. In Fig. 2.3 a second UV pulse with a bandwidth of 0.3 cm^{-1} excites the outer electron of the NO molecule from the $A^2\Sigma^+$ intermediate state (N' = 0, v' = 0; at 44200.3 cm^{-1}) to Rydberg states converging to the NO^+ $^1\Sigma^+$ ionic ground state. The solid lines show the photoelectron yield monitored as a function of excitation frequency in a static electric field of 1000 V/cm. The polarization of the excitation laser was either perpendicular or parallel with respect to the electric field. On the lower energy side there is no electron yield. Once the excitation energy is sufficient to excite Rydberg states above the saddlepoint of the potential, peaks start to appear in the ionization yield at a threshold of about 74530 cm^{-1} both for parallel and perpendicular excitation. Note that the photoionization spectrum of the NO molecule is, surprisingly, no more complex than the spectrum of a regular alkali atom [1]. Using this field strength and bandwidth of the excitation laser we are able to resolve the individual Stark states. Depicted above the spectra in Fig. 2.3 are the positions of the middle k-states of hydrogen of the $n = 25$ and $n = 26$ manifolds upon perpendicular excitation.

There is a distinctive difference in width of the Stark peaks depending on the polarization of the excitation laser. The width of the peaks at parallel excitation is around 1 cm^{-1} corresponding to a lifetime of these states of about 15 picoseconds. Perpendicular excitation, however, leads to longer lifetimes of the states and the width of these peaks is as narrow as 0.3 cm^{-1}. Since that is the bandwidth of the excitation laser, we can only estimate a minimum lifetime of 50 picoseconds for these states. The dependence of the lifetimes with the polarization may be understood in terms of the geometry of this system. There is both a direct and an indirect path for photoionization and it is the indirect path that gives the Stark resonances. An outgoing electron that is not ejected in the direction of the saddlepoint bounces off the wall of the potential and returns to the ionic core. However, after one radial oscillation the angular momentum has evolved towards higher ℓ up to $\ell = n$ - 1. Higher angular momenta do not penetrate the ionic core and subsequently cannot scatter. Only after a full angular momentum oscillation the electron can scatter from the non-hydrogenic core into the direction of the saddlepoint resulting in autoionization. The broad peaks in the photoionization spectrum upon excitation with parallel polarization indicate a single angular oscillation of the electron before autoionization whereas perpendicular excitation leads to several recurrences of the electron before escaping.

An important observation in Fig. 2.3 is that the ionization peaks do not appear in a stepfunction-like manner but slowly increase in intensity. The number of peaks per unit energy increases with excitation energy converging on the high-energy side to a constant yield (the ionization potential in zero-field is at 74721.7 cm^{-1}; Ref. [39]). Calculation of the Rydberg series in an electric field by using the parameters of Table 1 and a convolution with a Gaussian having a width of 0.3 cm^{-1} well simulates

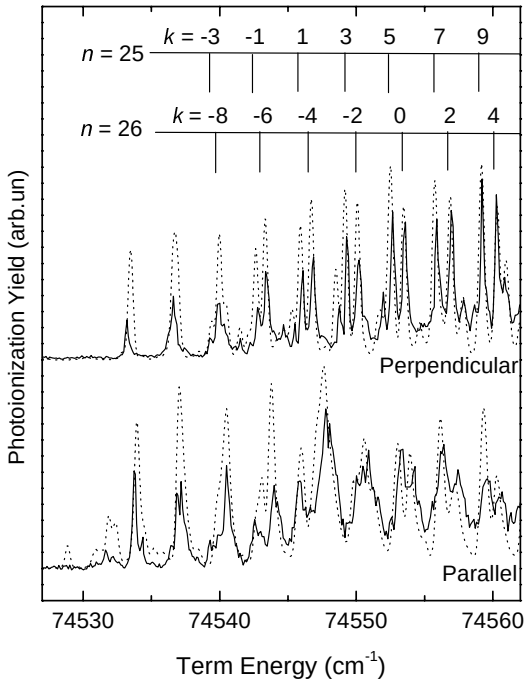

Figure 2.3: *The total photoionization yield as a function of term energy via the* $A^2\Sigma^+$ *intermediate state with rotation N' = 0. The laser polarization is either perpendicular or parallel with respect to the electric field of 1000 V/cm. The solid lines are the experimental data, the dotted lines are the calculated curves. The spectra are well reproduced by MQDT theory described in section 2.2.2. Predissociation is included in the calculations with predissociation rates taken from Ref. [28]. For comparison the position of some k-states of the hydrogenic n = 25 and n = 26 manifolds upon perpendicular excitation are depicted.*

the observed photoionization spectra far above (>40 cm^{-1}) the saddlepoint. Close to the saddlepoint, however, the calculation is only accurate concerning the position and width of the peaks. The discrepancy in intensity is diminished by including predissociation into the calculations. The dotted lines in Fig. 2.3 are calculations including the predissociation rates shown in table 2 (taken from Ref. [28]). The average predissociation rate can be found by adding all predissociation rates of the separate angular momentum states $\Gamma_0(total) = 3157/n^3$ $\text{cm}^{-1} \triangleq 6\ 10^{14}/n^3$ s^{-1}. In the plotted energy region the rates are typically 10^9-10^{10} s^{-1}.

$\Gamma_0(s) = 500$ cm^{-1}	$\Gamma_0(f) = 43$ cm^{-1}
$\Gamma_0(p) = 1610$ cm^{-1}	$\Gamma_{eff}(\ell > 3) = 4$ cm^{-1}
$\Gamma_0(d) = 1000$ cm^{-1}	

Table 2.2. *Decay rates for state n:* $\Gamma_0(\ell)$ / n^3*; taken from Ref.* [28].

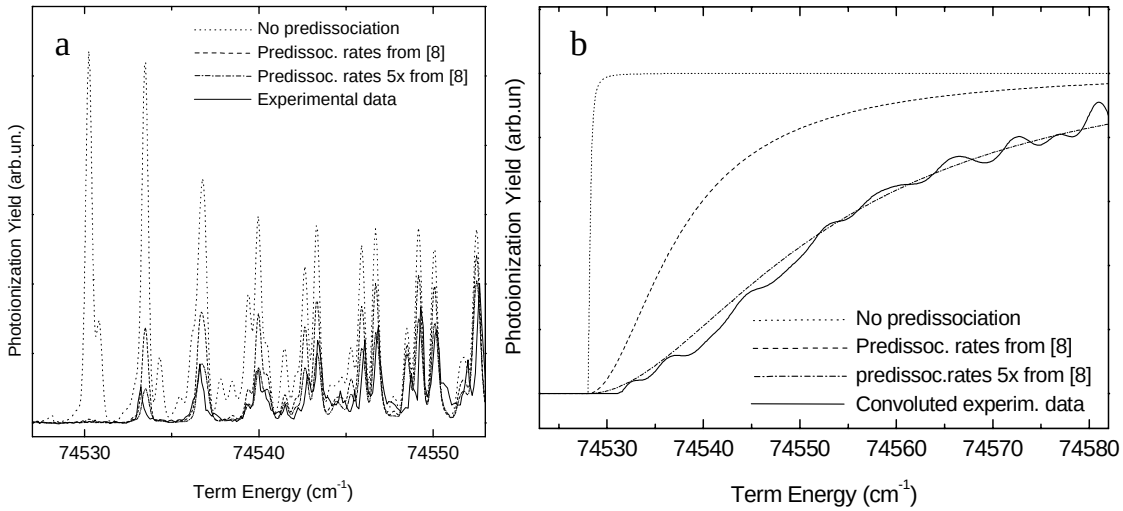

Figure 2.4: *a) Three calculations without (dotted line) and with predissociation (dashed line with rates taken from Ref. [28], dashed-dotted line 5 times faster) are compared to the experimental data (solid line) to illustrate the importance of including predissociation. b) Three calculations based on Eq. 2.13 without (dotted line) and with predissociation (dashed line with rates taken from Ref. [28], dashed-dotted line 5 times faster) are compared to the experimental data concoluted with a Gaussian of 3 cm^{-1} (solid line). All traces have perpendicular excitation.*

To appreciate the effect of predissociation on the calculations of the photoionization yield in Fig. 2.4a three calculations are depicted, one without and two with different predissociation rates. All calculated traces are convoluted with a Gaussian having a width of 0.3 cm^{-1}. There is a dramatic decrease in intensity of the photoionization yield close to the saddlepoint upon including predissociation. Some peaks have completely vanished making the photoionization threshold appear higher in energy. Furthermore the stepfunction-like behavior of the photoelectron yield at threshold is lost and intensity only slowly increases with higher excitation energy. Note that the agreement with the experimental results would improve even more by assuming a higher predissociation rate. The dash dotted line in Fig. 2.4a includes a five times faster predissociation rate than suggested in Ref. [28] and is virtually indistinguishable from the experimental data.

That predissociation only decreases intensity in the region of about 40 cm^{-1} above the saddlepoint lies in the fact that the escape angle of the Rydberg electron far above the saddlepoint is large and the electron autoionizes on subpicosecond time scales. Closer to the saddlepoint energy, however, the exit created by the electric field becomes narrow and the lifetime, hence the number of oscillations of the Rydberg electron, increases. After each angular oscillation the electron recurs to the core with low angular momentum ℓ and can couple to the predissociation channel. At the saddlepoint en-

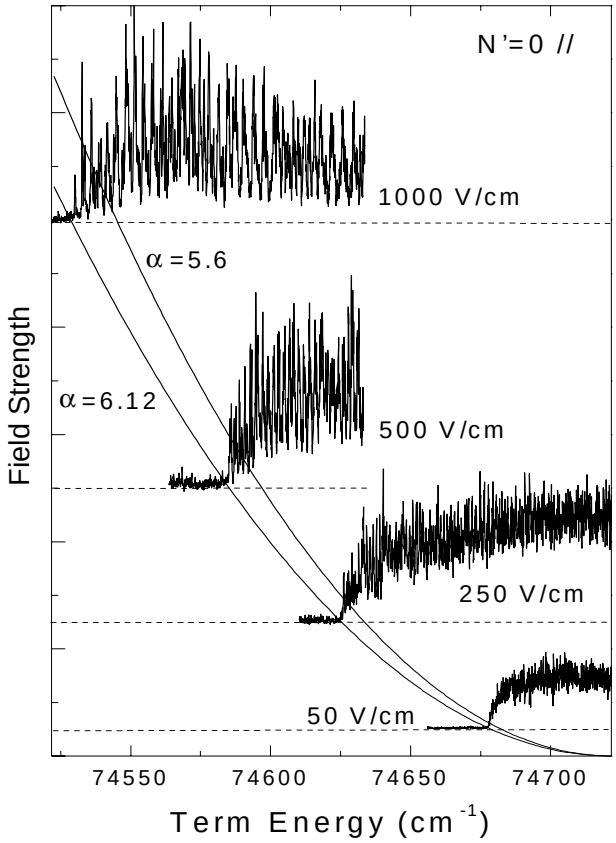

Figure 2.5: *The photoionization yield from N' = 0 as a function of term energy in electric fields of 1000, 500, 250 and 50 V/cm. The polarization of the excitation laser is parallel to the electric field. All structure seen is not noise but resolved Stark states. Plotted also is the position of the threshold in those fields with α = 6.12 and α = 5.6 as suggested by Ref. [20].*

ergy the predissociation is even dominant and the photoionization yield is completely quenched. Naturally the perpendicular excited states experience a larger influence of predissociation because of the longer lifetimes. It is useful to compare Eq. 2.13 derived in the theory section with the detected cross section convoluted with a Gaussian of 3 cm^{-1} width (Fig. 2.4b). The resolved Stark states are smoothed out and we can concentrate on the overall intensity behavior. As we already saw in Fig. 2.4a predissociation needs to be included and predissociation rates taken from Ref. [28] do not fit the experimental data very well ($S_{\mathrm{DIS}} = 0.08$). Five time faster rates are needed for a good fit ($S_{\mathrm{DIS}} = 0.4$). We have no explanation for the discrepancy except that the rates are extrapolated from higher n (70 - 120) and lower fields (<1 V/cm).

Including predissociation in interpreting photoionization yield spectra of molecules in a static electric field is important to determine the saddlepoint energy. If one determines the saddlepoint energy by fitting the experimental spectra with a smoothed

stepfunction, disregarding predissociation, one obtains a threshold that is too high in energy or, equivalently, the α from Eq. 2.2 would be too low. The photoionization yield measurements of nitric oxide in an electric field reported in Ref. [19,20] exhibit an apparent threshold that was higher in energy than expected. Instead of the theoretical $\alpha = 6.12$ cm^{-1} Ref. [20] reported 5.6 cm^{-1} and Ref. [19] even 3.69 cm^{-1}. In Fig. 2.5 the photoionization yield spectra as a function of term energy are shown for various applied field strengths. The excitation is via the $N' = 0$ intermediate rotational state with polarization parallel to the electric field. Also shown is the saddlepoint energy as a function of electric field strength according to Eq. 2.2 with $\alpha = 6.12$ cm^{-1} (a) and $\alpha = 5.6$ cm^{-1} (b) taken from Ref. [20]. By resolving the structure of Stark states and including predissociation in the calculation we find $\alpha = 6.12$ cm^{-1}. By artificially cutting the high-frequency parts of the spectrum and fitting with a smoothed stepfunction like Ref. [19, 20], we naturally obtain, when taking the midpoint of the rise, a lower α (in our case $\alpha = 5.7$ (1) cm^{-1}).

In earlier studies on molecules in an electric field [22, 43–46] Stark structure has been resolved. A saddlepoint, however, is not observed due to rotational or vibrational autoionization and we cannot compare the influence of predissociation to other molecules.

We now focus on the rotational dependence of the photoionization spectrum. As in Fig. 2.4, Fig. 2.6 shows the photoionization yield monitored as a function of excitation frequency of NO in an electric field of 1000 V/cm. The lowest trace in Fig. 2.6 is taken with excitation via the $A^2\Sigma^+$ intermediate rotational state $N' = 0$ (at 44200.3 cm-1). Three more traces are shown taken with excitation via the rotational states $N' = 1$, 2 and 3 (at 44204.3, 44212.2 and 44224.1 cm^{-1} respectively). For all traces, the laser polarization is perpendicular to the electric field. Starting from higher rotational states, the threshold is higher in energy. The theoretical saddlepoint energies are depicted with the dotted line. The increase of threshold energy corresponds to the increase of rotational energy E_{rot} (Eq. 2.4) with a rotational constant B = 1.9842 cm^{-1} (Ref. [33]). The only open channel for excitation lower than the saddlepoint energy via rotational states $N'>0$ is excitation of a bound Rydberg state that decays by rotational autoionization into a lower N' Rydberg series. The near absence of signal below the saddlepoint energies shows that the rotational autoionization is very weak; note that the competing predissociation channel sets an upper limit to the time during which rotational autoionization can take place.

Another argument for weak rotational coupling is shown in Fig. 5b. Identical spectra are depicted as in Fig. 5a but now as a function of relative binding energy, i.e. energy compared to the ionization energy in zero field of the selected intermediate rotational state. Only a small energy range is shown to illustrate the similarities between the Rydberg series converging to various rotational limits. The spectra are detected with perpendicular excitation via the $A^2\Sigma^+$ rotational states $N' = 0$, 1, 2 and 3 (ionization energy $E_{(IP)} = 74721.7$, 74725.7, 74733.6, and 74745.5 cm^{-1} respectively). In this energy range the separate Stark states of overlapping n-manifolds can be distinguished. Comparison of the four traces reveals that the photoionization yield is very similar, in-

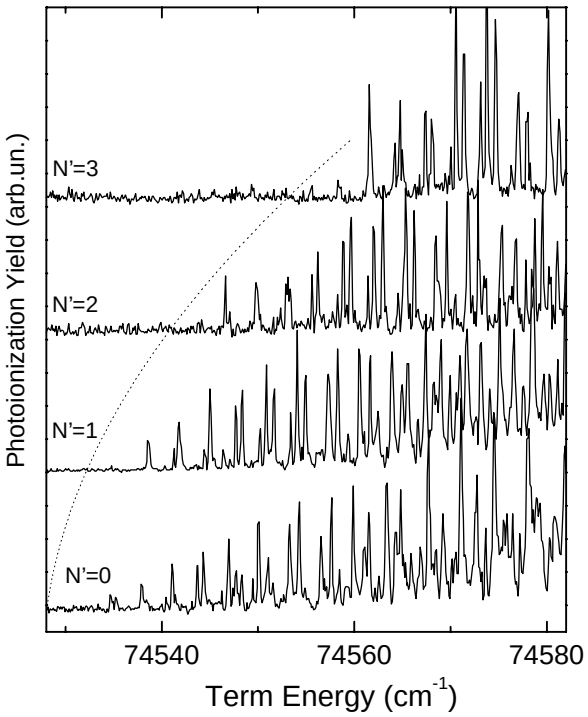

Figure 2.6: *The total photoionization yield as a function of term energy. The four spectra are detected via the $A^2\Sigma^+$ intermediate state with rotations N' = 0, 1, 2 and 3. The laser polarization is perpendicular with respect to the electric field of 1000 V/cm. For each higher rotation the apparent threshold is higher in excitation energy. The dotted line is the expected ionization threshold.*

dependent of rotation. Only the intensity of the separate peaks differs somewhat. This suggests that the excitation occurs predominantly via the Q-branch (N' - $N^+ = 0$, as in Ref. [19]) and only a weak rotational coupling changes the intensities of the peaks. In the case of nitric oxide, the dynamics of a complicated molecular ion and a Rydberg electron in a static electric field is considerably simpler than might be expected.

2.6 Conclusion.

We have investigated the photoionization of Rydberg electrons of the nitric oxide molecule. In a 1 + 1 REMPI experiment we selected rotational states of the $A^2\Sigma^+$ intermediate state (v' = 0) and monitored the dependence of a static electric field. Then the frequency of the first UV pulse was set to populate a specific rotational state and a second UV pulse was applied to excite to the Rydberg states. The excitation was done with polarization parallel or perpendicular to the electric field. The photoionization yield was monitored for autoionizing Rydberg states for NO in various electric fields and via different rotational states. The Stark structure in the spectra is fully under-

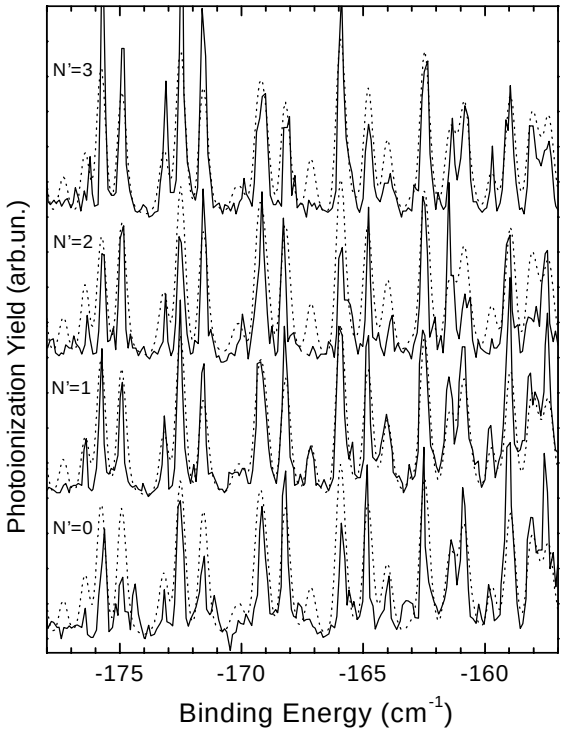

Figure 2.7: *The solid lines are the same traces as for Fig. 2.6 but now as a function of relative binding energy, i.e. the term energy minus the ionization potential energy of the intermediate rotational states. The four spectra are detected with perpendicular excitation via the $A^2\Sigma^+$ intermediate state with rotations N' = 0, 1, 2 and 3. Only a small energy range is shown to illustrate the similarity between the Rydberg series converging to the various rotational limits. The dotted lines are the calculated spectra.*

stood and accurate simulations are achieved by quantum calculations based on MQDT. We observe that lifetimes of the Stark states are different upon different excitation polarization: parallel excitation leads to lifetimes of about 15 ps whereas perpendicular excitation leads to much longer lifetimes. An important observation is that predissociation quenches the photoionization yield close to the saddlepoint which can lead to misinterpretation of photoionization threshold energy. A formula (Eq. 2.13) for the average behavior of the photoionization cross section , including the effect of predissociation, gives insight in to how the ionization signal is suppressed near threshold. The first peak on the low-energy side of the NO photoionization spectrum is therefore the onset of the Stark structure rather than the threshold of autoionization.

The photoionization spectra via various rotational states are compared and we observe that excitation occurs predominantly via the Q-branch. There is only weak rotational coupling leading to a lack of rotational autoionization and very similar photoionization spectra for the different rotational states of the core. In fact the spectra

are very reminiscent of an alkali atom. We can consider the Rydberg series of NO to consist of independent sets of one Rydberg series of one rotational state with an open predissociation channel. In the following chapter we consider ammonia where the rotational coupling cannot be neglected. In that case there is a competition between fieldionization, predissociation and rotational diffusion.

Chapter 3

Decay dynamics of vibrationless Rydberg series in ammonia.

A novel method is presented to retrieve the average predissociation rate and the average rotational autoionization rate of a molecule by detection of the fieldionization spectrum only. An intuitive picture and a quantitative description are derived for the competition between the three decay channels, fieldionization, rotational autoionization and predissociation. Fieldionization spectra of various rotational states of ammonia are presented and fitted. From the fits we found that the average predissociation rate of the Rydberg series converging to the vibrationless $N^+ = 3$ ionic state is about equal to the average rotational autoionization rate to the Rydberg series converging to the vibrationless $N^+ = 2$ ionic state, namely 1 $10^{15}/n^3$ s^{-1}.

3.1 Introduction.

There is a considerable interest in the highly excited states of the ammonia molecule. The competition of various decay channels, including fieldionization, vibrational and rotational autoionization and predissociation, leads to complicated and intriguing spectroscopy of these states [47–49]. Understanding the dynamics of these decay channels is of importance for rotationally resolved zero-kinetic energy-photoelectron spectra (ZEKE-PES) [50–52], pulsed field ionization (PFI) [53], and mass-analyzed threshold ionization spectra (MATI) [54–56]. It is experimentally difficult to separate one particular decay channel from all others. Especially, the influence of predissociation on the highest Rydberg states of ammonia is not well known. There are some reports concerning the lowest electronic states [57–59]. To our knowledge there is no accurate predissociation rate known of the high Rydberg states except that photodissociation is dominant over photoionization in zero-field just above the ionization potential of ammonia [60].

We present a novel method to measure the predissociation and rotational autoionization rates. This technique relies on the detection of fieldionization spectra. We have already seen in chapter 2 that predissociation in nitric oxide leads to a fieldionization spectrum that is quenched *just above* the saddlepoint. The loss of fieldionization yield can directly be related to the decay rate of predissociation. The competition of three decay channels in ammonia, namely fieldionization, rotational autoionization and predissociation, leads, in the absence of vibrational autoionization, to a unique fieldionization yield spectrum. Rotational autoionization has a similar quenching effect as predissociation, but manifests itself in the fieldionization spectrum by yielding fieldionization signal *below* the saddlepoint of the excited rotational state. Hence, the contribution of predissociation and rotational autoionization in the fieldionization spectrum is separable and both rates are independently retrievable.

In ammonia optical excitation of an electron from the doubly occupied $3a_1$ nitrogen lone pair in the pyramidal C_{3v} ground state populates Rydberg states with planar (D_{3h}) geometry. These states are described as symmetric top states [5] with a total angular momentum J and a projection K on the molecular axis. The rotational energy E_{rot} is $BJ(J+1) - (B-C)K^2$, where B and C are the rotational constants. Like in NO the excitation scheme is via an intermediate state, the $\tilde{C}'^1A_1'(0000)$ state, to select a rotation and vibration. All four independent vibrations of the intermediate state are chosen to be zero to avoid the additional competition of vibrational autoionization. Throughout the chapter N' denotes the rotational quantum number of the core for the intermediate state and N^+ the rotational quantum number of the core for the Rydberg series converging to the NH_3^+ ionic state.

3.2 Experimental.

To obtain frequency-resolved spectra of the Rydberg series of ammonia in an electric field we used the following set-up: The output of a Nd:YAG laser driven nanosecond dye laser with a wavelength of around 626 nm is frequency doubled in a KDP crystal. The frequency-doubled light, with an energy of 0.5 mJ/pulse, is used to drive the two-photon $\tilde{C}'^1A_1'(0000) \leftarrow \tilde{X}^1A_1'(0000)$ transition (see fig. 3.1). In this way a single quantum state is selected. A second Nd:YAG laser driven nanosecond dye laser produces light with a wavelength around 550 nm and with an energy of about 5 mJ to populate the Rydberg series converging to the NH_3^+ $\tilde{X}^2A_2''$ ionic state. The laser pulses arrive simultaneously in the vacuum chamber through a 20 cm lens. The second laser pulse is slightly defocussed at the focal spot of the first laser pulse. A pulsed valve produces a gas jet of helium with 5% ammonia between two electric field plates. The first laser pulse is fixed to excite a chosen rotational state while the second is scanned over the Rydberg series in a 2 + 1' REMPI scheme. Ionized electrons are detected through a mesh in the plates by an electron detector.

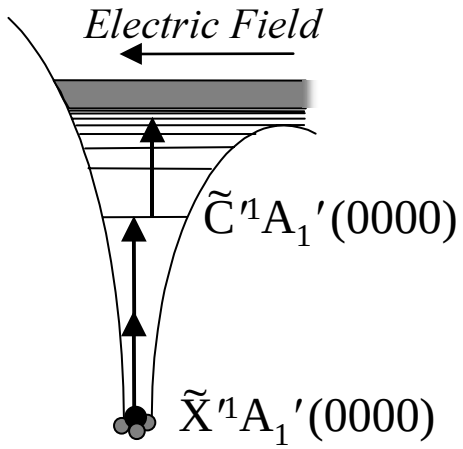

Figure 3.1: *Excitation scheme of ammonia in a static electric field. The molecule is excited with a 2 + 1' REMPI scheme from the $\tilde{X}^1A_1'(0000)$ ground state via the $\tilde{C}'^1A_1'(0000)$ intermediate state to the Rydberg series converging to the vibrationless $NH3^+$ $\tilde{X}^2A_2''$ ionic state. The static electric field lowers the potential energy on one side. The maximum potential energy of that side is the saddlepoint.*

3.3 Results and discussion.

The spectroscopy of the intermediate $\tilde{C}'$-state is well known [61]. The Q_s lines are by far dominant, where $\Delta N' = 0$ and $\Delta K' = 0$, and the transition frequencies can be found with the rotational constants of the $\tilde{X}^1A_1'(0000)$ ground state (B = 9.94 cm^{-1} and C = 6.23 cm^{-1} [62]) and the $\tilde{C}'^1A_1'(0000)$ excited state (electronic energy E = 63865.62 cm^{-1}, B = 10.778 cm^{-1} and C = 5.264 cm^{-1} [63]). Besides some accidental degenerate transition frequencies, we can select most rotational states unambiguously on their rotational quantum numbers N' and K'. In the subsequent experiments, the frequency of the first laser is fixed to excite the rotational levels (N',K') = (3,0), (3,1) or (3,3) of the $\tilde{C}'^1A_1'(0000) \leftarrow \tilde{X}^1A_1'(0000)$ transition at 63875.68, 63873.87 or 63859.44 cm^{-1} respectively, while the second laser frequency is scanned over the Rydberg series.

In Fig. 3.2 photoionization yield spectra are shown, detected with a 2 + 1′ REMPI scheme where the second laser scans over the energy range on the x-axis. The electric field is chosen to be just high enough to push the photoelectrons to the electron detector, in this case 7 V/cm. The clear Rydberg series that is observed for the Q_s(3,0) and Q_s(3,1) spectra is fitted with the Rydberg formula $E = IP - 1/2(n-\delta)^2$ [1], yielding an ionization potential IP of 18376.3(3) cm^{-1} and a quantum defect δ of 0.03(2). There is a second, smaller series appearing as a right shoulder on each peak of the Q_s(3,0) and Q_s(3,1) spectra. This second Rydberg series is well fitted with an IP of 18376.3(3) cm^{-1} and a quantum defect δ of 0.60(5). In the Q_s(3,3) spectrum these two series are also observed, but here they have equal intensity. The ionization potential of 18376.3(3) cm^{-1} corresponds to the $N^+ = 4$ limit. Assuming that the rotational constants of the

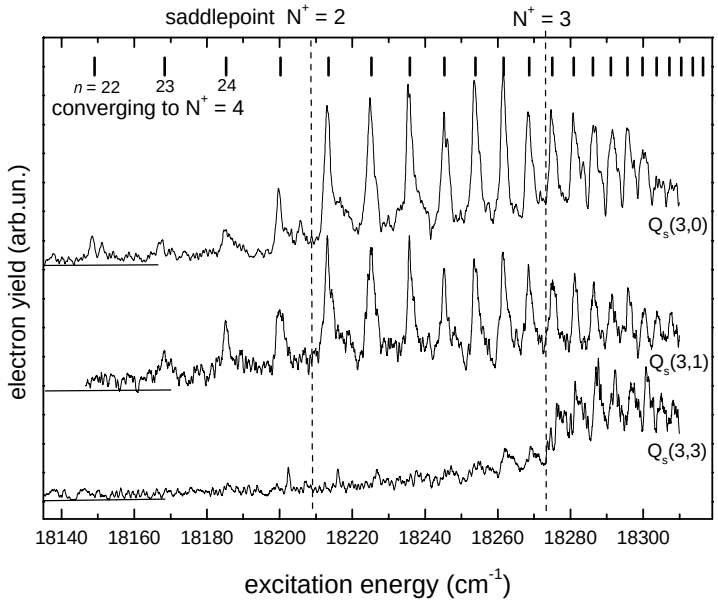

Figure 3.2: *Electron yield spectra, detected with a 2 + 1' REMPI scheme where the first laser is fixed on the two photon Q_s(3,0), Q_s(3,1) or the Q_s(3,3) of the $\tilde{C}'^1A_1'(0000) \leftarrow \tilde{X}^1A_1'(0000)$ transition. On the x-axis is the energy of the second photon. The electric field is 7 V/cm. The sticks at the top are the calculated energies of a Rydberg series with quantum defect 0.03 converging to an ionization potential at 18376.3 cm^{-1} (corresponding to $N^+ = 4$). Indicated are the positions of the saddlepoint energies of the $N^+ = 2$ and $N^+ = 3$ series at 18209 and 18273 cm^{-1}, respectively.*

ionic state are identical to those of the $\tilde{C}$-state, it implies that the lowest *IP* of the vibrationless ammonia ion with $(J^+, K^+) = (0, 0)$ is at 82155.2(5) cm^{-1}. The reported values for the lowest *IP* range from 82151 to 82159 cm^{-1} [51, 52, 56].

In a field of 7 V/cm the saddlepoint energy of $N^+ = 3$ is at 18273 cm^{-1} and the saddlepoint energy of $N^+ = 2$ is at 18209 cm^{-1} [1]. The observed spectra in Fig. 3.2 are reminiscent of those measured by Pratt and coworkers [47, 48] where interleaved Rydberg series were observed with $N^+ - N' = 0, 1$. The spectra can be explained by excitation of the $N^+ = 3$ Rydberg series that are strongly coupled to the $N^+ = 4$ series. We cannot resolve the separate Rydberg levels of the $N^+ = 3$ series because the excitation is at very high n. The photoelectron yield is strong above the $N^+ = 2$ saddlepoint, except for the spectrum detected via the Q_s(3,3). From this difference we deduce that the dominant ionization pathways are $\Delta N^+ = 0, -1$ with the restriction $\Delta K^+ = 0$, as observed also in MATI spectra [56]. Since there is some electron yield below the $N^+ = 2$ saddlepoint, there must be some $\Delta N^+ = \pm 2$ coupling. Also the signal below the $N^+ = 3$ saddlepoint for the spectrum detected via the Q_s(3,3) indicates that there is some coupling with $\Delta K^+ \neq 0$.

Rotational autoionization is very fast: The observed peaks have a width of about 3 cm^{-1}, corresponding to a lifetime of 10 ps. Since the observed states are around n = 30, converging to $N^+ = 4$, the lifetime corresponds to about two radial oscillations ($\tau_{rad} = 4$ ps for $n = 30$). Moreover, there is no clear intensity difference of peaks above and below the $N^+ = 3$ saddlepoint. This implies that rotational autoionization occurs at least on the same time scale as fieldionization at that energy. As is observed in atoms the fieldionization just above threshold occurs in the order of tens of picoseconds [64,65].

Upon introduction of a strong electric field the angular momentum ℓ of the electron is no longer conserved: Each Rydberg state n splits into n non-degenerate Stark states that are superpositions of all angular momenta, ranging from 0 to n - 1. Since only the low-angular momentum fraction penetrates the core region, and can hence contribute to the scattering into the open channels (see chapter 1), the lifetime of each Stark state is much longer than the zero-field Rydberg state, up to n times longer [28]. Furthermore, there might be a difference in the observed width of the peaks with the polarization of the second laser as compared to the electric field. Depending on the laser polarization, the electron has to scatter differently to escape over the saddlepoint, which can influence its lifetime.

In Fig. 3.3a the electron yield spectra are depicted in a field of 1000 V/cm, detected with a 2 + 1′ REMPI scheme where the first laser is fixed on the two-photon $Q_s(3,0)$, $Q_s(3,1)$ or the $Q_s(3,3)$ of the $\tilde{C}'^1A_1'(0000) \leftarrow \tilde{X}^1A_1'(0000)$ transition. On the x-axis is the energy of the 1′ photon, which has a polarization parallel to the electric field. The peaks are much sharper, about 0.5 cm^{-1}, which is the laser resolution. Similar to the zero-field spectra there is a clear change in electron yield at the $N^+ = 3$ saddlepoint for the $Q_s(3,3)$ intermediate state. For the other two intermediate states, however, electron yield is only reduced to (nearly) zero below the $N^+ = 2$ saddlepoint. The saddlepoint energies do not seem to be sharp cut-off energies for the electron yield: The signal slowly decreases closer to a threshold energy. The decrease is even slower for perpendicular polarization of the second laser field compared to the electric field. In Fig. 3.3b the same spectra are shown as in Fig. 3.3a, but now with the polarization of the second laser pulse perpendicular to the electric field. There is no difference in width of the peaks since we are laser resolution limited. All spectra show a slow modulation that we can attribute to the coupling with the Rydberg series converging to the $N^+ = 4$ limit.

3.4 Simulation of average fieldionization.

As we have seen in the previous chapter the overall behavior of the fieldionization spectra can be described with an intuitive picture. In ammonia we have a three-channel competition between fieldionization, rotational autoionization and predissociation.

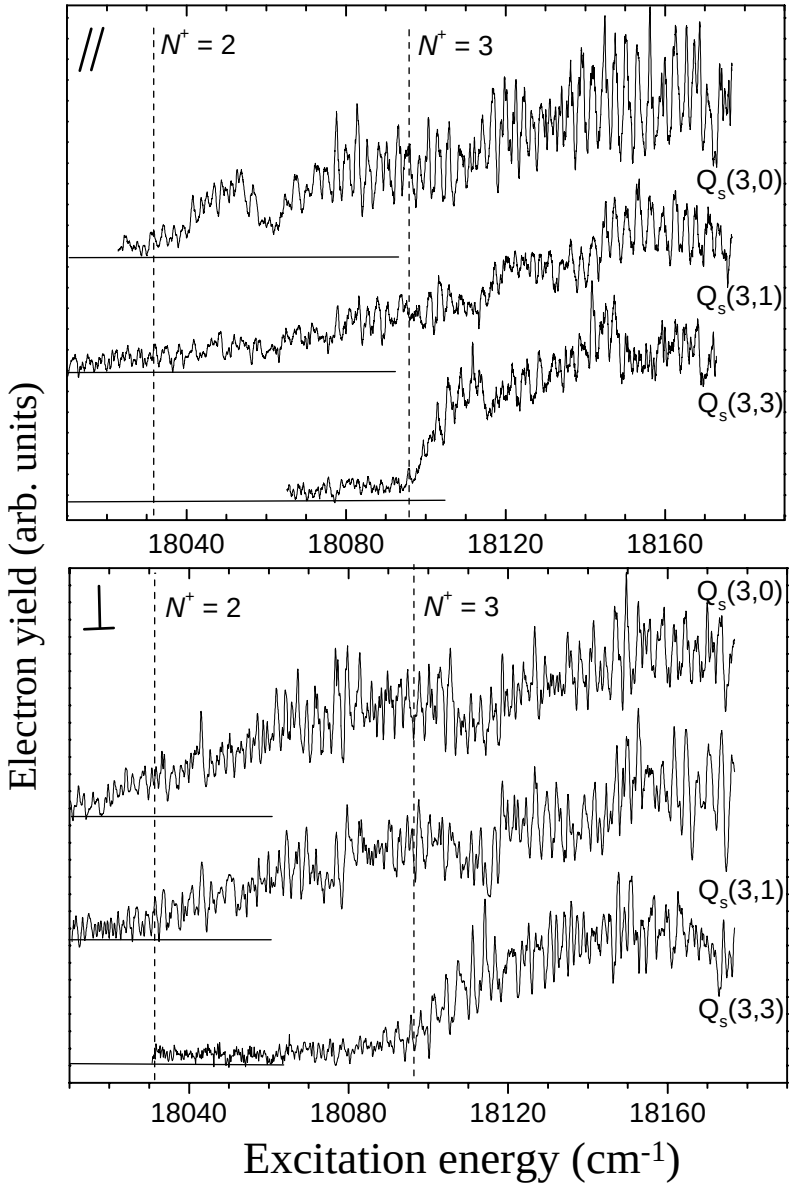

Figure 3.3: *a) Electron yield spectra, detected with a 2 + 1' REMPI scheme where the first laser is fixed on the two photon $Q_s(3,0)$, $Q_s(3,1)$ or the $Q_s(3,3)$ of the $\tilde{C}'^1A_1'(0000) \leftarrow \tilde{X}^1A_1'(0000)$ transition. On the x-axis is the energy of the second photon that has parallel polarization compared to the electric field of 1000 V/cm. The Stark-structure is well resolved. Indicated are the positions of the saddlepoint energies of the $N^+ = 2$ and $N^+ = 3$ series at 18031 and 18096 cm^{-1}, respectively. b) Same for perpendicular excitation.*

However, in fact it is a two-channel competition in disguise because both the rotational autoionization and the predissociation depend on the number of times the electron returns to the core. Therefore there is a fixed ratio between both decays above the lowest ionization threshold and there is in fact a competition between field-ionization versus the combination of rotational autoionization and predissociation. An additional complication, however, is the detection of the combined behavior of several rotational channels with their different ionization thresholds. Note that we cannot experimentally distinguish between predissociation and other core-dependent decay, like e.g. fluorescence or internal relaxation to other electronic states. We assume that the predissociation of the molecule is the dominant mechanism of core-dependent decay (see e.g. [60]). If otherwise, this has no implications for our simulations.

For the remainder of this section we prefer the term rotational *diffusion* for population transfer from a high to a lower rotational state since rotational *autoionization* occurs only into the continuum of the lower rotational state. Let us start with the simplest situation. We excite an electron to a single rotational channel that couples with one lower rotational channel. A strong electric field makes fieldionization possible in both channels. There is no predissociation yet and we cannot resolve any (Stark)structure. The situation can be described by the two-channel competition and the relevant equations are similar to the ones presented in chapter 2. The ammonia fieldionization cross section σ_{FI} for the initial rotational channel is:

$$\sigma_{\mathrm{FI}} \propto |D_{\mathrm{FI}}|^2 \left(\eta + [1-\eta]\, B_{\mathrm{FI}}\right) \tag{3.1}$$

where D_{FI} is the excitation amplitude into the rotational channel and η is the electron fraction that is directly ejected down-potential into fieldionization. The bound fraction, 1-η, can still fieldionize with a branching ratio B_{FI}. The branching ratio is given by the probability to fieldionize S_{FI}, divided by the probability to fieldionize plus the probability to rotationally diffuse to the lower rotational state S_{RD} (which is similar to the predissociation probability S_{DIS} in chapter 2):

$$B_{\mathrm{FI}} = \sum_{\ell=|m|}^{\ell=n-1} S_{\mathrm{FI}}(\ell) \Big/ \sum_{\ell=|m|}^{\ell=n-1} \left[S_{\mathrm{FI}}(\ell) + S_{\mathrm{RD}}(\ell)\right] \tag{3.2}$$

Both η and B_{FI} depend on the energy above the fieldinduced saddlepoint. The lower rotational channel is now populated by the fraction of electrons that rotationally diffuses from the higher rotational channel. The cross section of the lower rotational channel σ_{RD} is given by:

$$\sigma_{\mathrm{RD}} \propto |D_{\mathrm{FI}}|^2 \left(1-\eta\right)\left(1-B_{\mathrm{FI}}\right) \tag{3.3}$$

An electron that has rotationally diffused to the lower rotational channel can fieldionize if it is above the saddlepoint of this rotational channel. Since there is no predissociation, the cross section for rotational diffusion is equal to the cross section

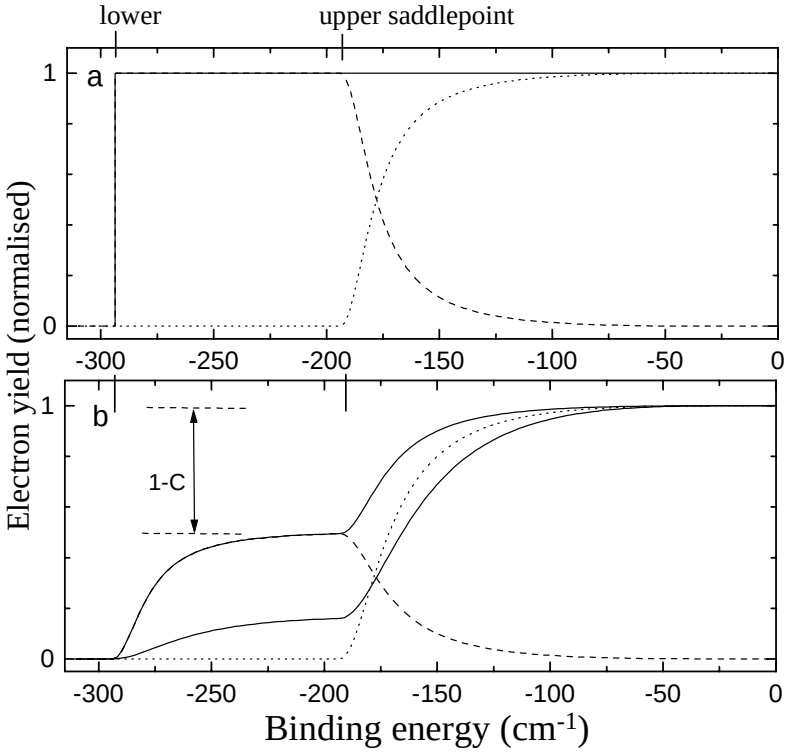

Figure 3.4: *a) The expected average photoionization yield (solid line), in the absence of predissociation, of two rotational channels in a field of 1000 V/cm. The rotational diffusion rate is 1 10^{15} s^{-1}. The photoionization yield can be divided in the fieldionization from the upper rotational state (dotted line) and the fieldionization via rotational diffusion of the lower rotational state (dashed line) b) Same as a), but with a predissociation rate of 1 10^{15} s^{-1} (upper solid line). The factor 1-C = 1/2 is lost to predissociation. For comparison, a predissociation rate of 5 10^{15} s^{-1} results in the lower solid line.*

for fieldionization via rotational diffusion $\sigma_{\mathrm{FI}\leftarrow\mathrm{RD}}$. The situation is depicted in Fig. 3.4a: The electron is excited with perpendicular polarization into the upper rotational channel that couples to a lower rotational channel with an energy difference of 100 cm^{-1}. An electric field of 1000 V/cm decreases the saddlepoint to -193.6 cm^{-1} as compared to the zero-field ionization potential. The dotted line is fieldionization from the high rotational channel. The intensity at the saddlepoint is quenched by competition of rotational diffusion with a rate of 1 $10^{15}/n^3$ s^{-1} in this example. The dashed line is the fieldionization from the lowest rotational channel via rotational diffusion. There is a sharp cut-off of yield at the saddlepoint of the lower rotational channel. The solid line represents the combined photoionization yield that would be detected in this idealized experiment.

Addition of predissociation changes both cross sections. As mentioned, both the

rotational diffusion and the predissociation rates depend on how often the electron returns to the core per time unit. There is a fixed ratio of probabilities of diffusing to another rotational channel or to predissociate. We define the ratio of $S_{\rm RD} : S_{\rm DIS}$ to be $1 : \zeta$.

The branching ratio $B_{\rm FI}$ changes into:

$$B'_{\rm FI} = \sum_{\ell=|m|}^{\ell=n-1} S_{\rm FI}(\ell) / \sum_{\ell=|m|}^{\ell=n-1} [S_{\rm FI}(\ell) + S_{\rm RD}(\ell) + S_{\rm DIS}(\ell)] = \tag{3.4}$$

$$\sum_{\ell=|m|}^{\ell=n-1} S_{\rm FI}(\ell) / \sum_{\ell=|m|}^{\ell=n-1} [S_{\rm FI}(\ell) + (1+\zeta) S_{\rm RD}(\ell)] \tag{3.5}$$

The fieldionization cross section in Eq. 3.1 is slightly modified by replacing $B_{\rm FI}$ with $B'_{\rm FI}$. Since $B'_{\rm FI}$ is always smaller than $B_{\rm FI}$, the quenching of electron yield close to the saddlepoint is larger. The cross section for rotational diffusion in Eq. 3.3 now differs on two points: It is also modified by replacing $B_{\rm FI}$ with $B'_{\rm FI}$ and it is multiplied by C $= 1/(1+\zeta)$ since the fraction 1-C is 'lost' to predissociation. Finally, the fieldionization cross section via rotational diffusion $\sigma^F_{\rm FI \leftarrow RD}$ is found by combining the competition between fieldionization and predissociation in the lower rotational channel with the cross section for population of the lower rotational channel:

$$\sigma^F_{\rm FI \leftarrow RD} \propto |D'_{\rm FI}|^2 \left(\eta' + [1-\eta'] B''_{\rm FI}\right) \tag{3.6}$$

$$|D'_{\rm FI}|^2 = \frac{1}{1+\zeta} |D_{\rm FI}|^2 (1-\eta)(1-B'_{\rm FI}) \tag{3.7}$$

where $B''_{\rm FI}$ is the branching ratio of fieldionization and predissociation in the lower rotational channel and η' is the electron fraction that is directly ejected from the lower rotational channel down-potential into fieldionization. Since both the excitation and coupling between the rotational channels involves the low angular momentum fraction of the electron wave, η will not differ much from η'. Note that Eqs. 3.6 and 3.7 are in fact Eq. 3.1 with a different excitation amplitude.

The three-channel competition in two rotational channels is depicted in Fig. 3.4b. The dotted line is fieldionization from the high rotational channel. The intensity at the saddlepoint is quenched by competition with the combination of rotational diffusion and predissociation. The rate of predissociation is chosen to be equal to the rate of rotational diffusion, 1 $10^{15}/n^3$ s^{-1}. The dashed line is the fieldionization from the lowest rotational channel via rotational diffusion. At the saddlepoint of the higher rotational channel most of the population entering the lower rotational channel by rotational diffusion will fieldionize. Close to the saddlepoint of the lower rotational channel, however, the competition with predissociation will quench the fieldionization via rotational diffusion in the lower rotational channel. The total average photoionization yield is given by the upper solid line. Since the predissociation rate and the rotational diffusion rate are chosen to be equal, C = 1/2. For comparison, the lower

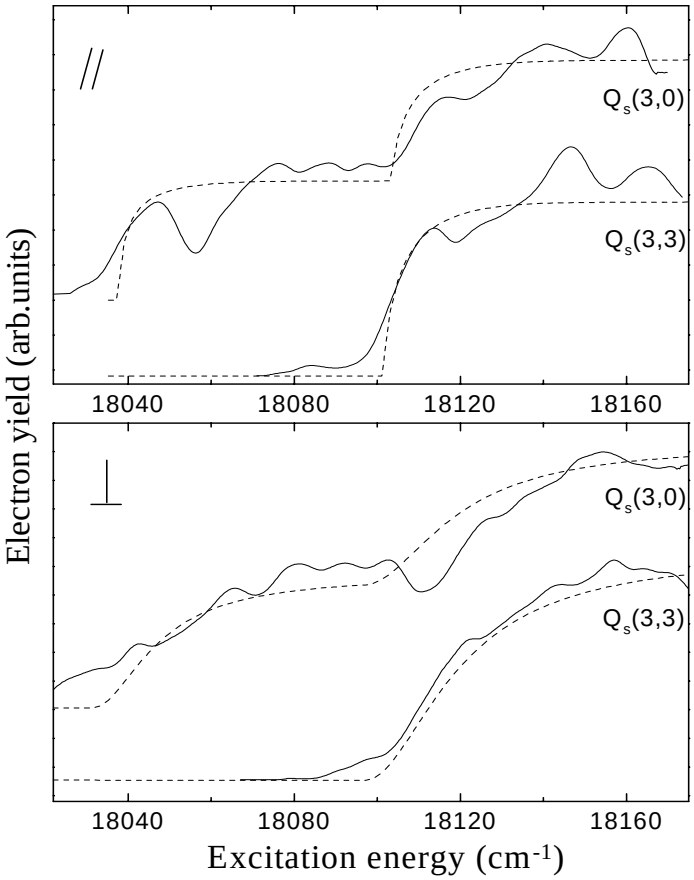

Figure 3.5: *The spectra shown in Fig 3.3 convoluted with a Gaussian of 5 cm^{-1} to show the average behavior of the fieldionization (solid lines). The spectra are fitted with $S_{\mathrm{RD}} = S_{\mathrm{DIS}} = 0.15$ (dashed lines).*

solid line shows the average photoionization yield if the predissociation rate is five times faster.

For a fit of the experimental data, there are two free parameters: S_{RD} and S_{DIS}, or S_{RD} and ζ. In case of ammonia we are helped by the selection rule $\Delta K^+ = 0$. The detected spectra via the two-photon excitation of the $Q_s(3,3)$ of the $\tilde{C}'^1A_1'(0000) \leftarrow \tilde{X}^1A_1'(0000)$ transition virtually has no fieldionization via rotational diffusion. The spectra can be fitted with a pure two-channel competition model between fieldionization and predissociation as described with Eqs. 3.1 and 3.3. This provides the rate of predissociation. We assume that this rate does not change for the spectra via the $Q_s(3,0)$ or the $Q_s(3,1)$. In our three-channel competition model we can than find the probability for rotational diffusion. In Fig. 3.5 the fits (dashed lines) are shown for the spectra from Fig. 3.3 that are convoluted with a Gaussian of 5 cm^{-1} (solid lines). It turns out that the predissociation and rotational diffusion rates are about equal ($\zeta = 1$)

and $S_{\mathrm{RD}} = S_{\mathrm{DIS}} = 0.15$ is the best fit, which corresponds to $\Gamma_0 = 1\ 10^{15}\ \mathrm{s}^{-1}$. The error in the fit is less than a factor 2. The average rates of the Rydberg states can be found by Γ_0/n^3 for zero-field (or for the separate Rydberg-Stark states Γ_0/n^4 in an electric field). For a $n = 30$ Rydberg state the decay time is about 27 ps both for rotational autoionization and for predissociation. Hence, the effective decay time is about 14 ps which corresponds well to the lifetime we observed in Fig. 3.2. The difference in the average photoionization yield upon parallel or perpendicular excitation is due to a larger η in the parallel case: At maximum half the excitation amplitude is directly ejected down potential into fieldionization. Upon perpendicular excitation all electron amplitude first has to scatter before going into fieldionization.

The slow modulation in the experimental data is attributed to coupling of the Rydberg series converging to $N^+ = 3$ with the Rydberg series converging to $N^+ = 4$. For a fit including the modulations a full MQDT simulation is needed like in chapter 2 and 4.

3.5 Conclusion.

We have demonstrated a novel method to retrieve the predissociation rates and rotational autoionization rates of the vibrationless Rydberg series of a molecule from the fieldionization spectra. We derived relatively simple formulae for a fit of the overall behavior of the fieldionization spectra. In our experiment we found that the average predissociation rate of the Rydberg series converging to the vibrationless $N^+ = 3$ ionic state of ammonia is about equal to the average rotational diffusion rate to the Rydberg series converging to the vibrationless $N^+ = 2$ ionic state, namely $1\ 10^{15}/n^3\ \mathrm{s}^{-1}$.

'Therefore he came to conclude that the time he was thinking about could be stretched in a thousand ways like dough made with egg yolks, as he had seen the women at La Griva knead it.'

Umberto Eco, L'isola del giorno prima.

Part 2

The excited electron coupled to the core electrons.

In the second part of this thesis we consider the situation in which the ionic core of the excited electron is not a closed shell. The core has some internal structure that couples with the excited electron. In chapter 4 the noble gas xenon is excited such that one electron is in a Rydberg state. Upon excitation it leaves a hole behind in the closed shell core of the ground state. The Xe ionic state with the hole can be in two energetically different spin-orbital states. A coupling of the Rydberg electron that is excited in the upper spin-orbital state with the continuum of the lower spin-orbital state may lead to the autoionization of the Rydberg electron. We have monitored the competition between autoionization and fieldionization.

In chapter 5 and 6 the opposite situation is taken: Magnesium has two valence electrons. If one electron is excited to a Rydberg there is one extra electron at the core. The Rydberg electron does not autoionize unless the so-called *isolated core electron* is excited with a laser pulse and, subsequently, exchanges energy with the Rydberg electron. Autoionization is monitored while changing the duration and frequency of the laser pulse that excites the isolated core electron.

Chapter 4

Two-channel competition of autoionizing Rydberg states.

Experimental data on the decay of xenon Stark states converging to the upper spin limit are presented. In an electric field the Rydberg electron has two qualitatively different decay paths. If the electron changes the core state from the upper spin state into the lower spin state, it gains sufficient energy to escape the ionic core and autoionizes. Moreover, if the electronic state is above the saddlepoint, created by the electric field, it can fieldionize. The probability to autoionize is nearly constant around the saddlepoint whereas the probability to fieldionize rapidly increases above the saddlepoint. With the velocity map imaging technique we monitor both ionization channels as a function of (increasing) photoexcitation energy. We observe that the fieldionization channel dominates the competition and gains yield at the expense of the autoionization channel. The spectra are explained both with full quantum calculations and with a relatively simple description for the overall behavior. These experiments show that the fieldionization can be used in general as a clock for total core-dependent decay.

4.1 Introduction.

In chapter 2 we investigated the fieldionization yield above the saddlepoint energy of the nitric oxide molecule in a strong electric field. A competition between the fieldionization and predissociation of NO is observed. The fieldionization yield just above the saddlepoint was strongly reduced by the predissociation channel and the ionization threshold appeared to have shifted to higher energy. Fitting the fieldionization spectrum with the equations derived in chapter 2 yielded the rate of predissociation. In that experiment only the fieldionization channel was monitored. To investigate a two-channel competition properly, however, one wants to monitor the two channels simultaneously. An ideal system of investigation is the autoionization from the Rydberg states converging to the upper spin state of a noble gas in a strong electric field.

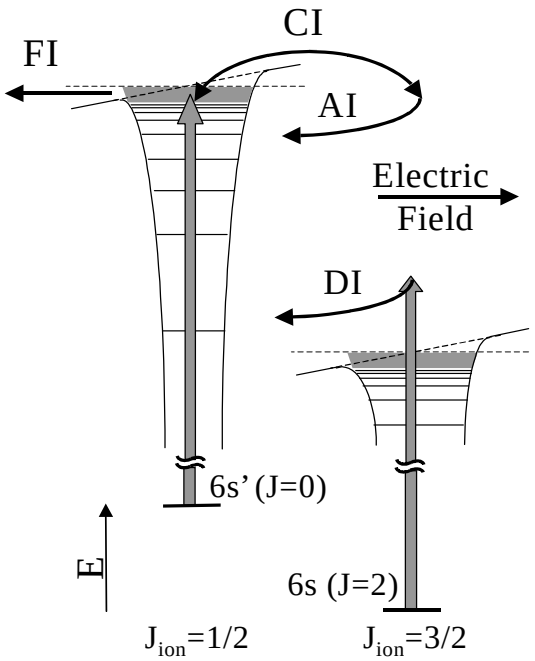

Figure 4.1: *Excitation scheme of the two-channel measurements. There are two initial metastable states, 6s′ (J = 0) and 6s (J = 2), that are excited with an optical pulse. In the J_{ion} = 1/2 channel the electron is promoted to a highly excited Rydberg state. Above the saddlepoint the electron can be fieldionized (FI). The J_{ion} = 1/2 channel is coupled to the J_{ion} = 3/2 channel by configuration interaction (CI). If the spin state of the ionic core is changed the excess energy is donated to the electron that autoionizes (AI). The initial state in the J_{ion} = 3/2 channel is somewhat higher in energy compared to its ionization limit than the one in the J_{ion} = 1/2 channel. Laser excitation results in direct ionization (DI) of the electron into the continuum.*

The fieldionized electrons have nearly zero kinetic energy whereas the electrons that autoionize by changing the core spin-orbit state, carry a kinetic energy of 1-2 eV, which makes the two ionization channels separable. The two channels are distinguished by velocity map imaging. The detected spectra, as presented in section 4.3, are simulated by full quantum calculations based on multichannel Stark theory [34, 35]. Moreover, we show that the overall behavior of the spectra can already be simulated by relative simple rate equations. In section 4.4 we adjust the parameters from chapter 2 to this specific experiment and compare with the experimental observations.

4.2 Experimental scheme.

Xenon is chosen to monitor the competition between fieldionization and autoionization. The spin-flip energy is 1.3 eV. A difficulty, however, is the high excitation energy. This is overcome by populating highly excited, metastable states of the Xe atoms by electron impact. The excitation scheme is shown in Fig. 4.1. The metastable states are the $6s'$ (J = 0) at 76197.3 cm^{-1} and $6s$ (J = 2) at 67068.0 cm^{-1} above the ground state [4], where J is the total angular momentum. The electron is optically excited to Rydberg states converging to the ion with $J_{ion} = 1/2$ at 108371.4 cm^{-1} above the ground state, and the states converging to the ion with $J_{ion} = 3/2$ at 97834.4 cm^{-1} [4]. With a typical field strength of 900 V/cm and excitation energy of 32174 cm^{-1} an electron in the $J_{ion} = 1/2$ channel can be fieldionized (FI) with nearly zero kinetic energy. Configuration interaction (CI) by spin orbit coupling between the two channels results in autoionization (AI). An autoionized electron carries an excess kinetic energy of 10537 cm^{-1} (1.3 eV). The energy difference between the two metastable states is smaller than between the two ionization limits. The same laser excitation from the 6s (J=2) metastable state will result in direct ionization (DI) into the continuum of the $J_{ion} = 3/2$ channel. The excess kinetic energy of the directly ionized electron is in this case 1408 cm^{-1}. Upon laser excitation of 32174 cm^{-1} we thus have to distinguish between electrons of three different kinetic energies, 0 (FI of the upper spin state), 1408 (DI of the lower spin state) and 10537 cm^{-1} (AI from the upper spin state). Note that the DI process is independent of the two other processes since it is due to the decay of another excited state.

The experimental set-up is depicted in Fig 4.2. A jet of Xe is produced by a pulsed valve with a backing pressure of 2.0 bar. The gas is led through a hot, tungsten filament [68]. Electrons from the filament are accelerated along the Xe beam by a repeller, electron optics and an electromagnet. Xe is excited to several metastable states by the electron bombardment. Charged particles are separated from the neutral beam by deflection plates. Only the $6s'$ (J = 0) and $6s$ (J = 2) metastable states survive the time of flight ($\sim \mu$s) to the interaction region, with an observed population ratio of 1:10. In the interaction region the atoms are subject to a variable, static electric field between a repeller plate and an extractor. The optical excitation with a narrowband laser around 32174 cm^{-1} is done in two ways: (I) A Quanta-ray Nd:YAG laser pumped Scanmate Dye laser produces pulses around 622 nm (16077 cm^{-1}) with an energy of 5 mJ, a duration of 7 ns and a bandwidth of 0.2 cm^{-1}. The laser pulse is frequency doubled with a KDP-R6G crystal to populate Rydberg states with a one-photon excitation. (II) An alternative way to excite the electron is to tune the same dye-laser to around 747 nm (13387 cm^{-1}) and send the pulse to the interaction region colinear with the second harmonic of the Nd:YAG laser (532.2 nm or 18790 cm^{-1}, with a bandwidth of 0.5 cm^{-1}, referred to as 'Nd:YAG' from now on) in a 1 + 1' excitation scheme[1].

[1]The more obvious 1 + 1 excitation with 622 nm shows resonant structure at the one-photon level and is not used.

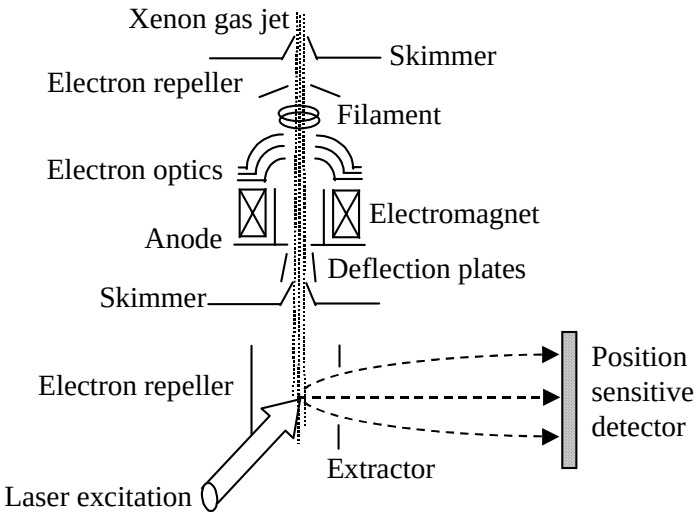

Figure 4.2: *Schematic outline of the experimental set-up. A xenon gas jet is led through a hot tungsten filament and two skimmers. Electron bombardment, guided by a set of electron optics and an electromagnet, excites the Xe atoms to metastable states. Charged particles are separated from the neutral beam by deflection plates. The metastable Xe is futher excited by laser light, with a polarization perpendicular to the electric field in the interaction region. Electrons that ionize are accelerated towards a position sensitive detector by means of a repeller plate and an extractor ring. The position of the electron signal depends on the kinetic energy of the electron perpendicular to the electric field.*

In an electric field of typically 200-1000 V/cm the kinetic energy difference of 1.3 eV between a fieldionized electron and an autoionized electron cannot easily be distinguished by time of flight. However, velocity map imaging [69] is excellently suited to measure kinetic energy differences in the presence of a strong electric field. The polarization of the excitation laser is chosen perpendicular to the electric field. The electrons that autoionize carry an excess kinetic energy perpendicular to the direction of the electric field. The outgoing electron density is accelerated towards a position sensitive imaging detector consisting of a set of multichannel plates and phosphor screen, viewed by a CCD camera. The CCD image shows a two-dimensional projection of the electron probability at a particular time (the arrival time at the detector) after ionization.

4.3 Results and discussion.

Fig. 4.3 shows a typical CCD image of the velocity map imaging. The electric field is 900 V/cm. The photo excitation is just above the saddlepoint, with a polarization perpendicular to the electric field (along the x-axis of the image in Fig. 4.3). The

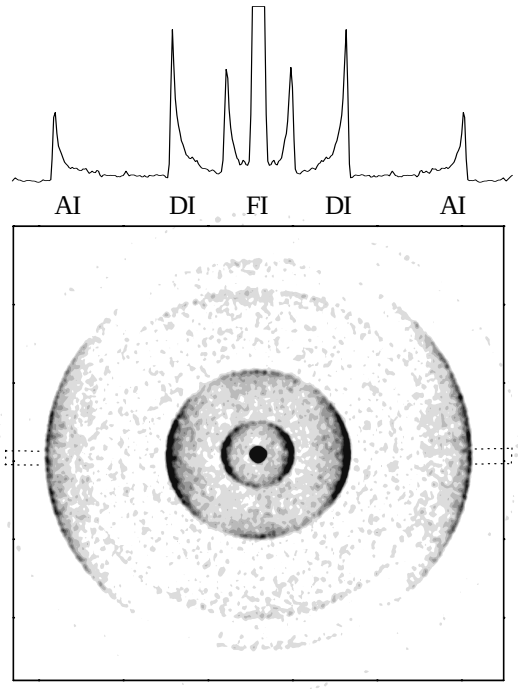

Figure 4.3: *A typical image of velocity map imaging. The central spot with the fieldionization signal (FI) is very intense and off-scale. The small inner ring is a fraction of the fieldionization signal that has scattered off the ionic core. The large inner ring is the direct ionization (DI) and the outer ring corresponds to the autoionization (AI). On top a horizontal slice through the middle of the image is shown.*

strong dot in the center of the image corresponds to the fieldionization yield (FI). The small inner ring is a fraction of the fieldionization that has scattered of the ionic core. The intensity of such a ring is less than 10% of that of the central dot. The large inner ring corresponds to direct ionization (DI)) and the outer ring to autoionization (AI). Shown on top of the image is a horizontal slice through the middle of the image. Velocity map imaging is based on the relation between the excess kinetic energy of an electron perpendicular to the direction of the electric field and the radius of the ring of electron signal on the CCD image. The maximum radius is proportional to the square root of the kinetic energy. Only at very low energies, up to 200 cm^{-1}, does the radius exhibit a more complicated function of kinetic energy, like is seen with the fieldionization in Fig. 4.3. A more detailed discussion about the angular distribution of electron density on the image and the features at low kinetic energy is found in Ref. [70].

The radial electron density distribution is obtained by angularly integrating the electron signal as a function of distance from the center of the image. Fig. 4.4 shows the radial distributions of ionization yield upon various excitation wavelengths in a

field of 900 V/cm. The spectra are plotted as a function of the number of pixels from the center of the images. As a test experiment only the second harmonic Nd:YAG photons with an energy of 18790 cm^{-1} are used. The detected radial distribution is shown in the lower trace in Fig. 4.4. The strongest feature e) results from two photon ionization in the $J_{ion} = 3/2$ channel, yielding a kinetic energy of 6814 cm^{-1} above the zero-field ionization limit of 97834 cm^{-1}. The small features at pixel 120 and 205 are, respectively, direct ionization in the $J_{ion} = 1/2$ channel (d) and direct ionization from the 6s' (J = 0) state into the $J_{ion} = 3/2$ channel (g).

Excitation with an ultraviolet pulse of 32012 cm^{-1} (UV) results in the radial distribution that is shown in the middle trace of Fig. 4.4. Feature a) is fieldionization in the $J_{ion} = 1/2$ channel, feature f) is autoionization from the $J_{ion} = 1/2$ channel to the $J_{ion} = 3/2$ channel and feature b) is direct ionization in the $J_{ion} = 3/2$ channel. Conversion to kinetic energy E_{kin} of the electron (the component perpendicular to the electric field) is obtained by

$$E_{kin} = c * (\text{pixel})^2 \tag{4.1}$$

where c is an experimental value depending on the fields used and distances of the phosphor screen and CCD camera from the interaction region. In this case c = 0.375 cm^{-1}. At the maximum radius of the signal the kinetic energy component perpendicular to the electric field is equal to the total kinetic energy of the electron. There are two reasons not to plot energy on the x-axis in Fig. 4.4. Firstly, the high-energy side of the spectra becomes stretched so much that it becomes hard to see the low-energy side. Secondly, there is the question of the binding energy of the electron. Starting with a metastable state the electron has a certain binding energy to overcome in order to ionize. For direct ionization the binding energy is the zero-field ionization energy. If the electron scatters of the core and fieldionizes the binding energy is the saddlepoint energy, which is 183 cm^{-1} lower in a field of 900 V/cm. The difference is small at the high energies around 15000 cm^{-1}. At low energies, however, the difference becomes important and one would expect the peak at b) at pixel 61 instead of 57 if one assumes the saddlepoint energy (rather than the zero-field energy) as binding energy.

For the two-channel competition experiments we chose to excite the Xe metastable states with a combination of a red pulse around 13222 cm^{-1} (R) with the second harmonic of a Nd:YAG laser (18970 cm^{-1}). The radial distribution of electron yield is shown in the upper graph in Fig. 4.4. There are two advantages of this excitation scheme over single-photon excitation of the metastable states by a UV pulse: As can be seen in Fig. 4.4 the relative intensity of the FI and AI signals (features a) and f)) as compared to the DI signal (b) greatly enhances upon using the R + Nd:YAG combination. The electron yield of a) and f) is increased with the help of the $6p'$ J = 1 state at 89279 cm^{-1}. Although about 140 cm^{-1} off resonance, the large oscillator strength of the $6p'$ state relatively enhances the integrated yield from the fieldionization FI and autoionization signal AI from the $J_{ion} = 1/2$ channel to be equal to the direct ionization signal DI of the $J_{ion} = 3/2$ channel.

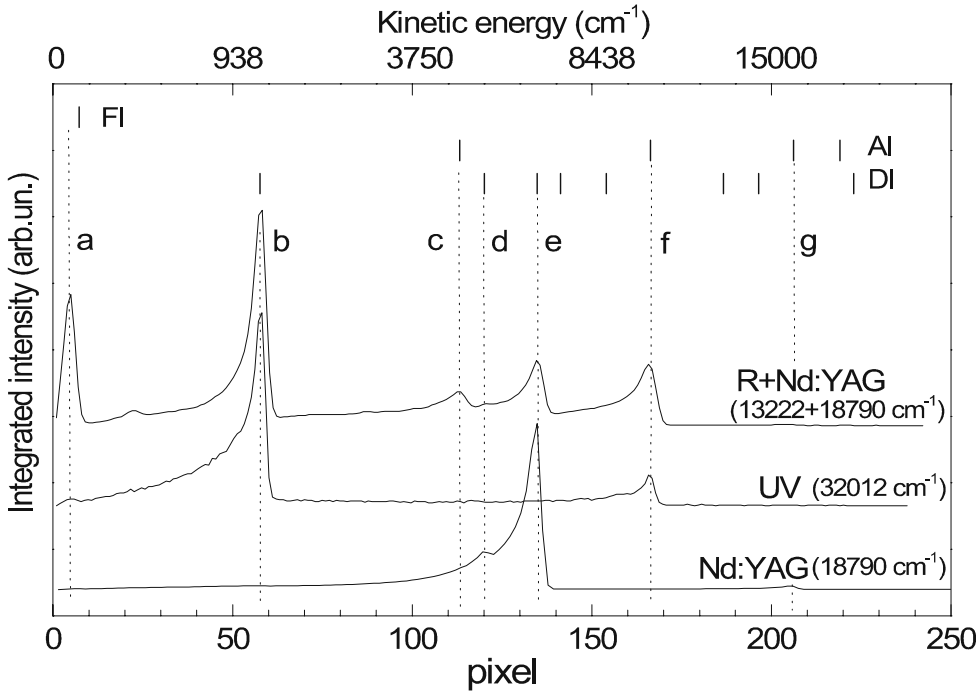

Figure 4.4: *Radial distribution of electron yield of the velocity map imaging upon various excitations. Metastable Xe is excited with the second harmonic of a Nd:YAG laser at 18790 cm^{-1} (532.2 nm; Nd:YAG), with an ultraviolet pulse of 32012 cm^{-1} (312.4 nm; UV) or with simultaneously a red pulse at 13222 cm^{-1} (756.3 nm; R) with the second harmonic of a Nd:YAG laser. The electric field is 900 V/cm. Indicated on top are the expected maximum radii of fieldionization (FI), autoionization (AI) and direct ionization (DI), based on the involved excitation energies and an empirical c = 0.375. The most prominent features are denoted: a) fieldionization in the J_{ion} = 1/2 channel, b) Direct ionization in the J_{ion} = 3/2 channel. c) Autoionization from the J_{ion} = 1/2 channel to the J_{ion} = 3/2 channel with two red photons. d) Direct ionization in the J_{ion} = 1/2 channel with two Nd:YAG photons. e) Direct ionization in the J_{ion} = 3/2 channel with two Nd:YAG photons. f) Autoionization from the J_{ion} = 1/2 channel to the J_{ion} = 3/2 channel.*

One new feature appears (c), which is attributed to photoionization of the metastable state in the $J_{ion} = 1/2$ channel excited with two red photons, autoionizing into the $J_{ion} = 3/2$ channel. The second reason to detect the FI and AI from the $J_{ion} = 1/2$ channel with a combination of excitation lasers is that the autoionization from the $J_{ion} = 1/2$ channel to the $J_{ion} = 3/2$ channel ($|D_{\mathrm{AI}}|^2$, see section 4.4) in case of UV excitation is always strong; the AI signal remains more or less constant upon increasing excitation energy above the saddlepoint energy. We have no explanation for the large $|D_{\mathrm{AI}}|^2$ in this particular case.

Integration windows are set over the FI, DI and AI signals and the total electron yield is monitored as a function of the excitation energy. The windows are set at 0-15, 16-65 and 140-170 pixels, respectively. We assume that the DI signal is frequency independent and first divide the FI and AI signals by the DI yield in order to remove intensity fluctuations of the laser. In Fig. 4.5a the observed integrated electron yield from the fieldionization is shown as a function of the energy of one red plus one Nd:YAG photon. The saddlepoint at 900 V/cm is at 31991 cm^{-1}. The FI electron yield is increasing over an energy range of about 25 cm^{-1} above the saddlepoint. Simultaneously the AI signal is decreasing as shown in Fig. 4.5b. Note that the Stark structure is well resolved. The observed spacing between the states is 3.1 cm^{-1}. The $n = 26$ manifold is expected to be around 32012 cm^{-1}. In a field of 900 V/cm the hydrogenic spacing between the Stark states of $n = 26$ is 3.0 cm^{-1} corresponding well with the observed spacing. There is a strong resonance in the AI signal at 32008 cm^{-1} seen in Fig. 4.5b. This is, however, an experimental artifact: In the radial distribution (not shown) is seen that at this wavelength two new rings appear, one of which falls in the AI window[2].

Also plotted in Figs. 4.5a and 4.5b are the theoretical fits based on a full MQDT calculation. The Stark structure is well reproduced. Adding the two spectra results in the absorption cross section. The calculations are based on the method described in detail in Ref. [34], giving the details for obtaining the outgoing wave functions and dipole matrix elements for multi-channel atoms in a static electric field. The method uses zero-field channel coupling matrices and the transformation amplitudes from spherical-to-parabolic wave functions to obtain the full multi-channel wave function in the static electric field. For the competition studied here, we calculated all of the zero-field channel coupling matrices for Xe using an R-matrix calculation in LS-coupling; the jj-coupled channel interactions were computed through an LS-jj frame transformation and the K-matrices were empirically modified at the few percent level to improve agreement with the zero field, experimental energies.

[2]The rings correspond to excitation with two times Nd:YAG plus one red photon and three times Nd:YAG starting with the 6s (J = 2) in the $J_{ion} = 3/2$ channel, directly ionizing in the $J_{ion} = 1/2$ channel. The resonance is a coupling of a virtual level at two times Nd:YAG starting from the 6s (J = 2) state in the $J_{ion} = 3/2$ channel minus one red photon to the $5d'$ state (J = 2) in the $J_{ion} = 1/2$ channel at 91448 cm^{-1}. The ring corresponding to the two times Nd:YAG plus one red photon starting from the $J_{ion} = 3/2$ channel is almost on top of the AI ring in the radial distribution. Therefore there is an increase in electron yield in its integration window not related to the competition between AI and FI.

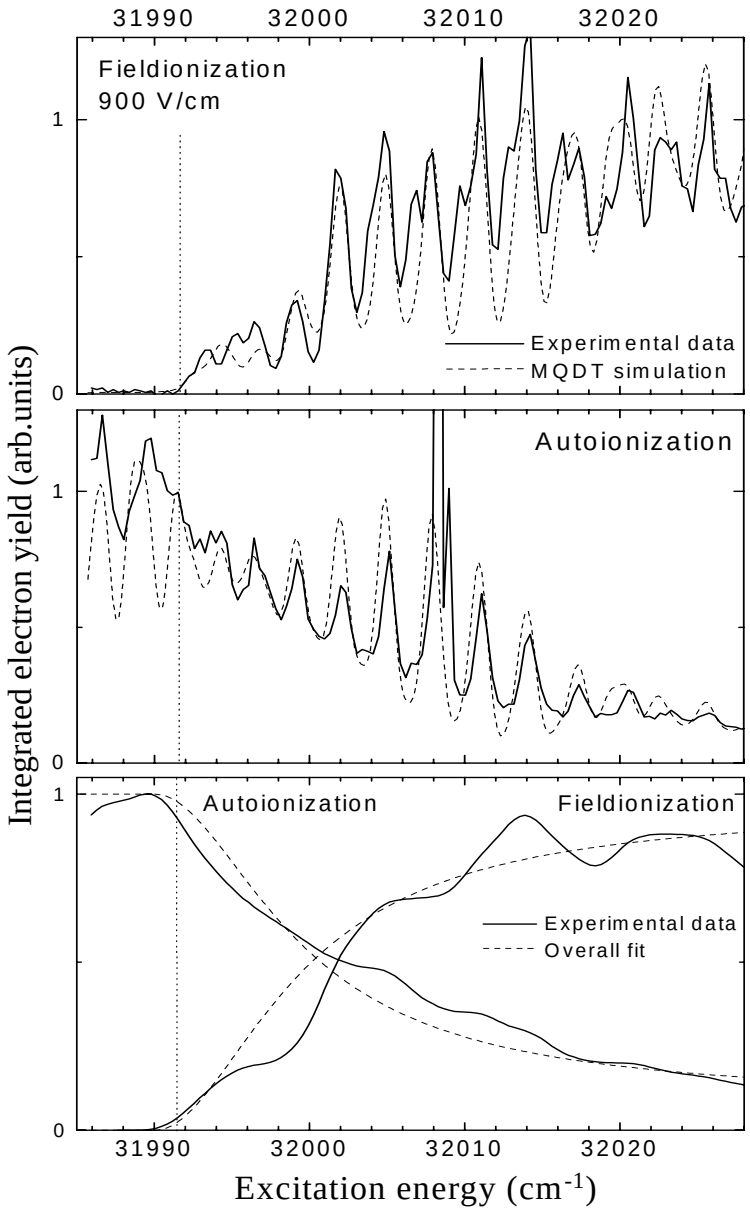

Figure 4.5: *a). Integrated electron yield of fieldionization (FI) in the J_{ion} = 1/2 channel as a function of the energy of one red and one Nd:YAG photon of 18790 cm^{-1}. The saddlepoint energy for the J_{ion} = 1/2 channel at 900 V/cm is 31991 cm^{-1} above the metastable state in the J_{ion} = 1/2 channel. The dashed line shows the simulation based on a full quantum calculation (see text). b) Same for autoionization (AI) from the J_{ion} = 1/2 channel to the J_{ion} = 3/2 channel. c) Both experimental spectra, convoluted with a Gaussian of 2 cm^{-1}. The dashed line is the overall behavior based on Eqs. (2) and (3) with S_{AI} = 0.17 and* $|D_{\mathrm{AI}}|^2 = 0.05$.

The two-photon dipole matrix elements in zero field were estimated by treating the absorption as only affecting the 6s electron in the initial state; it is most likely the dipole matrix elements are the least accurate part of the calculation.

Besides the spatial degrees of freedom of the escaping electron, there are three other important quantum numbers: J_{ion}-the total angular momentum of the Xe^+ core, Q-the angular momentum that results from coupling the spin of the Rydberg electron to J_{ion} of the core, and M_q-the projection of Q on the z-axis. The initial state of Xe can be described as $5p^5\ ^2P_{1/2}\ 6s\ J = 0$ with an equal population in each M level. The initial state has $J_{ion} = 1/2$, $Q = 0$, $M_q = 0$. The initial excitation mostly populates autoionizing states attached to the $J_{ion} = 1/2$ threshold because the photon mainly acts on the outer $6s$ electron. When the electron is near the core, the channel interactions allows the Rydberg electron to gain energy from the core and be ejected from the atom.

In Fig. 4.5c the same experimental spectra are depicted as in Figs. 4.5a and 4.5b, but convoluted with a Gaussian of 2 cm^{-1}(solid lines). The aim is to focus on the overall behavior of the electron yield. Above the saddlepoint, fieldionization becomes possible. In the absence of autoionization the onset of electron yield of fieldionization would be a sharp stepfunction, exactly on the saddlepoint energy. Coupling between the two channels $J_{ion} = 1/2$ and $J_{ion} = 3/2$ quenches the fieldionization intensity close to the saddlepoint. A slow rise of fieldionization and a slow decrease of autoionization above the saddlepoint is observed. The exact overall behavior of the spectra depends on the competition between the two channels. Instead of a full MQDT simulation of the spectra, a good, qualitative picture of the overall behavior of the spectra as shown in Fig. 4.5c can already be obtained using an approximate description.

4.4 Simulation of overall behavior.

The formulae for the overall behavior are derived in chapter 2. The dotted lines in Fig. 4.5c are theoretical predictions based on Eqs. (2.13) and (2.14). In the energy range from saddlepoint energy (31991 cm^{-1} in a field of 900 V/cm) to zero-field ionization potential (32174 cm^{-1}) the term S_{FI} changes from 0 to 1. Autoionization in Xe with a probability S_{AI} takes the role of S_{DIS} of predissociation in NO. S_{AI} is a constant so that the branching ratio B_{FI} changes from 0 to $1/(S_{\mathrm{AI}} + 1)$. The best result is obtained with $S_{\mathrm{AI}} = 0.17 \pm 0.05$ and a constant offset $|D_{\mathrm{AI}}|^2 = 0.05$, where $|D_{\mathrm{AI}}|^2$ is similar to $|D_{\mathrm{DIS}}|^2$ for predissociation in Eq. 2.14. The fieldionization rates are known from the calculation and therefore we can extract the autoionization rate. Xe autoionization rates are only known in zero-field [71–74]. We can directly calculate the S_{AI} from the zero field S-matrix from our theoretical data; for $M = 2$, the autoionizing states attached to the $J_{ion} = 1/2$ threshold with $Q = 0$ gives $S_{\mathrm{AI}} = 0.21$ which is in good agreement with the fitted result.

It is perhaps surprising that the value of S_{AI} should turn out to be smaller for this experiment on Xe than our previous experiment on NO (S_{AI} =0.25), as described in

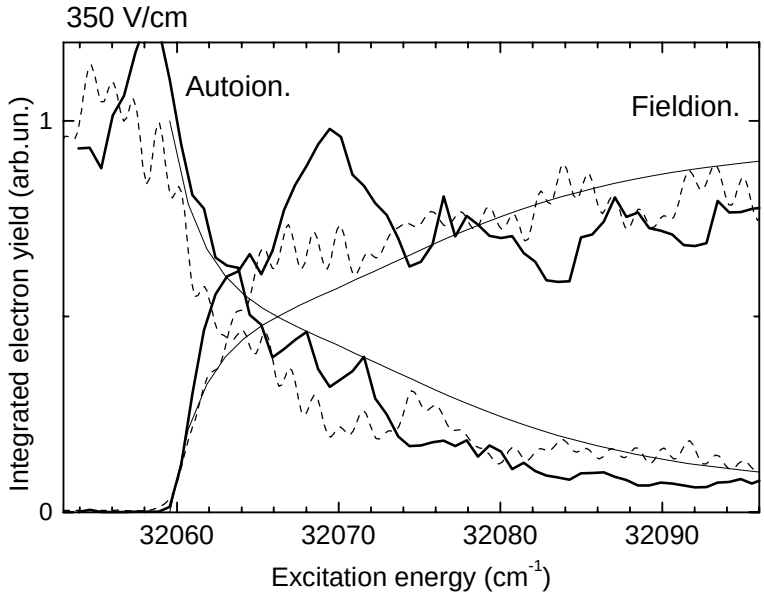

Figure 4.6: *Integrated electron yield of autoionization (AI) from the J_{ion} = 1/2 channel to the J_{ion} = 3/2 channel versus fieldionization (FI) in the J_{ion} = 1/2 channel as a function of the energy of one red and one Nd:YAG photon of 18790 cm^{-1}. The spectra are convoluted with a Gaussian of 1 cm^{-1}. The electric field is 350 V/cm (saddlepoint at 32060 cm^{-1}). The dotted line is the simulation based on a full quantum calculation. The thin solid lines are the overall behavior based on Eqs. (2.13) and (2.14) with $S_{\rm AI}$ = 0.17 and $|D_{\rm AI}|^2 = 0.05$.*

chapter 2. On average, the predissociation rates for NO [28, 75, 76] are substantially smaller than the autoionization rates in Xe. This paradox is solved by noting that the current experiment excites very specific Rydberg resonances: Q (the angular momentum that results from coupling the spin of the outer electron to the total angular momentum of the core) must initially be zero. Some of the broadest Xe resonances (for example, the $J = 1$ *nd* series) have $Q = 1$. If the experiment would probe $Q = 1$ Rydberg states, the observed value of $S_{\rm AI}$ should increase dramatically (e.g. for the $J_{ion} = 1/2$, $Q = 1$ state, $S_{\rm AI}$ is 7.5).

The $S_{\rm AI}$ value is a constant for the xenon atom for a given Q channel, independent of excitation energy and the field strength. To demonstrate this, the same experiment was repeated at a lower electric field. In Fig. 4.6 are shown the AI and FI signals after convolution of 1 cm^{-1} in a field of 350 V/cm. The saddlepoint in such a field is at 32060 cm^{-1}. The dotted lines are the results obtained with a full quantum calculation. The thin solid lines are the overall behavior based on Eqs. 2.13 and 2.14, showing again the power of this simplified model. The only parameter that is adjusted in the fit is the new field strength of 350 V/cm, $S_{\rm AI}$ is kept at 0.17, and $|D_{\rm AI}|^2 = 0.05$.

4.5 Conclusion.

We have demonstrated the competition between two ionization channels in xenon, fieldionization and autoionization, in the presence of an electric field. Due to the different mechanisms of decay the ratio between the two channels changes from zero at the saddlepoint to infinity at the zero-field ionization threshold. The overall behavior of the fieldionization yield spectrum is dictated in a unique way by the core-dependent autoionization rate. Fitting the fieldionization spectrum with the formulae derived in chapter 2 allows us to retrieve the total core-dependent decay rate. Since the overall fieldionization rate of high Rydberg states of any atom or molecule is the same within a factor of two, depending on the quantum defects, the fieldionization spectrum can be used as a clock to find the rate of total core-dependent decay. This general aspect can be very important for systems were it is impossible to detect core-dependent decay directly.

Chapter 5

Stepwise electron emission from magnesium Stark states.

Investigations of time dependent autoionization of doubly excited magnesium atoms in a strong electric field are reported. A narrow band laser excites one electron towards a 3s16k Stark state and subsequently the second electron is excited with a short laser pulse. The autoionizing electron yield shows a stepwise decay which is detected by a streak camera with picosecond resolution. Quantum calculations are in good agreement with the experimental results.

5.1 Introduction.

Decay of an autoionizing two-electron atom involves a doubly excited state coupled to a state in which one electron is ejected while the second electron relaxes to a deeper bound state. If one of the excited electrons is in a Rydberg state, only the fraction of the Rydberg wavefunction close to the nucleus can exchange energy with the excited core electron. At higher principle quantum number n the wavefunction spends less time at the core, hence the decay time scales with the oscillation period of the Rydberg electron. The emitted electron flux of such an autoionization process is most often *exponential* in nature.

We present a combined experimental and theoretical study of a *stepwise* decay of the electron flux. A long pulse dye laser excites the Mg ground state atoms ($3s^2$) to a stationary Rydberg state ($3sn\ell$). The excitation pulse is much longer than the classical orbit time of the Rydberg state and the electron density is spread over the complete trajectory. Since only one electron is excited, autoionization is not yet possible.

The key element for stepwise decay is that the second electron is excited with a laser pulse of short duration with respect to the classical period of the spectating Rydberg electron. The initial Rydberg eigenstate $3sn\ell$ is projected onto final autoionizing states in the $3pn'\ell'$ Rydberg series. The Rydberg electron experiences a change in potential

upon excitation of the core electron which induces a shake up from the initial $n\ell$ Rydberg state to final $n'\ell'$ state. If the excitation pulse is short compared to the oscillation period, a coherent superposition of autoionizing final states, or a wavepacket, is created.

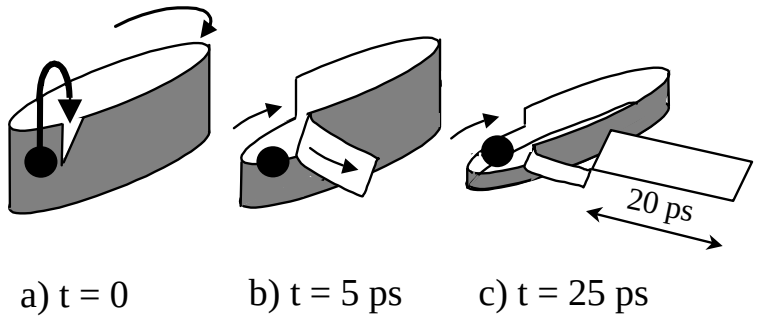

Figure 5.1: *Intuitive picture for stepwise decay. In the initial state one electron is in a high Rydberg orbit. The electron density is depicted as the gray ribbon around the black core. At t = 0 a short laser pulse excites the inner electron creating an exit for the outer electron. The autoionization probability (50% here) is constant and the electron emission has a constant intensity during a complete roundtrip period of 20 ps in this example. After one roundtrip time there is less electron density to autoionize and the outgoing flux will suddenly drop and remain constant again during the second roundtrip period.*

An intuitive picture of stepwise decay is given in Fig. 5.1. Most of the initial Rydberg wavefunction is far away from the nucleus during the excitation of the core electron as depicted as the gray ribbon in Fig. 5.1a. The fraction of the initial Rydberg wavefunction that happens to be near the core during excitation can autoionize ($3pn'\ell' \rightarrow 3s\epsilon\ell''$) which results in electron emission. We define the parameter γ to be the probability for the Rydberg electron to autoionize during one collision with the core electron (50% in Fig. 5.1). The remainder (1-γ) will leave the core unaffected and persists in its bound orbit. The outgoing electron flux will remain constant during one oscillation period since the Rydberg density far from the nucleus is unaffected by the short excitation (Fig. 5.1b). After one oscillation period all of the Rydberg density is reduced and the fraction originally near the core returns. At that time the incoming density is reduced and the autoionization flux suddenly decreases to $\gamma(1-\gamma)$. This reduced electron emission remains constant for a second Rydberg oscillation period and so on (Fig. 5.1c). The result is a series of steps in the outgoing electron flux.

Already in 1991 Wang and Cooke [77] predicted this stepwise decay behavior for a Rydberg electron that initially oscillates in the radial coordinate [78], after sudden Isolated Core Excitation (ICE) [79,81,82]. In the original proposal by Wang and Cooke one electron is excited into a high n ($n = 65$) Rydberg state where the energy spacing between Rydberg states is nearly constant. Although starting from an eigenstate, the

sudden ICE creates a superposition of final, autoionizing, states. The emitted electron flux exhibits a stepwise decay with time steps of the radial oscillation period, $\tau = 2\pi n^3$.

We report on the observation of stepwise decay by probing the electron emission of an autoionizing Rydberg atom in a strong, static electric field after ICE. The angular momentum ℓ of a Rydberg electron in an electric field is no longer conserved and the Rydberg state splits up into a manifold of n Stark states. We excite the initial Stark state 3sn$k$ to an autoionizing Stark state 3pn$'k'$ with a short pulse. A Stark state is a superposition of all angular momenta in that manifold. All angular momenta of the final Stark wavepacket oscillate between the extreme values $\ell = 0$ and $\ell = n$ - 1 [13, 80]. Only low angular momentum wavepackets penetrate into the core region ($r_{min} \sim \ell(\ell+1)$) and thus can interact with the, now excited, inner electron [83]. As a result, only the fraction of the wavepacket with low angular momentum character has a chance to autoionize. Since all angular momenta eventually evolve to low angular momentum, the autoionization rate remains constant for a complete angular oscillation period after which it drops suddenly with γ. The intuitive picture in Fig. 5.1 is now in ℓ-space. The electron emission will show a stepwise decay with a step time given by the angular momentum oscillation rather than the radial oscillation period as in the proposal by Wang and Cooke [77].

5.2 Experimental.

In order to measure the electron flux, we have used the streak camera with picosecond resolution. A general description of the streak camera is given in chapter 1, an interpretation of the image is worked out in detail in chapter 8. For this experiment an effusive beam of Mg atoms, from a resistively heated oven, is excited in a crossed laser beam arrangement. A 7-ns laser pulse with a frequency in the region 650 to 655 nm and a bandwidth of 0.2 cm^{-1} is frequency doubled and excites the Mg atoms in a non-resonant two-photon process from the ground state to a Stark state $3s16k$. A second ($\lambda \sim$560 nm) pulse with a duration of 2 ps is frequency doubled and drives the inner electron 3s→3p transition. The interaction region lies between two plates (separation = 10.0 mm) over which a static electric field is applied. The second plate has a slit of 10×0.3 mm parallel to the beam direction through which the electrons can leave the interaction region. A set of Multi Channel Plates and a phosphor screen viewed by a CCD camera images the signal. In the trajectory of the electrons two deflection plates are placed with a fast sweeping electric field perpendicular to the direction of the electrons. Electrons arriving at different times in the deflection region experience a different deflection field and the time coordinate is converted to a position coordinate on the phosphor screen.

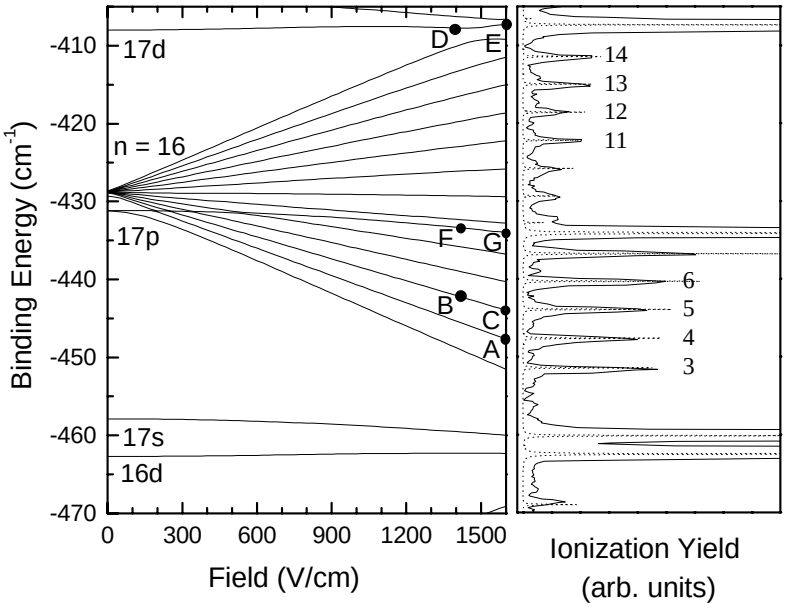

Figure 5.2: *(a) A calculated Stark map from the Mg n = 16 manifold in fields up to 1600 V/cm. (b) Experimental 3-photon resonant ionization yield spectrum at 1600 V/cm as a function of binding energy. The dotted line is the calculated 2-photon absorption cross section. The letters indicate the experimental positions in Figs. 5.3 and 5.4. The Stark states are labeled 3 - 14.*

5.3 Results and discussion.

In the experiment, the initial states are various Stark states of the $3s16k$ manifold in a field of 1400 or 1600 V/cm. In these fields, the spacing between the Stark states of a Hydrogen atom is 2.9 and 3.3 cm^{-1}, respectively, corresponding to angular oscillation periods of 12 and 10 ps respectively. We expect the angular oscillation period of the final Stark wavepacket in Mg to be close to these values. For comparison, the radial oscillation time for a $n = 16$ Rydberg state is 0.6 ps.

To classify the initial Stark states a calculated Stark map around the Mg $3s16k$ manifold in fields up to 1600 V/cm is shown in Fig.5.2a. In zero-field the singlet s, p and d quantum defects near $n = 16$ are 1.52, 1.05 and 0.60 respectively. The $17s$ and $16d$ states are about halfway between the $n = 15$ and 16 manifolds and only start mixing into the manifolds at high fields. The 17p-state is almost in the middle of the $n = 16$ manifold. Since it gains only s- or d-character at higher fields, it does not mix with the Stark states until relatively high fields. In Fig. 5.2b the experimental 3-photon resonant ionization yield spectrum at 1600 V/cm is shown as a function of binding energy. The s, p and d states are an order of magnitude stronger than the Stark states and off scale in the figure. The dotted lines in Fig. 5.2b are the calculations of the 2-photon absorption cross section. The positions of all peaks are

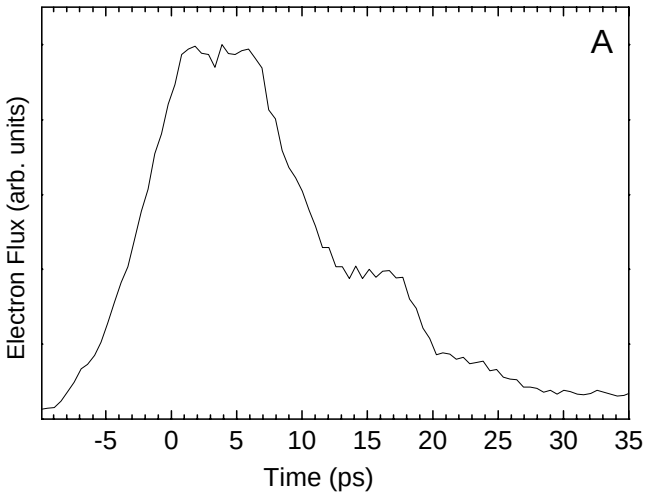

Figure 5.3: *The observed stepwise decay of the outgoing electron flux from the 3s16k state at position A in Fig. 5.2.*

accurately reproduced and gives us confidence that, concerning the initial states, the theory matches the experiment.

The narrowband excitation laser is fixed on a selected Stark state and the second UV laser pulse is applied to induce the $3s \rightarrow 3p_{1/2}$ transition at 280.4 nm. The near transform-limited pulse has a time duration of 2 ps which is short compared to the Stark period of the Rydberg electron. Fig. 5.3 presents the main observation of this chapter: the electron emission of the $3s16k$ state at the initial position A in Fig. 5.2 after sudden ICE is shown as a function of time. After a rise-time of about 5 ps the autoionization rate remains constant for 7 ps and than drops by 60% in 4 ps. In remains constant again for 5 ps before a second, equal drop in emission. The apparent shorter second and third period are caused by time smearing in the detector due to the large excess kinetic energy of the autoionizing electrons. From Fig. 5.3 we can deduce that the angular oscillation time is about 9 ps and the probability to autoionize is 60% per core passage.

Our calculations are based on the multichannel Stark theory developed in Ref. [34], the formulation of Isolated Core Excitations in Ref. [84], and the theory of time dependent ejection of electrons from autoionizing states in Ref. [85]. The main idea of the calculation is to use the energy eigenstates in the field as a basis to expand the time dependent wave function, $\Psi(\mathbf{r}, t)$,

$$\Psi(\mathbf{r}, t) = \int A(E) e^{-iEt} \psi_E(\mathbf{r}) dE \tag{5.1}$$

where ψ_E is the eigenstate and $A(E)$ is the amplitude of the final state E. The amplitude, $A(E)$, for exciting a state at energy E is the dipole matrix element times the amplitude that the laser contains a photon at the correct frequency. The basic part of the calculation uses the semiclassical treatment of the Stark problem in parabolic

coordinates [35] to obtain the initial state and the final eigenstates in the field. The final state is an autoionizing continuum state in which the only path for the electron to escape from the atom is by scattering from the core. As in Ref. [34], all of the zero field scattering parameters for both initial and final states are obtained from an R-matrix calculation in LS-coupling where the spin-orbit effects are incorporated by using an LS to jQ frame transformation [85].

There are two major difficulties that must be overcome in applying Eq. (5.1). The first is that the dipole matrix elements can not be obtained by direct numerical integration from an initial state. Instead we use the idea of Ref. [84] that the dipole matrix element between initial and final state is the *projection* of the initial Rydberg wave function onto the final eigenstates[1]. The second difficulty is that Eq. (5.1) is easiest to use for atomic distances ($< 10^5$ a.u.) and we must obtain the time dependent electron flux through a slit that is a macroscopic distance from the atom. Fortunately, the electric field hardly affects the ejected electron's trajectory within 10^4 a.u. of the nucleus because the ejected electron has a relatively high kinetic energy compared to the potential energy from the external field. This allows us to use the formulation of Ref. [85] to obtain the time dependent flux in any direction; we can use a linear combination of regular and irregular Coulomb functions for the energy eigenstates out to 10^4 a.u. From the time dependent wave function, $\Psi(\mathbf{r}, t)$, we calculate the angular dependence and the time dependence of the electron flux through a sphere of radius 10^4 a.u. A classical calculation uses the angle and time dependent flux at small distances $\sim 10^4$ a.u. as input to give the flux into the detector which is at $\sim 10^9$ a.u. from the atoms. The fraction of the total autoionizing flux that enters the streak camera mirrors the total flux.

To illustrate the differences in electron emission flux after excitation of the $3s \rightarrow 3p$ transition with a laser pulse of 2 ps, various $3s16k$ states are probed and compared to low-ℓ states in fields of 1400 and 1600 V/cm. The characters in Fig. 5.4 are the experimental positions indicated in Fig. 5.2. In Figs. 5.4B and 5.4C the electron emission after sudden ICE is depicted as a function of time, starting from a red Stark state. From this state we observe stepwise emission like in Fig. 5.3. There is no qualitative difference in the observed flux starting from the red Stark states. Only the reddest state shows a less clear stepwise emission. All spectra show the same step period of 11 ps at 1400 V/cm and 9 ps at 1600 V/cm. Blue Stark states were too weak to be observed. The ICE calculations (smooth lines) qualitatively agree with the experimental data. We observe the same period of decay. Intensity differences might be due to difficulties in simulating the time smear of the detector.

[1]From M.D. Lindsey *et al*, Phys. Rev. A **50**, 5058 (1994), this projection can be obtained from the Wronskian of the initial and final Rydberg state at a distance close to the nucleus. Thus, the dipole matrix element can be obtained in terms of the zero field K-matrices and the coefficeints that transfrom between the Stark states and zero field states.

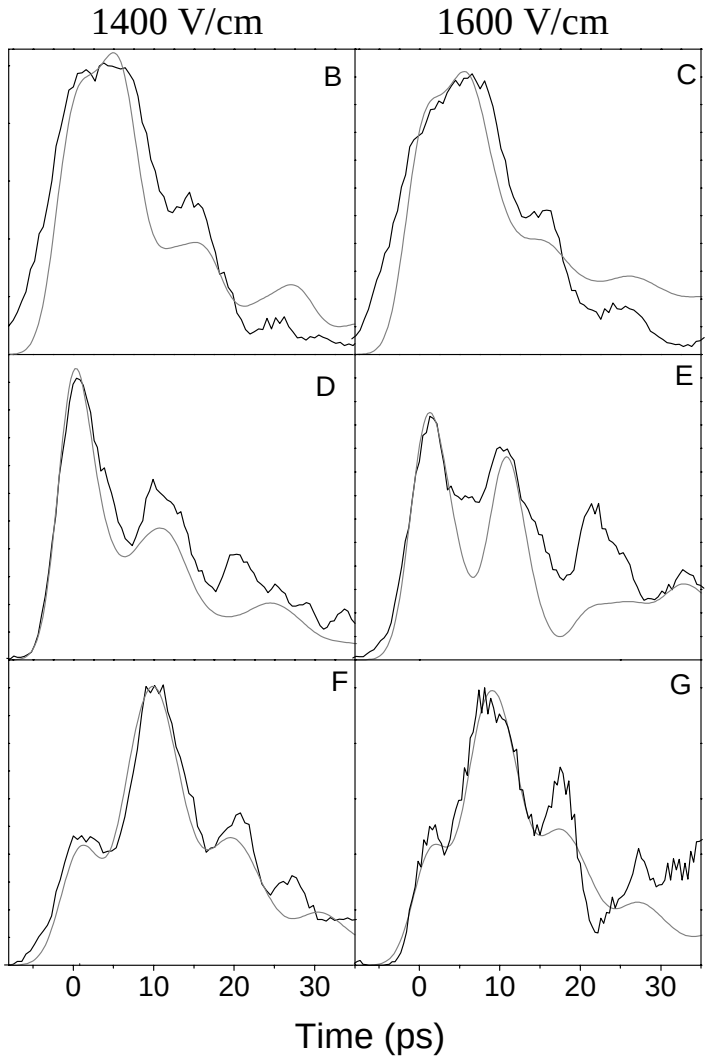

Figure 5.4: *The outgoing electron flux starting from various states in fields of 1400 and 1600 V/cm. One can see a clear difference between the flux after excitation of an initial Stark state on one hand (B,C) and starting from the 17d (D,E) and 17p (F,G) states on the other hand. The letters refer to the labels in Fig. 5.2. All show the same period which is 11 ps at 1400 V/cm and 9 ps at 1600 V/cm. The smooth lines are the calculations.*

If the initial state is the $17d$ state (Figs. 5.4D and 5.4E), the electron emission, after sudden ICE, appears dramatically different. Unlike a Stark wavepacket, which has a constant fraction of low-ℓ character, this wavepacket has, at t = 0, predominantly d character. The angular momentum starts to oscillate in the electric field up to n-1 and back. Since only the low-ℓ character can autoionize, the emitted flux exhibits recurrences separated by the oscillation period. The decay behavior is reminiscent of the decay of a one-electron autoionizing Stark wavepacket [16, 17]. The experiments and calculations agree well in the first 20 ps and start to deviate at later times.

Also starting from the $17p$-state (Figs. 5.4F and 5.4G) the electron emission after ICE does not show the stepwise decay like from an initial Stark state. The electron emission shows recurrences similar to those from an initial d-state, with the same periods. There is no intuitive reason that the second peak of electron flux should be larger than the first. Note the fact that the p-state lies right in the Stark manifold but its electron emission in time is still different from the Stark states that are only a few wavenumbers away. This indicates that the p-state indeed does not have strong Stark character.

5.4 Double wavepackets.

After a successful excitation of the isolated core electron to the first excited state, one wonders whether the isolated core electron can also be excited further to the Rydberg states converging to the doubly charged ion [86]. With a short pulse excitation we expect an angular wavepacket that periodically returns to the core and meets the previously excited, stationary Stark state. A periodic collision of the two electrons results in short shockwaves, or 'gaps' in the stationary Stark orbit. Simultaneously electrons are emitted in pulses with the combined beating period of the isolated core electron wavepacket and the stationary Stark state with shockwaves. As we have seen in this chapter the autoionization time of the doubly excited Mg atom is of the order of picoseconds. Therefore an cascaded excitation of the isolated core electron to the Rydberg series of the doubly charged ion [87, 88] would have large losses by autoionization of the intermediate resonances and is experimentally difficult. A cascaded excitation scheme of the isolated core electron can also lead to a high angular momentum state of the electron, resulting in a 'planetary atom' [89–92] where the two electrons have little interaction. A solution is a one-photon excitation of the isolated core electron with an XUV photon.

An experiment is undertaken with a similar experimental set-up as described above but where the 3s→3p excitation is replaced by excitation with tunable high order harmonics of a frequency-doubled infrared pulse as will be described in chapter 7 and 8. The 5th harmonic of a laser pulse centered around 413 nm excites the isolated core electron just below the doubly charged ionic state. An alternative method would be using the 9th harmonic of an 800 nm pulse to excite the 7p doublet state of the Mg ion. To avoid the ionization signal of ground state Mg with the XUV light, the 413

nm laser pulse was chosen to be with a perpendicular polarization as compared to the electric field. Directly ionized electrons have a large kinetic energy and will miss the detection slit of the streak camera.

Unfortunately no overlap signal was detected. We estimate the number of excited Rydberg states about 10^5. The photoionization cross section of the singly charged ion to just below the doubly charged ion is about 0.2 Mbarn [93]. Hence, we need, in our interaction region of 1 mm^2 by 10 mm about 5 10^{10} XUV photons to populate one doubly excited state. If the angular distribution of autoionized electrons is isotropic, about 10% will pass the detection slit. To obtain signal we need to generate 5 10^{11} XUV photons. This large number of photons is not generated by the 2 mJ of 400 nm light ($\sim 10^{16}$ photons), so the efficiency of the 5th order harmonic of 400 nm is less than 10^{-5}. The 9th harmonic of 10 mJ of 800 nm light does not generate that large number of XUV photons either. A more efficient way of generating high order harmonics or refocusing the available XUV light is required to make this experiment successful.

5.5 Conclusion.

We have performed sudden Isolated Core Excitation of highly excited Rydberg Stark states and observed a stepwise electron emission. The time dependent electron flux from an initial Stark state after ICE is qualitatively different than from an initial low-ℓ state, like a p or d state. A Stark state has, after sudden ICE, a constant low-ℓ fraction giving a constant autoionization rate during one angular oscillation period followed by a drop in outgoing electron flux. The electron emission shows a stepwise decay. A low-ℓ state has predominantly low-ℓ character after ICE and oscillates between high and low angular momentum, resulting in recurrences of electron emission separated by the angular oscillation time.

In the following chapter isolated core excitation is performed with a narrowband laser, scanning in the frequency domain, to spectroscopically identify the doubly excited states that are involved in the autoionization process of the Rydberg electron.

Chapter 6

Isolated core excitation detected in the frequency domain.

Electron yield spectra of doubly excited magnesium atoms in electric fields in the region 50-1600 V/cm are reported. One electron is excited to a stationary Rydberg state around n = 16, either a non-mixing state with low angular momentum or a Stark state. Subsequently the second, isolated, core electron is excited with a narrowband ns laser pulse. The isolated core excitation induces a shake-up which is measured as a function of excitation frequency. An initial low-angular momentum state leads to a much broader shake-up than an initial Stark state, i.e. many more autoionization peaks are observed for an initial low-angular momentum state than for an initial Stark state. Full quantum calculations show excellent agreement with the recorded spectra. We discuss the implications of this experiment for dielectronic recombination and compare the frequency spectra to the time dependent measurements on magnesium presented in chapter 5.

6.1 Introduction.

Isolated Core Excitation (ICE) of two-electron atoms is an established method to create autoionizing Rydberg states where the core electron is used to provide the exit energy to the Rydberg electron [1, 79]. Experiments are reported for ICE on magnesium [84,94–96] and other two-electron atoms [97–99]. In a two-electron system one electron is optically excited to a high Rydberg state. Such an electron can be viewed as a spectator, because of its large spatial extend and, consequently, small electron density in the vicinity of the ionic core. A second laser pulse excites the remaining, isolated, core electron. If the two excited electrons collide, energy exchange can take place causing one electron to decay back to its ground state whereas the other has now gained enough energy to escape the ionic core. When the isolated core electron is not excited by a laser frequency on a resonance of the ion, the spectating Rydberg electron can

sometimes absorb or donate the energy difference. Population of off-resonant Rydberg states is called shake-up.

In most cases ICE was studied in field-free conditions. If a static electric field is applied the core electron state is unlikely to be affected, owing to its small spatial size. The highly excited Rydberg state, on the other hand, will split up into Stark states. Consequently the shake-up upon ICE in a field will attain completely different states as compared with zero-field. Also the shake-up width may be changed: A Stark state is a mixture of all angular momenta, resulting in an even smaller electron density in the vicinity of the ionic core. One expects that the interaction between the two electrons decreases as compared to zero-field. Consequently the shake-up width upon ICE for a Stark state is expected to be smaller than for a low angular momentum state.

Following the development of a theoretical approach of Ref. [100], we perform a rigorous check with experimental data of magnesium. The initial and final states are populated as a function of excitation frequency with narrowband nanosecond laser pulses to determine the shake-up in various electric field strengths and starting from various states. To our knowledge this is the first match between experiment and theory of ICE spectra in a strong electric field as will be shown in sections 6.4 and 6.5.

One of the motivations to study the autoionization in a two-electron system is the relation with its time inverse process, dielectronic recombination (DR) [103–106]. DR is the process in which a free electron collides with an ion and is converted to a doubly excited atom. If one of the two excited electrons decays by sending out a photon, the initially free electron is recombined. Dielectronic recombination is playing a role in astrophysical plasmas. In such plasmas an electric field can generally not be neglected [103]. A spectating ion already exerts a field of 1400 V/cm on another ion at a distance of 100 nm. Measurements of DR are cumbersome and detecting DR as a function of field is a true experimental challenge. With relative ease the autoionization of a two-electron atom is studied. In section 6.6 we dwell upon the information for DR retrieved from ICE autoionization experiments. We find that the total autoionization cross section is identical to the DR cross section. An autoionization measurement allows us to study the partial cross sections with high resolution; we detect the autoionization yield for each principle quantum number n instead over an integrated number of n's, and we find via which final states they decay.

Finally in section 6.7 we compare the Fourier-transform of the frequency spectra with time resolved electron emission of magnesium of the last chapter. The comparison shows the differences of the recurrence of electron density back to the core and the fraction of that density that is emitted on picosecond time scale.

6.2 ICE in magnesium.

In Fig. 6.1 the laser excitation scheme is depicted of the magnesium ICE experiment in an electric field. The initial Rydberg state is prepared by exciting the $3s^2$ ground state to a Stark state $3snk$ where typically $n = 16$. Since the second electron remains in

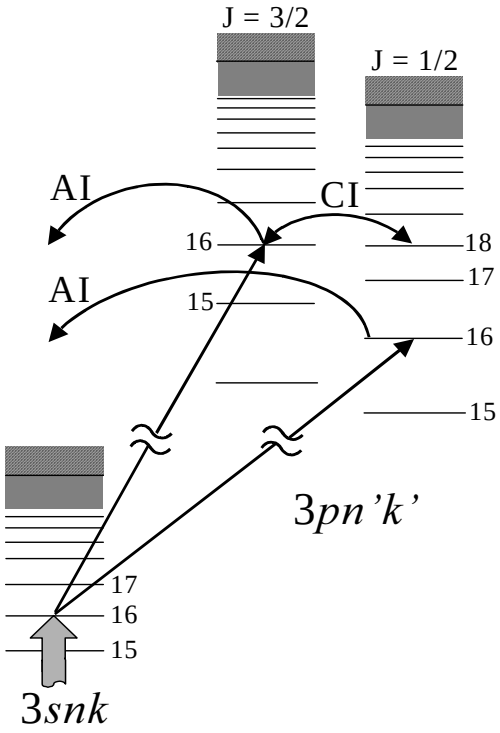

Figure 6.1: *Excitation scheme for isolated core excitation in magnesium in an electric field. One electron is optically excited to an initial 3snk, n = 16 Rydberg state. Subsequently a second laser pulse drives the isolated core electron 3s→3p ($\Delta E \backsim 4.3eV$). For clarity only one state is drawn per manifold and the spread of the Stark manifold is not shown. There are two final spin states $p_{1/2}$ and $p_{3/2}$ coupled by configuration interaction (CI). Both the $p_{1/2}$ and $p_{3/2}$ channels are coupled to the 3s continuum: Autoionization (AI) occurs when one electron decays to the 3s ground state donating its energy to the second electron which escapes the ionic core.*

the $3s$ state, we will refer to these initial states 3snk as the $3s$ channel. Subsequently the second electron is excited $3s \rightarrow 3p$. There are two final $3pn'k'$ channels, namely the $3p_{1/2}$ and the $3p_{3/2}$ channel, respectively 35669.42 and 35760.97 cm^{-1} higher in energy than the $3s$ channel [4]. Upon ICE, the initial $3snk$ state is projected onto the states in the $3p_{1/2}$ or $3p_{3/2}$ channels. Autoionization (AI) then occurs via coupling to the continuum of the $3s$ channel: One electron decays back to the $3s$ ground state donating its energy to the other electron which escapes with $\sim$4.3 eV of excess kinetic energy. If the excitation laser is detuned from the $3s \rightarrow 3p$ resonance, the inner electron can still be excited if the Rydberg electron donates or absorbs the energy difference.

Since the two final channels are only separated 91.55 cm^{-1} in energy, their Rydberg series are interleaved and can experience a strong configuration interaction (CI). For example, as one can see from Fig. 6.1, the $n = 16$ manifold of the $3p_{3/2}$ channel is

nearly degenerate with the $n = 18$ manifold of the $3p_{1/2}$ channel. On the other hand the $n = 16$ of the $3p_{1/2}$ channel has its energy in the middle between the $n = 14$ and $n = 15$ manifolds of the $3p_{3/2}$ channel. In the latter case configuration interaction could only occur between the extreme red and blue states at the highest field we used, 1600 V/cm. The Δn spacing in this energy region is around 50 cm^{-1}.

6.3 Experimental set-up.

A resistively heated oven produces an effusive beam of magnesium atoms passing through two parallel metal plates with a static electric field. The distance between the plates is 10.0 mm. The Mg is excited with two narrowband laser pulses of about 7 ns (FWHM) with a time delay of 20 ns. For the first laser pulse a Nd:YAG laser pumps a Quantel dye laser producing laser light around 648 nm. The light is frequency doubled with a KDP crystal and drives a two-photon excitation of the Mg ground state to a selected Rydberg Stark state $3s16k$ with a energy of 200 μJ focussed down to an intensity of about 10^9 W/cm^2. For the second laser pulse another Nd:YAG laser pumps a Lambda Physics Scanmate dye laser producing laser light around 580 nm. This light is also frequency doubled and drives the one photon $3s$-$3p$ isolated core transition with an intensity of only 10^3 W/cm^2. The bandwidth of both dye lasers is 0.3 cm^{-1} which is sufficient to resolve Stark structure in the used fields. The laser polarization is parallel to the electric field. The autoionized electrons pass through a mesh in one of the metal plates and is detected by a set of microspheroid plates and an anode. The electron emission is monitored as a function of energy of the ICE laser pulse and as a function of field strength between the two metal plates.

6.4 Results.

We first present the spectroscopy of the initial states $3snk$. In the last chapter, displayed in Fig. 5.2a is a Stark map, calculated in the energy range around the $n = 16$ manifold in electric fields up to 1600 V/cm. There are a few states with low angular momentum ℓ and a manifold of Stark states that fans out as a function of field. The s and d states have quantum defects δ_ℓ of 1.52 and 0.60 respectively. These states are in the middle between two manifolds and hardly mix with the Stark states in the applied fields. The p state has a quantum defect of 1.05 and is near the centre of the Stark manifold. It can, however, only mix with the Stark states if it acquires some d character. Therefore the p state is still quite unaffected by the manifold in fields up to 1600 V/cm. The remaining 13 Stark states fan out approximately linearly as a function of field. We verified the positions of the initial states experimentally. Shown in Fig 5.2b is the 2+1 photon resonant ionization yield spectrum as a function of binding energy as detected in a field of 1600 V/cm.

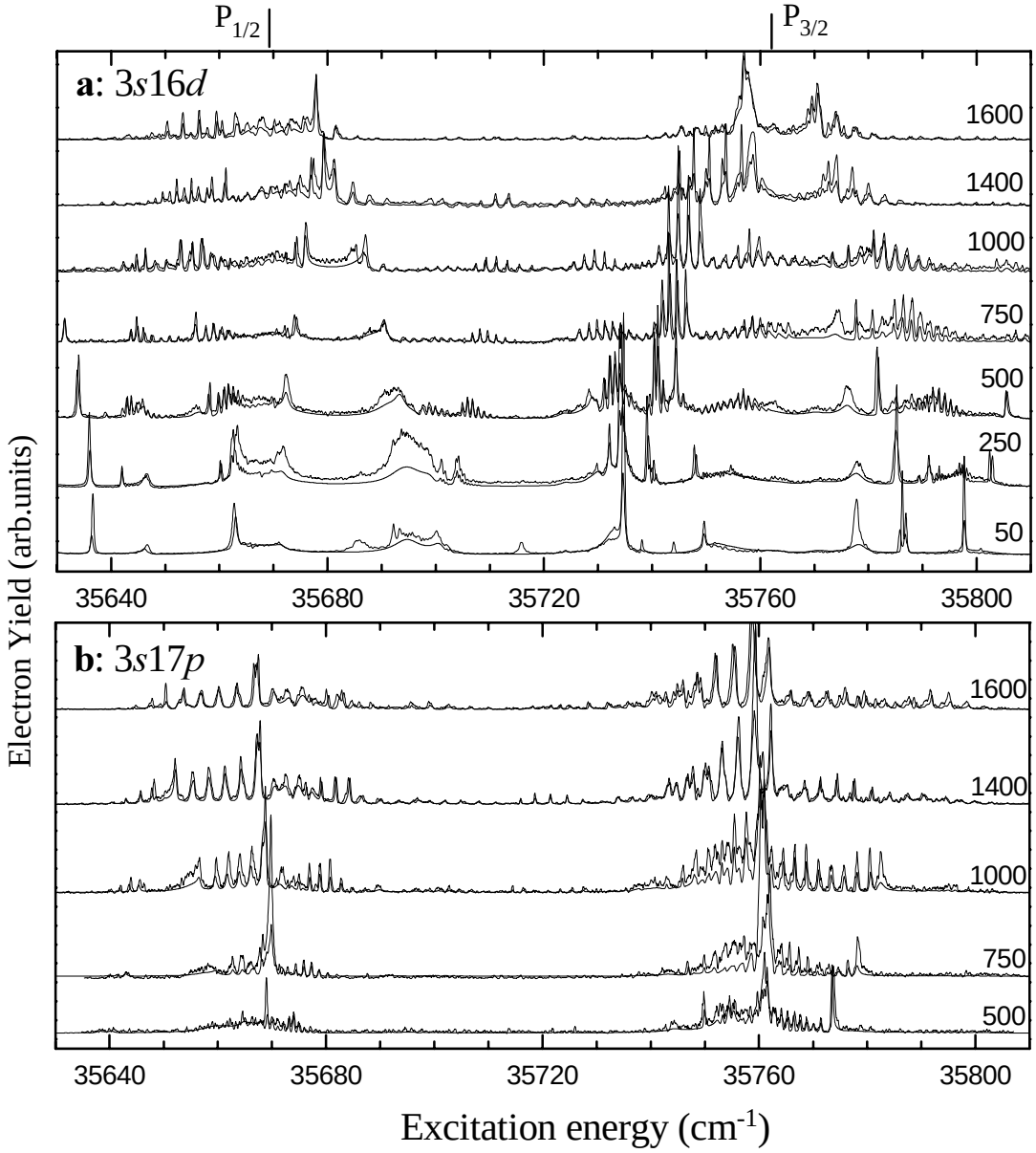

Figure 6.2: *a) Electron yield as a function of isolated core excitation energy starting with the 3s16d state in fields of 50 up to 1600 V/cm. The positions of the $3s \rightarrow 3p_{1/2}$ transition at 35669.42 cm^{-1} and the $3s \rightarrow 3p_{3/2}$ transition at 35760.97 cm^{-1} are indicated. The smooth lines are the theoretical calculations. b) Same as for a) with the initial state 3s17p in fields of 500 up to 1600 V/cm.*

Since the photoionization probability is only appreciable for low-ℓ character [13, 108] the 2 + 1 photoionization yield spectrum emphasizes the s, p and d states that are an order of magnitude stronger than the Stark states and off scale in the plot. The dotted line in Fig. 5.2b is the calculated 2-photon absorption cross section. The positions of the peaks are accurately reproduced and gives us confidence that, concerning the energy positions of the initial states, the theory matches the experiment. The Stark states are labeled according to their excitation energy from 3 up to 15. The dots in Fig 5.2a are the selected initial states from where we perform the isolated core excitation.

We first show the results of the initial low-ℓ states which are not much affected by the electric field. For the recorded spectra shown in Fig. 6.2a, the $3s16d$ state was selected as initial state. In zero-field this state has by far the largest oscillator strength in our two-photon excitation scheme. The autoionization yield after ICE is depicted as a function of excitation frequency of the isolated core electron for various fields. In a field of 50 V/cm, which is nearly field free, we observe a variety of sharp and broad features. The energy range covers a few n states, about n = 16-18 of the $3p_{1/2}$ channel and n = 15-16 of the $3p_{3/2}$ channel. Outside this region no signal is observed. As noted by Dai *et al.* [94] the broad features can be attributed to specific $3p_{1/2}nd$ or $3p_{3/2}nd$ J = 3 states. The sharp peaks are mixtures of $3p_{1/2}nd$ or $3p_{3/2}nd$ J = 1 states. The shake-up starting from $3s16d$ is so large that the autoionization peaks belonging to both spin channels are interleaved and spread over the whole energy range of Fig 6.2a.

Once the field is increased to 500 V/cm, narrow Stark states appear and the broad features sharpen up. At about 1600 V/cm we only observe Stark states of 1 cm^{-1} width. The spacing between the states is 3.0 cm^{-1} in this field, slightly less than the spacing of the Stark states of the initial $3s$ channel. Note that the laser linewidth is 0.3 cm^{-1}. It is difficult to determine a number for shake-up width from these spectra. To qualitatively get a feeling for the shake-up width we assume that the autoionizing states detected after ICE are in fact two groups of states centered around the $3s \rightarrow 3p_{1/2}$ and the $3s \rightarrow 3p_{3/2}$ transition. The two groups are observed over a certain energy range. Fig. 6.2a shows that the shake-up after ICE of an initial d-state is rather large; the width is about 100 cm^{-1} at 50 V/cm down to about 50 cm^{-1} in 1600 V/cm for each spin-orbit channel.

In Fig. 6.2b the autoionization yield of an initial $3s17p$ after ICE is depicted as a function of excitation frequency state for various fields. The initial $3s17p$ state can only be excited in a field of at least 500 V/cm with a two-photon excitation scheme. The ICE spectrum only consists of sharp Stark states without any broad features. The width of the Stark states is 1 cm^{-1} and the spacing in a field of 1600 V/cm is also 3 cm^{-1}. In all fields the shake-up width is about 50 cm^{-1}. In the ICE spectra of initial low-ℓ states in high fields there are no peaks with a large cross section that would indicate a predominant low-ℓ character. In the $3p$ channel all states are mixed above 500 V/cm, in striking contrast to the $3s$ channel where we can clearly distinguish the low-ℓ states in all fields.

In order to compare the shake-up starting from various initial states, Fig. 6.3

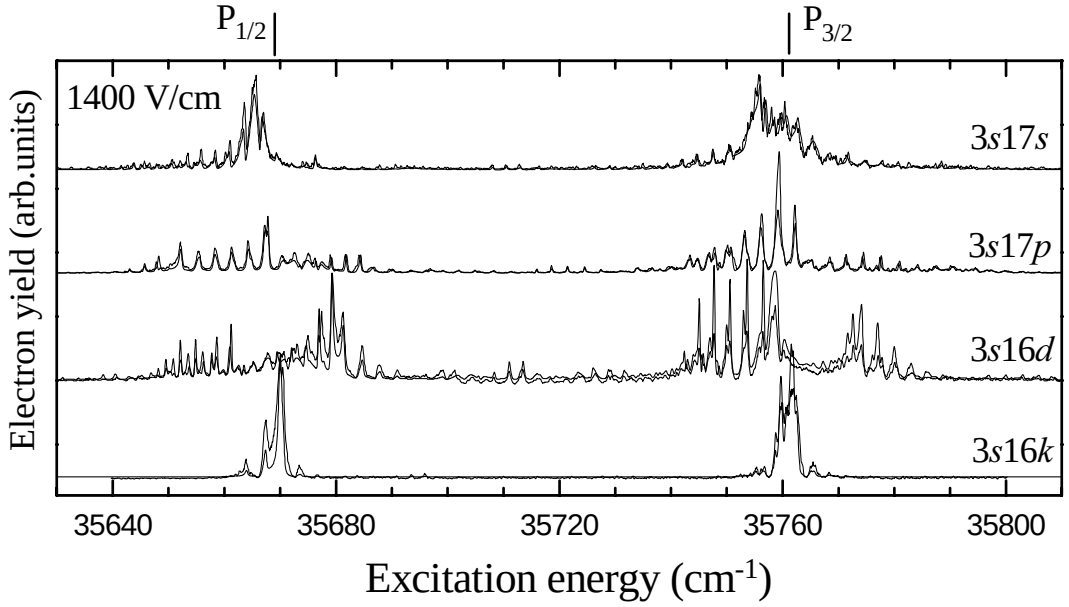

Figure 6.3: *Electron yield as a function of isolated core excitation energy starting with the initial state (top to bottom) the 3s17s, 3s17p, 3s16d low-angular momentum states and the 3s16k Stark state with $k = 4$ as labeled in Fig. 5.2. The electric field is 1400 V/cm. The energy scale is identical to that used in Fig 6.2. The positions of the $3s \rightarrow 3p_{1/2}$ transition at 35669.42 cm^{-1} and the $3s \rightarrow 3p_{3/2}$ transition at 35760.97 cm^{-1} are indicated. The smooth lines are the theoretical calculations.*

shows the autoionization yield as a function of excitation frequency of the isolated core electron in a field of 1400 V/cm. The top three curves are spectra taken with $3s17s$, $3s17p$ and $3s16d$ as initial state. All states with low angular momentum in a strong electric field have a shake-up with a width of about 50 cm^{-1}. The richness of the ICE spectrum is dramatically less if we start from a Stark state. The bottom curve in Fig. 6.3 shows the ICE spectrum starting from an initial $3s16k$ Stark state, with $k = 4$. The shake-up only has a width of about 5 cm^{-1}. We have taken spectra at several initial Stark states and observe that all have a similar small shake-up width. In Fig. 6.4 we show the ICE spectra starting from various initial Stark states and zoom in on the energy axis. In the $P_{1/2}$ channel there is one large peak and, in case of an initial red Stark state (k = 3-8) a smaller peak on the low-energy side and in case of an initial blue Stark state (k = 10–15) a smaller peak on the high energy side. The small and large peak are juxtaposed around the central $3s \rightarrow 3p_{1/2}$ transition at 35669.42 cm^{-1}. The energy difference between the peaks matches the Stark spacing of 3 cm^{-1}, the width of the peaks is 1 cm^{-1}. In the $P_{3/2}$ channel, on the other hand, we observe more states, up to twice as many as in the $P_{1/2}$ channel depending on the initial Stark state. All peaks are centered around the $3s \rightarrow 3p_{3/2}$ transition at 35760.97 cm^{-1} also with a

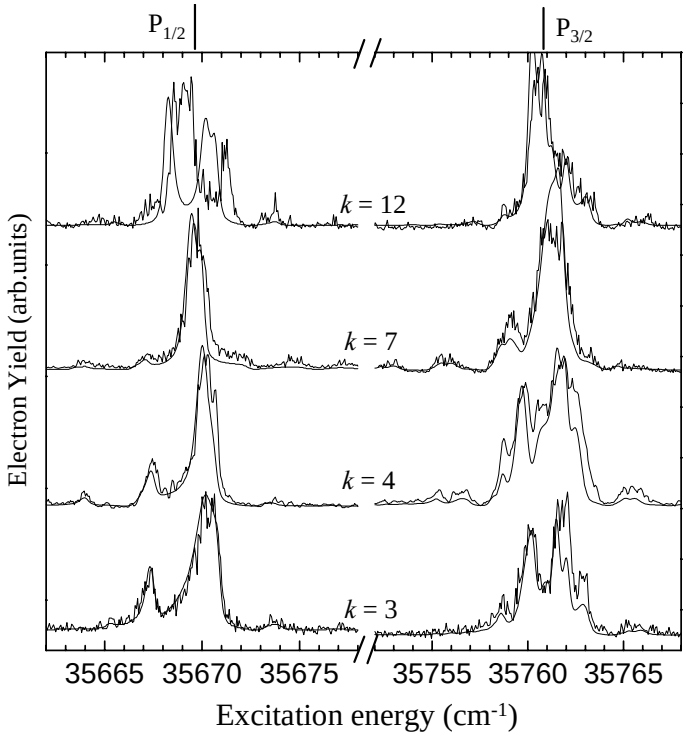

Figure 6.4: *A blow-up of the energy scale centered around the 3s→3p$_{1/2}$ transition at 35669.42 cm^{-1} and the 3s→3p$_{3/2}$ transition at 35760.97 cm^{-1} of the electron yield as a function of isolated core excitation energy starting with the 3s16k Stark states with k = 3, 4, 7 and 12 as labeled in Fig. 5.2. The smooth lines are the theoretical calculations.*

shake-up width of 5 cm^{-1}.

The smooth lines in Fig. 6.2-6.4 are the MQDT calculations developed in [100]. As one can see, the agreement is nearly perfect. To our knowledge this is the first theoretical match on isolated core excitation in a static electric field. Agreement is equally good over the entire range of electric fields and starting from all initial states. We can see in Fig. 6.2a that there is a small deviation between the experimental and theoretical curves at low fields. Saturation effects probably caused the relative increase of broad peaks in the experimental data.

6.5 Discussion.

Energy exchange between the two excited electrons upon ICE can only occur in the core region. In the absence of a field the Rydberg electron spends only a fraction of it radial oscillation time ($\tau_n = 2\pi n^3$, 0.6 ps for $n = 16$ [78]) in the vicinity of the core and is viewed as a spectator. This restricts the probability of transition to the final $3p$

states to a certain shake-up width. This shake-up width of $n = 16$ is about 100 cm^{-1} for an initial low-ℓ state in field-free conditions as seen in Fig. 6.2a. Upon introduction of a static electric field the angular momentum of the initial Rydberg electron is no longer conserved and the degenerate Rydberg state splits up into Stark states. Starting from a pure Stark state we observe a shake-up width of only 5 cm^{-1}. Thus we can view an electron in an initial Stark state even more as a spectator than an electron in an initial low-ℓ state. The difference in shake-up width is due to the additional angular oscillation of the Stark electron.

It may recur radially every 0.6 ps, however, most of the time the Stark electron will be in high (ℓ>3) angular momentum, describing a more circular orbit, far from the core region. The angular oscillation period at 1600 V/cm is about 10 ps. The initial $3s$ low-ℓ states are slightly mixed with Stark character at 1600 V/cm and the shake-up width decreases from 100 cm^{-1} in zero-field to 50 cm^{-1} in 1600 V/cm.

The difference in shake-up width can be understood in the angular momentum picture: ICE of an initial Stark state only affects the low angular momentum fraction. The higher angular momentum fraction, with ℓ>3, has a quantum defect of approximately zero before and after the ICE. In other words, most of the Stark state is not changed by the excitation of the core and the shake-up can only be small. The smallest shake-up possible would lead to only one peak per spin channel in the autoionization spectra. The notion that the dipole moment k of the Stark states hardly changes in an optical excitation has also been observed in far-infrared ionization of Rydberg-Stark atoms [16, 102]. For an initial magnesium Stark state the change in dipole moment is small but not strictly zero. Note that there are only 13 initial Stark states $3snk$ and 16 final Stark states $3pn'k'$. At 1600 V/cm the 13 initial Stark states are spread over more or less the same energy region as the final 16 Stark states. Therefore the spacing between the initial states is larger (3.4 cm^{-1}) than for the final states (3.0 cm^{-1}). Upon ICE the reddest initial Stark state $k = 3$ (k is just a label here, see Fig. 5.2a) is projected onto (in hydrogenic labeling) the k' = -13 and k' = -15 states. The k = 4 state is projected onto k' = -13 and k' = - 11, and so on. This is well observed for the $P_{1/2}$ spin-channel as shown in Fig. 6.4.

For the $P_{3/2}$ channel the autoionization spectra are more complicated. The differences between the $P_{1/2}$ and the $P_{3/2}$ channel as seen in Fig. 6.4 is caused by configuration interaction. The k' = -15 and k' = - 13 of the $n = 16$ manifold of the $P_{3/2}$ channel are interleaved with the k' = -11 and k' = -9 of the $n = 18$ manifold of the $P_{1/2}$ channel. All these four states are localized on the same, down potential side of the atom in a field, making configuration interaction favorable. Also $P_{3/2}$ $n = 14$ blue states are degenerate with the reddest $P_{1/2}$ $n = 16$ states, but since the blue states are localized on the uphill side of the potential, no configuration interaction is observed for $P_{1/2}$. Configuration interaction make it very hard to theoretically fit all details of Fig. 6.4. The $P_{1/2}$ channel gives a far better fit that the $P_{3/2}$ channel. The observed width in Fig. 6.4 of the final Stark states is 1 cm^{-1} corresponding to a lifetime of 15 ps. That indicates that the probability of the Stark states to autoionize upon core passage is high: the electron density has autoionized within about two angular recurrences.

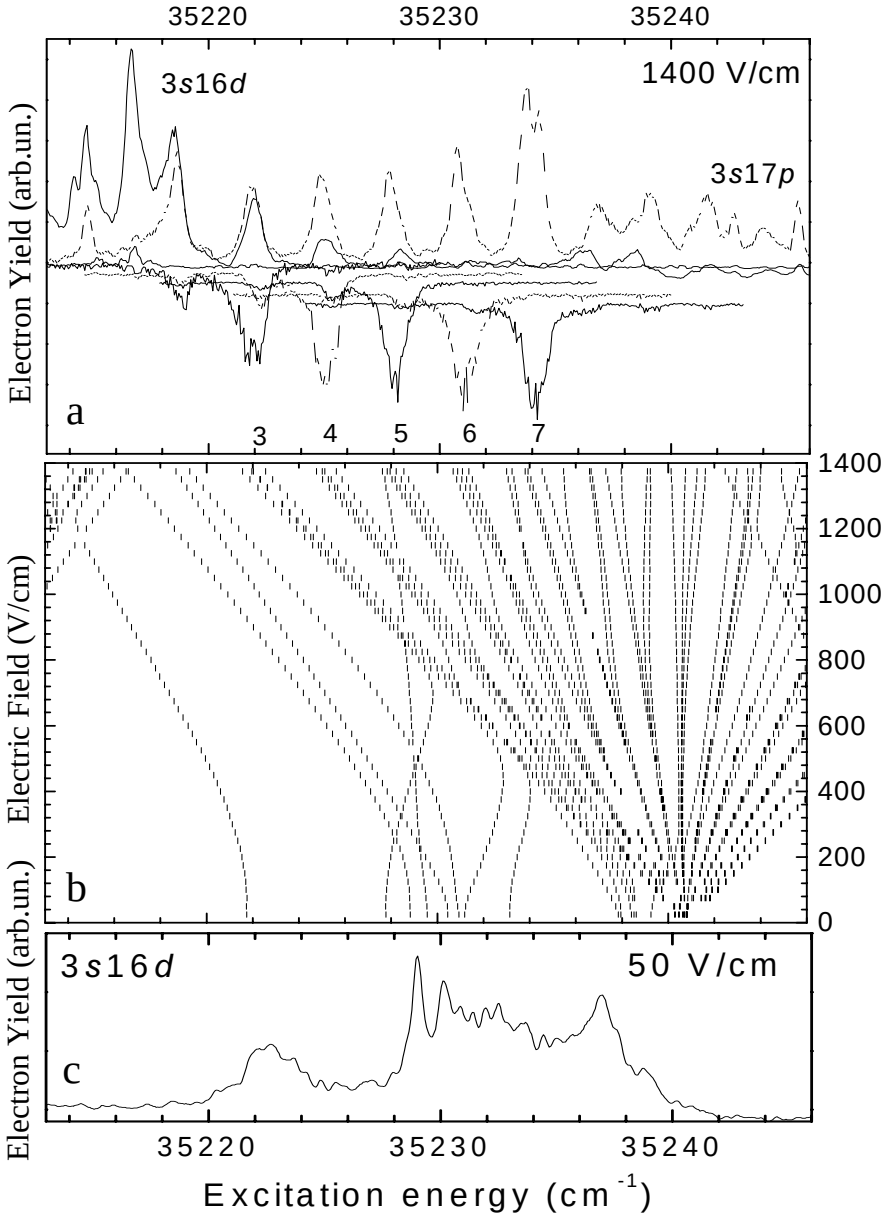

Figure 6.5: *a) Electron yield as a function of isolated core excitation energy minus the initial binding energy. Initial states are 3s16d (solid), 3s17p (dotted) and the five reddest Stark states (3-7; upside down). b) Simulation of the energy of the 3p channel states as a function of electric field. c) Electron yield as a function of isolated core excitation energy minus the initial binding energy for an the initial states 3s16d at 50 V/cm.*

As we have seen in [100], the only difference between the various initial states is their overlap integral with the $3p$ channels and their initial binding energy (Eq. 10 of [100]). They autoionize essentially via the same $3p$ states. In Fig. 6.5a we plotted the ICE electron yield spectra of various initial states as a function of isolated core excitation frequency minus the initial binding energy of the states in a field of 1400 V/cm. In other words, the ICE spectra are plotted as a function of energy above the $3s$ channel ionization limit. For clarity only a small energy region around the $P_{1/2}$ transition is shown. The solid line is the ICE spectrum starting from the $3s16d$ state, the dotted line starting from the $3s17p$ state. The ICE spectra starting from the reddest five Stark states are plotted up side down. It is clear the same $3p$ states are seen starting from different initial states. The only difference in the spectra is the overlap. In Fig. 6.5b a theoretical spectrum is shown of the energy of the $3p$ autoionizing states as a function of field strength (like Fig. 5.2a for the $3s$ states). All m-states are shown. In our experiment both excitation lasers were parallel with the electric field and only $m = 0$ states can be reached. For comparison, at low-field the ICE spectrum starting from the $3s16d$ state in 50 V/cm is shown in Fig 6.5c. Starting from zero-field the $n = 16$ Stark manifold fans out around 35241 cm^{-1}. In these low fields, however, only the states with d-character can be reached and we observe broad features around 35222 and 35232 cm^{-1}. Upon increasing the field the d states are mixed into the Stark manifold and at 500 V/cm the Stark states have acquired enough d-character to show up in the ICE spectra (compare Fig. 6.2). Finally, at 1600 V/cm all low-ℓ states are mixed into the Stark manifold that we observe in Fig. 6.5a.

6.6 Implications for dielectronic recombination.

Let us divide the autoionization experiment into three parts: Excitation from the Mg ground state to the initial Rydberg states in the $3s$ channel, the radiative excitation (the ICE) to the $3p$ channel, and electron emission. Dielectronic recombination (DR) is the time inverse process: capture of a free electron by excitation of a Mg ion into a doubly excited neutral, radiative decay to a singly excited state and radiative decay to the Mg ground state. The second step of both processes involve the same couplings between states. What can we learn from an autoionization experiment that is important for DR?

The DR rate is proportional to $\Gamma_{a,\rho}\Gamma_{R,\rho}/(\Gamma_{a,\rho}+\Gamma_{R,\rho})$ (i.e. proportional to the rate of capture $\Gamma_{a,\rho}$ into the autoionizing states ρ times the branching ratio for photon emission $\Gamma_{R,\rho}$) [105]. Each autoionizing state ρ with a rate of capture $\Gamma_{a,\rho}$ larger than the photoemission rate $\Gamma_{R,\rho}$ contributes to DR. An electric field enhances DR [103] since it mixes the short-lived low-angular momentum states with long-lived high-angular momentum states. Effectively this increases the number of states that have a faster autoionization rate than the radiative rate. For the time-inverse process of DR, our autoionization measurement, the same rates are important. In the first excitation step we can choose which initial $3s$ state to probe, provided it has oscillator strength from

the ground state. In the second step the strength of the coupling between the $3s$ and $3p$ channels leads to a shake-up width for autoionization or a radiative decay $\Gamma_{R,\rho}$ for DR. If electron emission (third step) of a populated state in the $3p$ channel is observed, it implies that its autoionization rate $\Gamma_{a,\rho}$ is larger than its radiative rate $\Gamma_{R,\rho}$ back to the $3s$ channel. In other words, what we detect is proportional to the radiative rate $\Gamma_{R,\rho}$ into the autoionizing states ρ times the branching ratio for autoionization $\Gamma_{a,\rho}$, so together $\Gamma_{R,\rho}\Gamma_{a,\rho}/(\Gamma_{a,\rho}+\Gamma_{R,\rho})$, where $\Gamma_{a,\rho} > \Gamma_{R,\rho}$. This is equal to the DR rate into the selected Rydberg state.

Measuring the autoionization yield of an initial $3s$ state is identical to detecting the partial DR cross section for that state. Integration of the autoionization yield of all initial $3s$ states results in the total DR cross section. The advantage of an autoionization measurement is that we gain information about both the initial and final states in the second step with high resolution (equal to the laser bandwidth). Knowledge of the coupling between initial and final states can be important to explain e.g. the enhancement of the DR cross section, owing to an electric or magnetic field.

6.7 Time-dependent ICE.

In the above described experiment the isolated core was excited with a ns, narrowband laser pulse. If the excitation is done with a short pulse, with a bandwidth larger than the spacing between the shake-up states, a coherent superposition of the final $3p$ states is created. Short pulse ICE is investigated in field free conditions [81, 95, 98, 99, 101]. In the previous chapter, we reported short pulse ICE in an electric field.

In Fig. 6.6 the initial states are a $3s16k$ Stark state with $k = 4$ as labeled in Fig. 5.2a, and the low-ℓ states $3s16d$ and $3s17p$, in a field of 1400 V/cm. Shown is (solid lines) the electron emission as a function of time after sudden isolated core excitation with a laser pulse of 2 ps, copied form Fig. 5.4. The dashed lines are the simulations of the electron emission in time, based on the MQDT theory developed Ref. [100]. Slight deviations can be attributed to the high excess kinetic energy ($\sim$4.3 eV) of the autoionized electrons. It is clear that the ICE spectra of Mg in an electric field can be accurately simulated both in frequency and time.

The electron emission is the flux of electron density that escapes over the saddle-point. We would like to compare this flux with the electron density at the core. Fourier transforming the frequency spectra provides us with that information. The detected frequency spectra from Fig. 6.3 are multiplied by a Gaussian with the bandwidth of 7 cm^{-1} (corresponding to the 2 ps pulse) and Fourier-transformed. The resulting curves (dotted lines in Fig. 6.6) give the recurrence probability of the initial excitation conditions [16, 102]. For an initial low-ℓ state this means the recurrence to that low-ℓ in the vicinity of the ionic core. At t = 0 the probability is normalized, whereafter the probability shows a periodic, oscillatory behavior. At the moment of recurrence there is a probability for electron emission. As one can indeed see, the periodicity in Figs. 6.6b and c for electron emission and recurrence are identical. The intensity is not

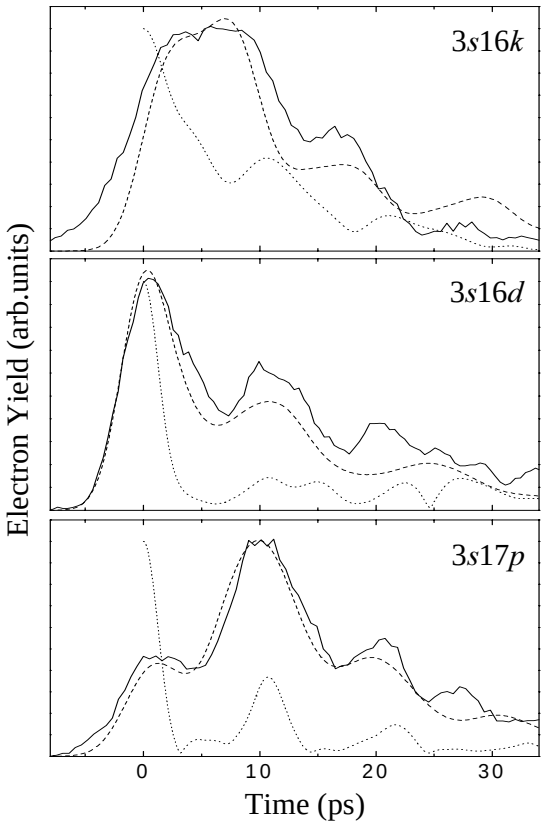

Figure 6.6: *The electron emission in time upon ICE starting from a) the 3snk, $k = 4$ Stark state, b) the 3s16d state and c) the 3s17p state in a field of 1400 V/cm. The solid line is the streak camera measurement, the dashed line is the calculation of the electron emission. For comparison also the Fourier-transform of the corresponding frequency spectrum multiplied by the bandwidth of the laser is displayed (dotted line), corresponding to the electron density at the core.*

necessarily the same. For example, the electron density at the core right after sudden ICE of an initial $3s17p$ state is high (Fig. 6.6c). This does, however, not result in strong electron emission. Most emission occurs at the first electron recurrence to the core after one angular oscillation.

For an initial Stark state the electron emission after sudden ICE and the Fourier-transformed ICE frequency spectrum are distinctly different (Fig. 6.6a): Fourier-transforming the frequency spectrum actually provides us with the recurrence of the shock wave-front rather than the electron density at the core. At the moment of sudden ICE the shock wave starts close to the core. Simultaneously the constant electron emission begins. After one angular oscillation period (10 ps) the shock wave returns to the core and suddenly the electron emission drops. This happens a second time at 21 ps.

6.8 Conclusion.

We performed isolated core excitation of magnesium atoms in an electric field and monitored the autoionization yield as a function of isolated core excitation frequency. We started with different initial states in various electric fields. The various initial states around $n = 16$ lead to very different shake-up widths upon ICE: An initial low-ℓ state has a much larger shake-up width (100-50 cm^{-1}) than an initial Stark state (5 cm^{-1}). All spectra can be accurately fitted with the MQDT theory, for all fields, both in frequency and time. Comparing the autoionization measurements with dielectronic recombination measurements, we find that these measurements are in essence the same. Detecting autoionization, however, has the advantage that it is much easier and it displays a high resolution to discern the states that are involved. Finally, we compared the Fourier-transform of the frequency spectra with time-dependent electron emission measurements of ICE of the previous chapter. For initial low-ℓ states the same periodic behavior is observed, for an initial Stark state, however, the electron emission is stepwise and the FT of the frequency spectrum provides us with the recurrence spectrum of the excitation shock-wave. If the shock-wave returns to the core, the electron emission suddenly drops.

'Met vuur en vlam ben ik aan de arbeid; kan mijn geluk niet op, want wat is er heerlijker dan een hersenschim te verzinnelijken.'

M.C. Escher.

Part 3

Application of ionization of photoexcited Rydberg electrons.

Using the knowledge gained in the preceding chapters on the behavior of atoms under influence of a laser pulse we reverse the situation: The atom is used as a tool to monitor the laser pulse itself, both in the frequency and time domain. First the photoionization probability of neon as a function of electric field is applied in chapter 7 to retrieve the spectrum of the excitation pulse. In chapter 8 neon is used as a photocathode to convert high-energy photons into low-kinetic energy electrons. These electrons are detected as a function of time which reflects the temporal profile of the excitation pulse.

Chapter 7

Atomic spectral detection of tunable XUV pulses.

A novel method is demonstrated to detect the spectral width and wavelength of XUV pulses with the photoionization probability of an atom in an electric field. A tunable laser source in the XUV is used based on higher harmonic generation of the frequency doubled output of a 50-fs Ti-Sapphire laser. The bandwidth and the wavelength of the 7th harmonic (∼57 nm) is detected with neon, where the resolving power $\lambda/\Delta\lambda$ is 10^5.

7.1 Introduction.

In many experiments in atomic and atmospheric physics a tunable, pulsed XUV laser source and an easy pulse characterization are desirable. Excitations from ground state atoms or molecules to their ionization or dissociation threshold are typically in the 10-20 eV, XUV region. Spectral characterization of XUV radiation is far from trivial; one needs the use of gratings and a long path for the divergence of the frequency components, all in the vacuum. The typical resolving power $\lambda/\Delta\lambda = 10^4$-$10^5$ [109]. Common to all (XUV) spectrometers is that the photon is converted into a detectable particle (often an electron) and that the detector is frequency selective. As we have seen in the previous chapters the photoionization of atoms fulfills both criteria: Photoionization yields detectable electrons and the photoionization probability is sensitive to whether the photon energy is below or above the threshold.

We present a novel method to measure the spectrum of XUV pulses with a minimum of experimental tools. An atom is selected such that the photon energy of the XUV pulse is just below the zero-field ionization threshold. Upon excitation one electron populates a superposition of Rydberg states, within the bandwidth of the XUV pulse, as schematically depicted in Fig. 7.1a. An electric field creates a saddlepoint in the Coulomb potential in the opposite direction of the field. Rydberg states that

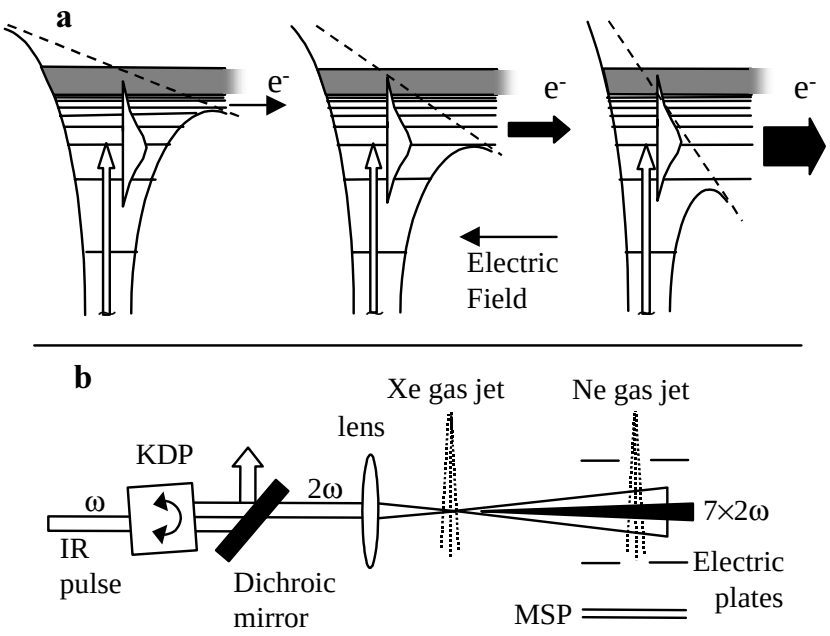

Figure 7.1: *a) Coulomb plus electric field potential of a Rydberg electron. The XUV pulse excites a superposition of Rydberg states. Fieldionization occurs only for the fraction of Rydberg states above the created saddlepoint. The field strength is increased from left to right, yielding a higher electron flux. b) Scheme of the experimental set-up. The output of a Ti-Sapphire laser is frequency doubled with a 20-mm KDP crystal. The resulting UV pulse is separated from the fundamental and focussed into a Xe gas jet with a 50 cm lens. Ne atoms in a pulsed gas jet are fieldionized between two electrically charged plates. Electrons can pass through a slit in one plate and are detected by a multichannel plate and anode.*

are energetically above this saddlepoint are fieldionized. Rydberg states that are energetically below the saddlepoint remain bound, as is well known from zero kinetic energy electron spectroscopy (ZEKE) [6]. By monitoring the photoionization yield as a function of applied electric field, the detected spectrum will be the integration of the XUV excitation above the saddlepoint. By taking the derivative of the photoionization spectrum the spectrum of the original excitation pulse is retrieved. This method can be implemented anywhere in an experiment where there is space for two electric field plates, an atomic gas jet and an electron detector.

To demonstrate our method, XUV pulses are generated using high harmonic generation: The output of a femtosecond laser system is focussed into a gas jet that emits the odd harmonics of the fundamental. The resulting harmonics, however, have a very large bandwidth, on the order of the fundamental bandwidth times $\sqrt{N}$ for the N'th harmonic [110–112], which is too large for a sensible test of the method. To generate narrowband XUV pulses one can use a picosecond dye laser as the fundamental light

for high harmonic generation [113]. We employ an alternative method to create the (relatively) narrowband fundamental light by frequency-doubling the fundamental femtosecond pulse with a long, non-linear crystal. The bandwidth of the frequency-doubled light is inversely proportional to the length of the crystal [11,114]. Additionally, by rotating the doubling crystal the phase matching angle is changed and hence the doubled output is tunable in wavelength [115,116]. An advantage of using frequency-doubled light as the driving frequency of high order harmonic generation is that only a low-order harmonic is needed to reach the XUV region, so that the generation is already efficient at a relatively low intensity.

7.2 Experimental.

The experimental set-up is schematically depicted in Fig. 7.1b. The output of a 50 fs Ti-Sapphire laser (8 mJ/pulse) is frequency doubled with a 20-mm Potassium Dihydrogen Phosphate (KDP) crystal using type I second harmonic generation. The resulting UV pulse is separated from the fundamental by a dichroic mirror and focussed into a Xe gas jet with a 50 cm lens to generate higher harmonics. A reflection of the UV is guided into a spectrometer to monitor wavelength and bandwidth. All harmonics pass through an interaction region with a pulsed neon gas jet between two electrically charged plates. Ionized photoelectrons are detected trough a slit by a microspheroid plate and anode. Only the 7th harmonic produces detectable photoelectrons: Lower harmonics do not induce photoionization and higher harmonics produce photoelectrons with high kinetic energy that do not reach the detector because the UV and its harmonics have a polarization perpendicular to the applied electric field. A few hundred XUV photons per pulse suffice for the measurement.

7.3 Frequency-doubling the infrared pulse.

In the experiment a Potassium Dihydrogen Phosphate (KDP) crystal is used, for type I second harmonic generation. For maximum conversion efficiency of the fundamental light, the crystal is tuned to the phase-matching angle θ_{pm}^{ooe}, given for a negative, uniaxial crystal by [11]:

$$\tan^2 \theta_{pm}^{ooe} = \frac{1-U}{W-1} \tag{7.1}$$

$$U = \frac{\left(2n_{o1}/\lambda_1\right)^2}{\left(n_{o2}/\lambda_2\right)^2}, \quad W = \frac{\left(2n_{o1}/\lambda_1\right)^2}{\left(n_{e2}/\lambda_2\right)^2} \tag{7.2}$$

where λ_1 is the fundamental wavelength and λ_2 is the second harmonic wavelength, with corresponding ordinary and extraordinary index of refraction n_o and n_e. At phase-matching angle the phase velocity of the fundamental and the second harmonic light

are equal. The group velocity at phase-matching angle, however, is different and the second harmonic pulse will lag behind the fundamental pulse after a short distance in the crystal [114]. The result is a square frequency-doubled pulse with a duration corresponding to the group velocity difference. The group velocity v_g is given in first order by:

$$v_g = c(n_i - \lambda \frac{\partial n_i}{\partial \lambda})^{-1} \tag{7.3}$$

At phase-matching angle, where $n_{o1} = n_2^e(\theta_{pm}^{ooe})$, the time delay caused by the group velocity difference is, in first order:

$$\frac{L}{c}(\lambda_1 \frac{\partial n_{o1}}{\partial \lambda_1} - \lambda_2 \frac{\partial n_2^e(\theta_{pm}^{ooe})}{\partial \lambda_2}) \tag{7.4}$$

where L is the length of the crystal and c is the speed of light.

At phase-matching angle, 44.9°, with the values from Ref. [67] for 800/400 nm, we obtain a time delay of 0.077 ps/mm. Since we use a KDP crystal of 20 mm, we expect, in the low intensity limit, a doubled light pulse that has a block shape in time of 1.55 ps [13, 119]. Of course it can not be a sharp block because only a limited range of frequency components are doubled by the crystal. At best the edges of the block pulse have equal rise time as the fundamental pulse.

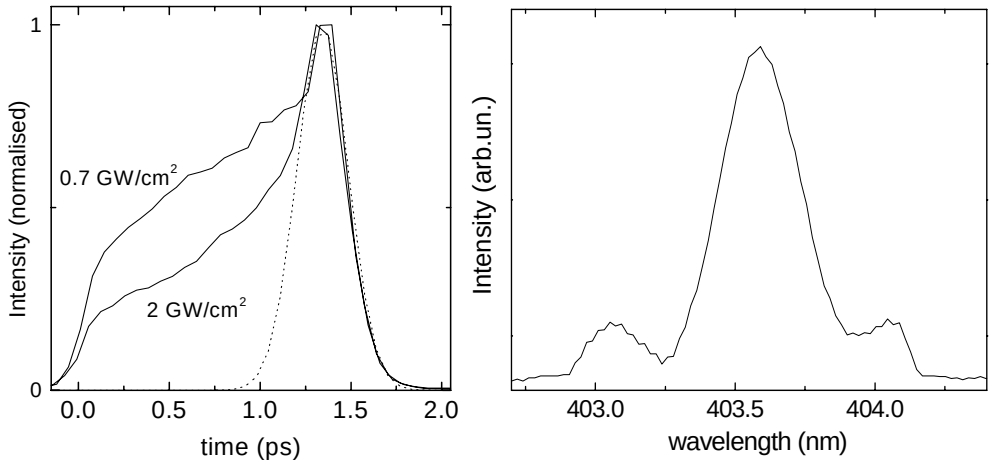

Figure 7.2: *The normalised temporal and spectral profile of the 20-mm KDP crystal frequency doubled pulse. The intensity of the fundamental (800 nm) is 0.7 and 2 GW/cm^2 for the temporal profile and 2 GW/cm^2 for the spectral profile. The crystal angle is 42.16°.*

Exceeding an intensity of about 10^7 W/cm^2 the conversion to UV becomes so efficient that it depletes the fundamental light. The UV that is generated in the first part of the crystal will have a higher intensity than that what is generated at the end

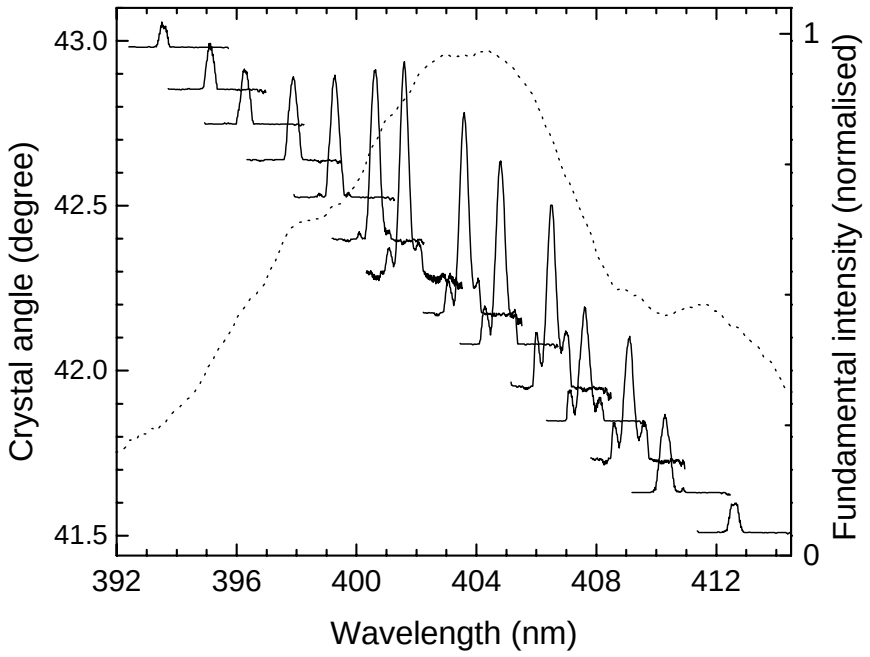

Figure 7.3: *Spectral profiles (solid lines) of the frequency doubled pulses from a 20-mm KDP crystal at various crystal angles. The fundamental IR pulse (dotted line, $I = 10\ GW/cm^2$) is shown as a function of wavelength divided by 2.*

of the crystal. In Fig. 7.2 the temporal and spectral profile is shown for a fundamental pulse with a high intensity. The temporal profile is detected by a difference-frequency measurement of the frequency-doubled pulse with its fundamental pulse, resulting in an 800 nm signal if the two pulses overlap both in space and time. The flanks have a risetime of about 0.15 ps. The profile resembles a 0.3 ps Gaussian pulse (dotted line) with a long prepulse that has relatively less power at higher fundamental intensity. The duration of the pulse is indeed about 1.5 ps.

The spectral profile shown in Fig. 7.2 is detected with a spectrometer. Owing to the high fundamental intensity, the central peak of the frequency-doubled light is saturated and one observes two side peaks appear at 0.5 nm of the central peak. The width of the central peak is 0.3 nm. To relate the temporal profile to the spectral profile; a 0.3 ps Gaussian pulse in time corresponds to a 0.73 nm Gaussian pulse in wavelength. The prepulse in time, however, modulates the spectrum. Assuming that the temporal profile consists of an infinite number of 0.3 ps pulses, with a maximum spacing of 1.1 ps, a modulation is expected with a period of 0.48 nm, which corresponds well with the observed 0.5 nm.

In Fig. 7.3 the tunability of the frequency-doubled output 20-mm KDP crystal is shown. The dotted line is the power of the IR as a function of the wavelength divided by 2. The solid lines are the spectral profiles of the frequency doubled light at various

crystal angles. The conversion efficiency is 15%. The tuning range stretches over 392-413 nm with >1 mJ/pulse [1]. The tuning range is only constrained by the bandwidth of the fundamental pulse. With the advance of few-cycle optical pulses this constraint is weakened rapidly. A full octave on bandwidth produced by a Ti-Sapphire laser system has been demonstrated [117,118], which could realize a continuous tuning range of 300 - 600 nm.

The spectral width of the frequency-doubled pulses is in the whole tuning range 0.3 nm or 3 meV. In the wings of the tuning range single peaks are observed. In the center of the tuning range the power of the IR light is high, resulting in saturation of the central peak as shown in Fig. 7.2.

7.4 Detection of XUV.

The frequency-doubled pulse is used to generate higher harmonics. The 7th harmonic in this experiment is tunable in the range 56 - 59 nm (22.1 - 21.0 eV), around the lowest Ne zero-field ionization potential at 57.494 nm (21.565 eV, [4]). To demonstrate the atomic detection of XUV pulses, the UV is tuned to 403.00 nm (3.0766 eV). The 7th harmonic (expected at 21.536 eV) populates a superposition of Rydberg-Stark states just below the Ne ionization potential ($n \simeq 20$, where n is the principle quantum number). In Fig. 7.4a the fieldionization yield as a function of the applied electric field is shown. A 10 - 90% photoionization is achieved in the range 1000 - 3000 V/cm. A simple formula for the classical saddlepoint energy, $E = IP - 2\sqrt{F}$, relates the electric field F to the energy E below the ionization threshold (IP) of the atom [1]. In order to retrieve the spectrum of the XUV pulse, the curve in Fig. 7.4a is differentiated and the result is plotted in Fig. 7.4b. The photon energy of the XUV pulse is indeed centered at 21.536 eV and the bandwidth is 15 meV. No sidewings are observed, only a slight asymmetry. For comparison the fundamental UV pulse is plotted (dotted line) with the energy scale multiplied by 7. It is somewhat surprising that the width of the XUV pulse equals 7 times the width of the central peak of the fundamental pulse. It is clear that the spectral profile of the 7th harmonic is not well predicted by convoluting the fundamental profile seven times with itself. For a more detailed interpretation of the width of the harmonic one needs a true model of an atom in a driving laser field, including the side-peaks of the fundamental pulse. There is no observation of an energy shift of the XUV pulse, as has been reported with a chirped fundamental pulse [120] or an AC Stark shift due to a high intensity driving laser field.

The energy window of detection below the IP, E_{window}, depends on the maximum electric field that can be applied. For practical laboratory fields the detection window is about 200 meV under the IP of the atom.

[1] There is a fixed deviation of the observed angle and the calculated phase matching angle θ_{pm}^{ooe} for a negative, uniaxial crystal of 2.5°. Apparently the crystal was cut under 42.5° and not 45° as quoted.

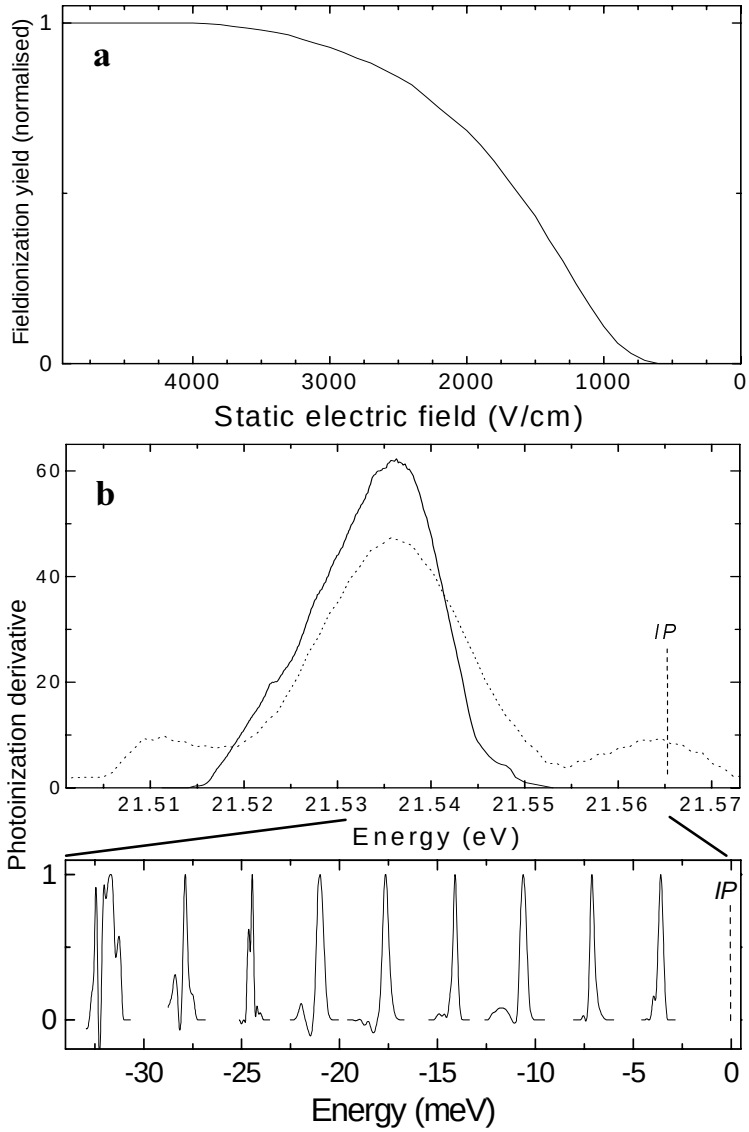

Figure 7.4: *a) Fieldionization yield as a function of applied electric field for the 7th harmonic of a UV pulse at 403.00 nm. b) The derivative of the curve shown in a) as a function of energy. The maximum is at 21.536 eV and the FWHM is 15 meV. The dotted line is the fundamental UV pulse where the energy scale is multiplied by 7. The Ne ionization potential is indicated with IP. c) An AC-Stark shift broadened narrowband laser pulse (2.0 cm^{-1}) at various energies, detected in Rb with the method described in the text. The energy steps are 3.5 meV where states are populated around $n \approx 20.7, 22.0, 23.5, 25.3, 27.7, 30.9, 35.5, 43$ and 60 (left to right). The energy scale is twice that of b).*

By selecting different atoms the energy windows range from Cs ($IP = 3.89$ eV) to He ($IP = 24.6$ eV). This range can even be extended to X-rays by using the Rydberg states of (multiply charged) ions. In Fig. 7.5 the ionization potential of various elements is depicted. In the range 3.5 to 20 eV there is always an atom or an ion with an ionization potential less than 0.5 eV away. The elements depicted are a selection; including all elements and (multiply) charged elements makes the range far larger and denser. Note that molecules make bad candidates for this method. As we have seen in chapter 2 and 3, other decay channels, such as predissociation and rotational autoionization, compete with fieldionization, which results in a lower fieldionization yield close to the saddlepoint. The quenching of fieldionization yield close to the saddlepoint would result in a broadening and a shift to higher energy of the derivative curve.

The resolution of the scheme is of the order of the energy spacing of the adjacent populated states. Hence the resolution increases closer to the *IP*. If the bandwidth of the excitation pulse exceeds the spacing between the populated states, the discrete character of the states is averaged out and all atoms show the same, average, field dependent photoionization. The lower limit of this method is at the energy at which the bandwidth of the XUV pulse equals the energy spacing Δ between the populated Rydberg states at the saddlepoint. The oscillator strength of an arbitrary state at the saddlepoint depends on the mixing with neighboring states. If there is a complete mixing, the spacing between two populated states is given by the average energy separation between neighboring Stark states, which is n^{-4} in the n-mixing regime. In case of no mixing, Δ is given by the average energy separation between neighboring Rydberg states, which is n^{-3} in the n-mixing regime. Since the saddlepoint energy

$$E = IP - 2\sqrt{F} = IP - 1/2n^2 \tag{7.5}$$

so that $F = 1/16n^4$ [1], the lower limit is when

$$\Delta = (16F)^{\alpha} = (4E_{window}^2)^{\alpha/4} \tag{7.6}$$

where $\alpha = 4$ for complete mixing and $\alpha = 3$ for no mixing. We have experimentally determined the resolution in Rb to be 0.25 meV for $E_{window} = 25$ meV (see Fig 7.4c). A narrowband dye laser (0.1 cm^{-1}) is used to excite high Rydberg-Stark states at various energies with steps of 3.5 meV. The bandwidth is AC Stark shift broadened to 0.25 meV caused by the intensity of the laser pulse ($\sim 10^9$ W/cm^2). Ignoring tiny resonances on the low-energy side of each detected spectrum, the method is reliable over $E_{window} = 25$ meV. A laser bandwidth of 0.25 meV and $\alpha = 4$ imply an energy window of 40 meV and $\alpha = 3$ an energy window of 6 meV. From Fig 7.4c we learn that $\alpha = 4$, since the window is larger than 6 meV, but more than two populated states must fall within the bandwidth of the laser for a reliable spectrum, because the window is not the full 40 meV. Below this energy window the method can still be used but one has to take care of atomic resonances that show up in the photoionization yield. This result demonstrates that the width of the XUV pulse shown in Fig. 7.4b is not instrumental limited but reflects the actual shape of the high order spectrum.

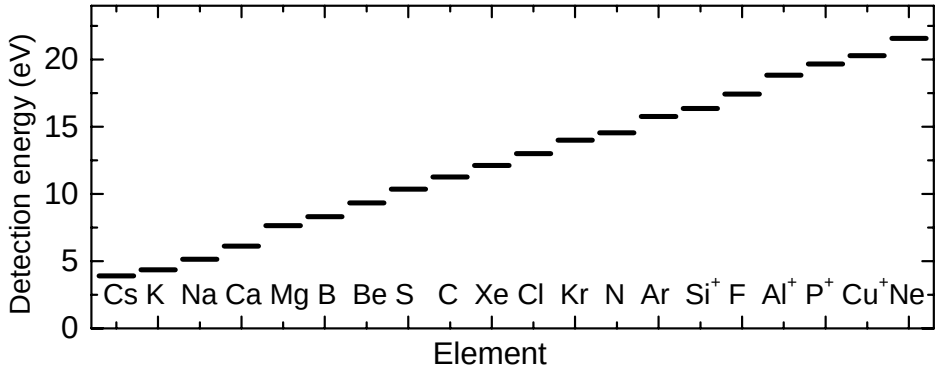

Figure 7.5: *The ionization potential for various elements and ions of elements between cesium and neon. There is always an element with an ionization potential within 0.5 eV from any energy between 3.5 and 20 eV. Each element has a detection window of 0.2 eV.*

With the help of the data in Fig. 7.4c we obtain the resolving power of the scheme in the XUV domain to be $\lambda/\Delta\lambda = 10^5$. This is comparable to the best grating spectrometers [109]. Once more, the resolving power is not a fixed number for an atom. The wavelength λ must be close to the ionization potential of the atom but the $\Delta\lambda$ increases as λ is closer to the IP.

Note that the atomic states populated by the XUV pulse can in principle also be read out by means of state selective field ionization (SFI) [121]: After the XUV excitation of the atoms in zero-field, the electric field is ramped, such that the time of ionization is a measure of the binding energy of the electron. We foresee two limitations to this version of probing the state distribution. First, the one-to-one correspondence of binding energy and time of ionization fails if the ionization pathways switch from adiabatic to diabatic. Hence the SFI technique is only applicable in a limited energy window. Second, since the Rydberg states are excited in zero-field the n Stark states are still degenerate. The spectrum is probed with an n times bigger spacing ($\alpha = 3$ rather than $\alpha = 4$) and the resolving power drops considerably.

7.5 Conclusion.

A novel method of detecting the wavelength and bandwidth of XUV pulses is presented. The method is based on the electric field dependence of photoionization probability of Rydberg states. The derivative of the fieldionization yield as a function of applied electric field shows the energy and the bandwidth of the pulses with a $\lambda/\Delta\lambda = 10^5$. We demonstrated the method with a tunable XUV laser source based on higher harmonic generation of the frequency doubled output of a 50 fs Ti-Sapphire laser. The spectral

profile of the 7th harmonic is detected with Ne. Each atom has a detection window of about 200 meV. By choosing an appropriate atomic gas one can apply this method in the range 3.5 - 20 eV.

Chapter 8

The streak camera operating in the XUV.

The atomic detection of XUV pulses can also be used to determine the temporal profile of the pulses. We present a new type of streak camera to measure the temporal shape of pulses in the XUV region: A cloud of noble gas atoms is used as a photocathode. The first results at 57 nm show a time resolution of 10 ps. Modifications to improve the time resolution are discussed. Using a noble gas as a photocathode has the potential to decrease the temporal resolution of the streak camera in the XUV to less than 0.5 ps.

8.1 Introduction.

Streak cameras are widely used to characterize the time profile of optical pulses. The frequency range in which streak camera's are sensitive stretches from THz [122], IR [123–125] and visible [17, 126] all the way to the X-ray region [127–131]. Applications range from monitoring the shape of ultrashort laser pulses to fluorescence lifetime measurements. Streak cameras have four components: a photocathode to convert the optical pulse into an electron replica, an acceleration region, a drift region where the electron replica is streaked by a set of deflection plates, i.e. the temporal profile is converted into a spatial profile, and a position sensitive read-out. The achievable temporal resolution of a streak camera depends on the temporal dispersion of the electron signal that arrives at the deflection plates. To minimize this dispersion one needs a photocathode with a minimum inherent energy spread and a high acceleration field. The performance of a particular photocathode varies widely with the wavelength of the optical pulse. Around the visible range [200-800 nm] various phosphors are available, with a high yield and a small inherent energy spread. Hence, the temporal resolution of streak cameras in the visible is better than 0.5 ps [126]. In the X-ray region metallic photocathodes are used like CsI or KBr. These photocathodes have a large inherent energy spread. However, at high photon energies of 100 eV or more, and by applying

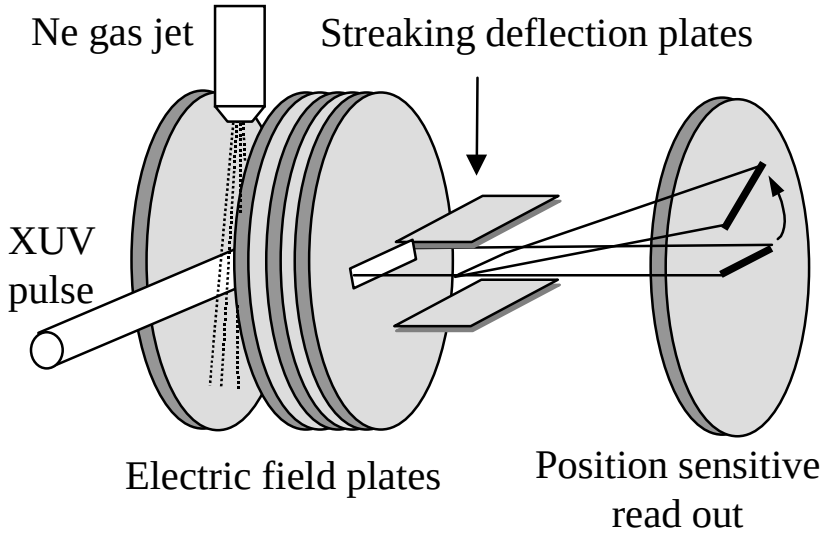

Figure 8.1: *Schematic outline of the XUV streak camera: The XUV pulse travels between two electric field plates where a pulsed valve injects a jet of noble gas. Photoionized electrons are accelerated towards a position sensitive read-out. The streaking deflection plates convert the temporal profile of the electrons into a position coordinate on the read-out.*

very strong acceleration fields (in the order of 100 kV/cm), the temporal resolution may be as good as 1 ps [128,129]. The XUV range with photon energies of 10-30 eV is a difficult region where neither phosphors (no sensitivity) nor metallic photocathodes (large $\Delta E/E$) perform well. We propose an atomic streak camera [17, 124, 125] with a noble gas acting as the photocathode [132]. There are several advantages of using a noble gas. There is no inherent energy spread because the energy of the initial state, the atomic ground state, is extremely narrow. Excitation just above the ionization threshold results in electrons with nearly zero kinetic energy and an energy spread which is equal to the bandwidth of the excitation pulse only, minimizing the temporal dispersion. One can choose which noble gas to use for ionization thresholds ranging from 12-24 eV (see table 1). In higher harmonic generation where a fundamental light pulse generates a number of odd harmonics, one can even selectively monitor a particular harmonic: If the polarization of the laser pulse is perpendicular to the electric field of the streak camera, only the photons with energies just above the ionization threshold are selectively detected; lower harmonics do not induce a photoionization signal, higher harmonics produce electrons with a large kinetic energy that miss the detector slit. Moreover, the cross sections of noble gasses are relatively high for a good conversion ratio (table 1).

noble gas	ionization threshold (eV)	cross section (Mb)
He	24.58	7.2
Ne	21.56	6.1
Ar	15.76	32
Kr	14.00	43
Xe	12.13	60

Table 1. *The ionization threshold [4] (for all noble gasses, except He, the lower spin state is taken) and the cross section of photoabsorption just above the ionization threshold of all noble gasses [9]. 1 Mbarn corresponds to* 10^{-18} cm^2.

8.2 Experimental.

The experimental setup to demonstrate the XUV application of the atomic streak camera is shown in Fig. 8.1. It is a slight adjustment in the streak camera set-up as described in the introduction. An XUV pulse is passing through the interaction region between two electrically charged plates in a background vacuum of 10^{-7} mbar. Ne atoms from a pulsed gas jet create a local, temporary pressure of approximately 10^{-2} mbar. Ionized photoelectrons (one per $\sim 10^3$ XUV photons) are accelerated in a field of typically 3 kV/cm through a slit (10 $\times$ 0.3 mm) towards a position sensitive read out (a set of microchannel plates and a phosphorscreen viewed by a CCD camera). In the trajectory of the electrons two additional plates affect the volume and time focussing (as described by Wiley and McLaren [133]). Two streaking deflection plates convert the arrival time at the deflection plates into a position coordinate on the read out. The electric field between the plates is switched from 2.5 kV/cm to -3 kV/cm in 300 ps by discharging a capacitor through a GaAs photosensitive switch.

To achieve an XUV pulse with a relatively narrow bandwidth the output of a Ti-Sapphire laser is frequency-doubled with a 20-mm KDP crystal as described in the previous chapter. The resulting UV pulse (3.1 eV) has a bandwidth of about 5 meV and a duration of 0.5 ps. The pulse is focussed into a Xe gas jet to generate high harmonics. Ne can be ionized by the 7th harmonic ($\sim$22 eV) and higher. The bandwidth of the 7th harmonic pulse is measured in the previous chapter to be 15 meV. To selectively monitor the ionization of Ne with the 7th harmonic, the laser polarization is chosen to be perpendicular to the acceleration field in the interaction region. All higher harmonics, >7, create electrons with a high kinetic energy (>6 eV) perpendicular to the electric field, so that they miss the detection slit. Rotation of the polarization would cause all harmonics $\geq$7th to contribute to the signal.

8.3 The slope of the streak camera.

A typical streak image is shown in Fig. 8.2a. The finite speed of excitation light along the x-axis that initiates the electron emission will lead to a slope of the electron signal

on the CCD screen of the streak camera. Since the slope is a calibration for the time axis, the y-axis, it is important to understand how it depends on the deflection field, kinetic energy of the electrons and the distance of the phosphorscreen with respect to the deflection plates. We find the *dy/dx*, where y is the vertical displacement of the electron signal, owing to the deflection plates, and x is the length of the signal, given by the length of the detection slit by:

$$\frac{dy}{dx} = \frac{dy/dt}{dx/dt} = \frac{(dy/dV)(dV/dt)}{dx/dt} \tag{8.1}$$

where *dx/dt* is the speed of light c and *dV/dt* is the voltage ramp on the deflection plates. We have to find the vertical displacement of the electron signal as a function of deflection field, *dy/dV*. An electron has a kinetic energy E_{kin} (expressed in eV) and therefore a finite transit time along the deflection plates with a length l. The transit time t_{trans} is

$$t_{trans} = l\sqrt{m/2eE_{kin}} \tag{8.2}$$

where e and m are the charge and the mass of the electron, respectively. During the transit time the electrons acquire a velocity in the y-direction. The velocity is the integration of the acceleration a due to the force exerted by the deflection field V on the passing electron during the transit time along the deflection plates with separation s:

$$v_y = \int_{t_{trans}} a(t)dt = -\frac{eV}{ms}t_{trans} \tag{8.3}$$

The displacement y of the electron on the phosphorscreen with respect to the position without deflection is found by multiplying the acquired velocity with the time it takes to travel through the field free region and arrive at the phosphorscreen at a distance d:

$$y = v_y\frac{d}{l}t_{trans} = -\frac{ld}{2sE_{kin}}V \tag{8.4}$$

so that

$$\frac{dy}{dV} = -\frac{ld}{2sE_{kin}} \tag{8.5}$$

For the voltage ramp on the deflection plates we assume that the voltage decreases linearly from the maximum V_{max} to the minimum V_{min}, uniform over the whole plates in a ramp time τ:

$$\frac{dV}{dt} = \frac{V_{\max} - V_{\min}}{\tau} \tag{8.6}$$

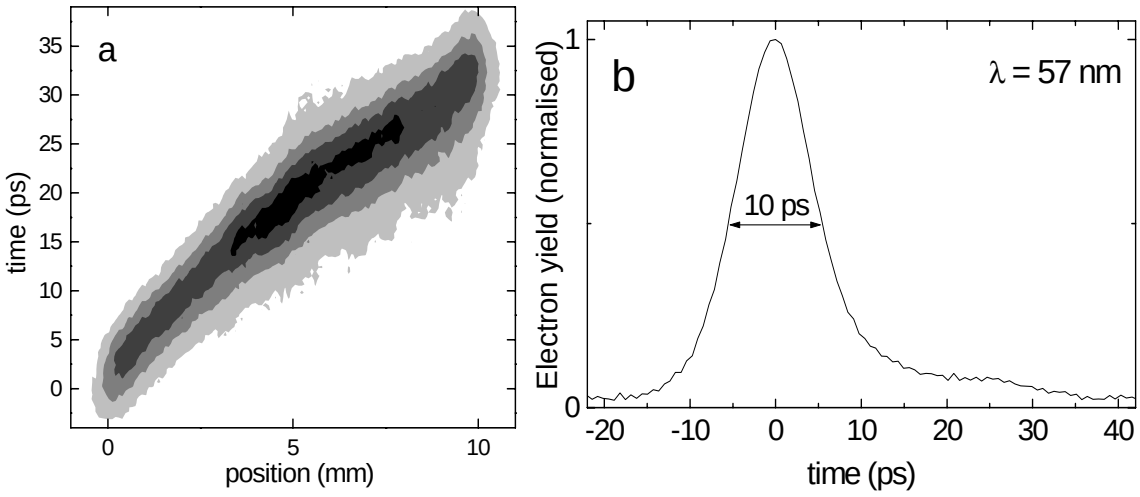

Figure 8.2: *a) A streak camera image after excitation of Ne with 21.7 eV (57 nm). The acceleration field is 3 kV/cm. The optical pulse travels 10 mm from left to right, the deflection in time is upward (33 ps). b) Integrated electron yield along the signal line of Fig. 2a. The observed peak has a FWHM of 10 ps.*

The slope of the electron signal of a streak image is thus given by:

$$\frac{dy}{dx} = -\frac{(V_{\max} - V_{\min})ld}{2c\tau s E_{\text{kin}}} \tag{8.7}$$

Typically the field is switched from V_{max} = +800, to V_{min} = -1000 in a time $\tau = 300$ picoseconds. The length of the deflection plates $l = 10$ mm, the separation of the plates $s = 3$ mm and the distance d of the position sensitive readout 0.20 m. With a kinetic energy of 3 keV the streak camera will display a slope of $dy/dx = 2.2$. In practice the slope is about half that value.

8.4 Results and discussion.

In Fig. 8.2a the streak camera image is shown resulting from the photoionization of Ne with a 0.5 ps XUV pulse. The optical pulse travels from left to right, the deflection is upwards. The image is an average of 100 shots, where each image is automatically cross-correlated with a reference image and shifted to remove time jitter. Owing to the relative high cross section of Ne, a reliable streak image can be made with about 10^4 XUV photons per shot. The slant dy/dx is about 1. The signal is integrated along the slant and results in Fig. 8.2b. The temporal profile has a FWHM of 10 ps. Since the detected XUV pulse is at most 0.5 ps this streak camera can, as yet, act to determine XUV pulses of 10 ps or longer.

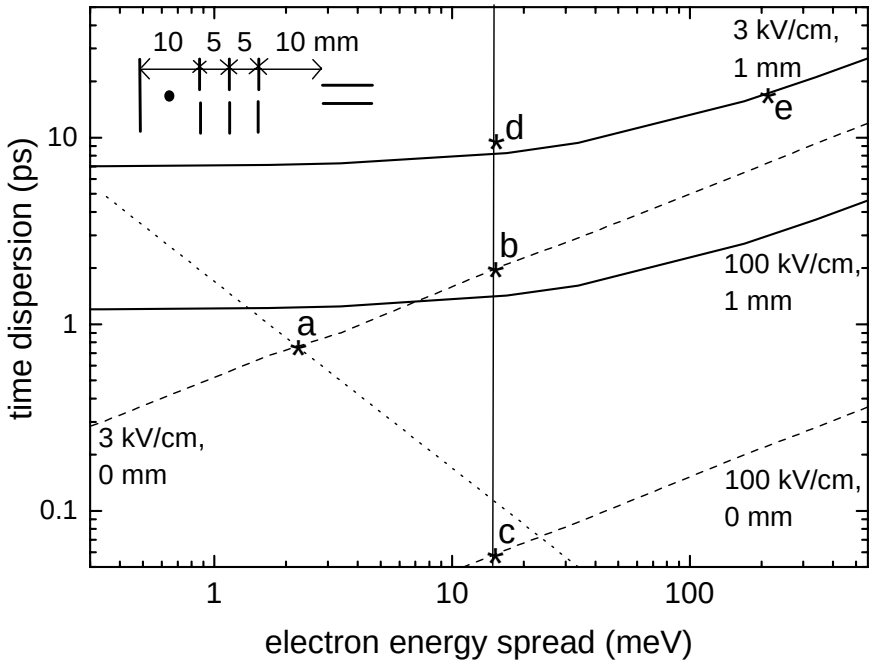

Figure 8.3: *Calculated time dispersion of the electron signal at the deflection plates as a function of electron energy spread at the photocathode. The time dispersion is simulated for two acceleration fields: 3 and 100 kV/cm. The excitation volume is a cylinder with a diameter of 0 mm (dashed lines) and 1 mm (solid lines). The dotted line is drawn where the time dispersion equals the time duration of a Fourier-transform limited excitation pulse. The (d) is the experimental data point of Fig. 2, the other characters are explained in the text. The inset shows the geometry of the streak camera with 4 electric field plates and 2 (horizontal) deflection plates. The excitation is at the •. The trajectory of the electrons to the deflection plates is 25 mm.*

What are the main limitations for the temporal resolution of the atomic streak camera and how can these be minimized? The applied acceleration field is 3 kV/cm. Obviously, increasing the field will shorten the time that the electron replica can disperse. Shown in Fig. 8.3 is the calculated electron time dispersion upon arrival at the deflection plates as a function of electron energy spread. The simulation is based on classical electron trajectories in our streak camera configuration. For the dashed lines the assumption is that the XUV pulse is focused to a cylinder with zero diameter, the plate separation is 5 mm and the deflection plates are positioned 10 mm behind the last plate as shown in the inset in Fig. 8.3. As mentioned before, in our case the only contribution for the energy spread of the electrons is due to the bandwidth of the short optical pulse. The dispersion time is simulated for 3 kV/cm and 100 kV/cm (as is used in Ref. [129]) in the interaction region. The dotted line in Fig. 8.3 indicates where

the time dispersion equals the pulse duration of a Fourier-transform limited pulse of that bandwidth. Below the dotted line the streak image is a true representative of the optical pulse, above the dotted line the camera is temporal resolution limited. The shortest observable pulse in a field of 3 kV/cm is a Fourier-transform limited pulse of 0.8 ps (a). The XUV pulse that is detected in Fig. 8.2 has a width of 15 meV (indicated by the vertical line in Fig. 8.3). According to our simulation the minimum temporal resolution of the streak camera is 2 ps (b). Increasing the acceleration field decreases the time dispersion dramatically: In a field of 100 kV/cm, the time dispersion is only 60 fs (c). Note that the simulation is for the worst case scenario with zero energy, only bandwidth. Kinetic energy of the electrons in the direction of the deflection plates will decrease the time dispersion even more.

There is still a factor of 5 difference in the observed temporal resolution in Fig. 8.2 and the time dispersion as calculated in Fig 8.3. This is due to the finite volume of excitation. The XUV beam was not focussed and excited Ne atoms in a cylinder with a diameter of $\sim$1 mm. That volume is focussed in the propagation direction by the Wiley-McLaren time focussing [133] at the deflection plates. However, the focus is at one point in space whereas the deflection plates have a certain length along the propagation (10 mm). The imperfect time focussing is expected to give rise to a time dispersion of about 7 ps in a field of 3 kV/cm (1.2 ps for 100 kV/cm). Furthermore, the excitation volume is projected on the CCD screen giving rise to an additional limitation for the temporal resolution. The quadratic sum of the imperfect time focussing and the projection of the excitation volume is also shown in Fig. 8.3 (solid lines). In our experiment (3 kV/cm and 1 mm diameter) we expect 8.5 ps which agrees well with the observed 10 ps (d) as is shown in Fig. 8.2. An improvement could therefore be made by refocusing the XUV pulse with a focussing grating or mirror. The absolute minimum temporal resolution, however, remains due to the energy width of the electrons.

To show the influence of the energy spread, the experiment was repeated with the 9th harmonic of the fundamental IR pulse to ionize krypton. The wavelength of the 9th harmonic ($\sim$88 nm) is at the ionization potential of Kr. This leads again to electrons with nearly zero kinetic energy in the same excitation volume but now with a very large bandwidth. The bandwidth of the harmonic pulses of the fundamental IR is not measured but we can estimate the bandwidth to be $\sqrt{N}$ times the bandwidth of the fundamental pulse for the N'th harmonic (See e.g. Ref. [110]). Since the bandwidth of the IR pulse is 35 nm, we estimate the 9th harmonic to be 205 meV. The observed streak camera image exhibits a temporal profile with a FWHM of 45 ps, which is much worse than the expected 17 ps in Fig. 8.3 (e).

8.5 Conclusion.

An atomic streak camera in the XUV region is demonstrated by using a noble gas as a photocathode. The main limitation for the time resolution, the energy spread of the photocathode, is abolished this way. The energy spread of the electrons, leading to

the time dispersion of arrival at the deflection plates is only due to the bandwidth of the optical pulse. The first results show a temporal resolution of 10 ps. The detection can be improved by focussing the XUV pulse and applying a higher acceleration field. Our expectation is that this new technique has the potential to minimize the temporal resolution below 0.5 ps.

Appendix:
The streak circuit.

The heart of the streak camera is the circuit that produces a fast switch of the electric field on the deflection plates. A schematic representation is displayed in Fig. 4. A capacitor of 150 pF is charged with a negative voltage. One of the deflection plates is positively biased. If the resistance of the GaAs photosensitive switch is reduced by the trigger laser pulse, the capacitor is discharged on the deflection plate, creating the fast voltage ramp. Two 1 MΩ resistances act as barriers of high frequency signals. The maximum voltage ramp speed is determined by the RC and LC times of the circuit.

The capacity of the deflection plates C is given by:

$$C = \varepsilon_0 \frac{A}{s} = 8.85\ 10^{-12} \frac{2\ 10^{-4}}{2\ 10^{-3}} = 0.9\ pF \tag{8}$$

where ε_0 is the permittivity in vacuum, A the surface of the plates and s the distance between the plates. The self-inductance of the circuit L is given by:

$$L = \mu_0 \frac{A}{l} w^2 = 4\pi\ 10^{-7} \frac{1\ 10^{-3}}{0.1} 1^2 = 13\ nH \tag{9}$$

where μ_0 is the permeability in vacuum, A is the enclosed surface, l the length of the wire between the top and bottom plate and w is the number of windings. We obtain a rough estimate of the response time of the circuit by calculating the LC time, where $t_{LC} = \sqrt{LC} = 100$ ps and the RC time, where a resistance $R = 220\ \Omega$ leads to a RC time of 200 ps. The small resistance is added to damp out the oscillation that would occur in the circuit with just a capacity and inductance. Applying the laws of Kirckhoff [7] confirms the switching time to be about 300 ps.

A new design of the circuit was realized to make the voltage ramp faster. The 220 Ω resistance in the fast loop has been removed and all elements were made more compact to decrease the self-induction ($L = 4$ nH). Actually, the whole new circuit fits inside a matchbox. An 15 GHz analog scope determined the switching time to be about 150 ps. This fast switching time, however, creates more problems than it solves. The switching time is faster than the interaction time of the electrons with the deflection plates. A typical 2 keV electron still takes 377 ps to pass the 10 mm deflection plates. The huge bias field will result in deflection of the electron signal away from the detector.

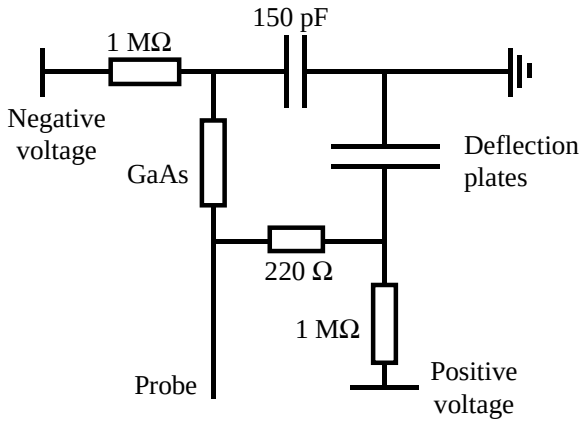

Figure 4: *A schematic representation of the streak camera circuit. A 150 pF capacitor is charged to a negative voltage via the 1 MΩ resistance. The resistance of the unexposed GaAs photoswitch is about 500 MΩ. If a lightflash falls on the GaAs a discharge from the capacitor will flow to the deflection plates, switching it rapidly from positive to negative. If the photoconductivity of the GaAs drops to zero again, the deflection plates recharge to a positive voltage via the second 1 MΩ resistance. A probe is added to monitor the switch field outside the vacuum.*

Moreover, the spreading of the voltage on a plate has a speed of $c/\sqrt{\epsilon_r}$, where ϵ_r is the relative dielectric constant of the medium around the plate. Since the plate is in vacuum, the speed of the electronic signal is equal to the speed of light. Therefore, faster switching implies a larger spatial voltage ramp on the plates that leads to a electron signal line on the read out that is curved (the notorious 'smiley'). The spatial ramp also occurs with 'slow' switching but the effect is less severe (Note the slight curvature of Fig. 8.2). Fortunately, during the actual experiment the effective field for the electrons is actually fairly uniform: The plates are not terminated by a resistance and a full reflection of the field will be back in the deflection region in less then 100 ps. The two counter propagating spatial ramps exactly cancel the ramp, making a 'flat' effective field within 100 ps.

The photosensitive switch of GaAs has a resistance of 10^8 Ωcm. The piece in the streak circuit of 10×5×1 mm has a resistance of $R = 500$ MΩ. If GaAs is subject to light, however, electron-hole pairs are created and the resistance lowers to nearly zero. The color of the excitation light is very important: The bandgap of GaAs is 1.424 eV, and the wavelength of the light has to be shorter than 870 nm. The absorption coefficient α at this wavelength increases rapidly to about 10^4 cm^{-1} [8]. The intensity I(x) of the incoming light with an intensity I_0 decreases with $I(x) = I_0 \exp(-\alpha x)$ where x is the penetration depth. The intensity has dropped with a factor 1/e after 1 μm. For $\lambda = 600$ nm the absorption coefficient has increased to 2 10^4 cm^{-1} and for the doubled light of a Ti:Sapphire laser, 400 nm, α has increased to even 5 10^5 cm^{-1}. This

means that the intensity of the excitation light has already dropped with 1/e after 20 nm penetration! In the last case two problems occur that were not of importance in former experiments [16] where a wavelength of 600 nm was used. The electron-hole pairs are created in a very small volume, making the density of photocarriers very high. Direct recombination of an electron with a hole becomes also of importance besides the recombination at impurities, decreasing the time that the GaAs is photoconductive. The second problem is due to the surface of the material. At the surface exists a space-charge layer set up by the equilibrium interchange between electrons in surface states and the interior. These problems together decrease the carrier lifetimes close to the surface easily with orders of magnitude [10]. Shortly after the initial excitation pulse there will be only a very thin slice of photoconducting GaAs, just underneath the surface of the material. The effective resistance remains higher than one would expect. Probing the deflection plates with 100 μJ of excitation light of 600 nm leads to an effective switching time of about 300 ps. Using 100 μJ of excitation light of 400 nm, however, leads to an effective switching time of 2 ns. Since the capacity and inductance did not change the resistance of the GaAs must have a minimum in the order of 2000 Ω. High residual resistance is proved by removing the resistance of 220 Ω, which did not lead to an oscillatory behavior of the field on the plates. For experiments with 400 nm the streak circuit is used with excitation light of >200 μJ.

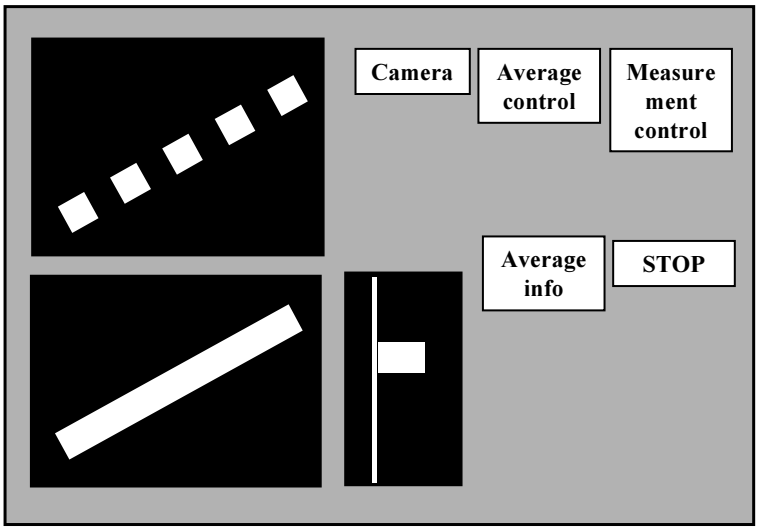

Figure 5: *Schematic outline of the streak camera software for image stabilisation. In the upper left frame the single shot raw images are shown. In the lower left the average is shown, with or without stabilisation. The integration along the signal line is done automatically and the result is displayed in the bottum-middle frame.*

Switching with a photosensitive switch leads to a time jitter for the deflection plates and therefore a position jitter for the signal on the camera. Labview software has been

developed in order to remove the position jitter that would result in a smeared signal for an average. The basis is that a user can set an approved image as a reference image. Each subsequent image is then cross correlated with the reference image to find the maximum overlap before it is added to the average. An adjustable acceptance threshold is put in for maximum shift of the image and minimum overlap with the reference image. Rejected images do not go to the average image. This way the FWHM of the average signal is about the FWHM of the reference signal but has a far better S/N ratio. Integration of the image along the signal lines is done automatically also. The program finds the length of the signal line (1 cm = 33 ps) and the slope of the signal line giving the time calibration of the electron yield. The user sees three images simultaneously on the screen: the last raw image, the average and the integrated signal as function of emission time. Free running the camera works at 50 Hz. With all the calculations the frequency decreases to 15 Hz, which is still fast enough to obtain good averages of hundreds of images within a minute.

Bibliography

[1] *Rydberg Atoms*; T.F. Gallagher, Cambridge University Press (1994).

[2] *Rydberg states of atoms and molecules*, R.F. Stebbings and F.B. Dunning, Cambridge University Press, Cambridge (1983).

[3] *Highly excited atoms*, J.-P. Connerade, Cambridge University Press, Cambridge (1998).

[4] *Atomic Energy Levels*, C.E. Moore, Circular of the National Bureau of Standards 467 (1949).

[5] *Electronic spectra and electronic structure of polyatomic molecules*, G. Herzberg, van Nostrand Reinhold company, New York (1966).

[6] *ZEKE Spectroscopy*; E.W. Schlag, Cambridge University Press (1998).

[7] *Electronisch Vademecum*; Kluwer Technische Boeken B.V., Deventer (1980).

[8] *Electronic Material Science for integrated Circuits in Si and GaAs*; J.W. Mayer and S.S. Lau, Macmillan Publishing Company, New York.

[9] *Photoabsorption, photoionization and photoelectron spectroscopy*, J. Berkowitz, academic press NY (1979).

[10] *Photoconductivity of solids*; R.H. Bube, J. Wiley & Sons Inc. New York (1960).

[11] *Handbook of Nonlinear Optical Crystals*, V.G. Dmitriev, G.G. Gurzadyan and D.N. Nikogosyan, Springer-Verlag, Berlin (1991).

[12] *Physics*, H.C. Ohanian, W.W. Norton & Company, New York, (1989).

[13] Thesis, Bart Noordam, University of Amsterdam (1990).

[14] Thesis, Jan Hoogenraad, University of Amsterdam (1997).

[15] Thesis, Rutger Vrijen, University of Amsterdam (1997).

[16] Thesis, Marcel Lankhuijzen, University of Amsterdam (1997).

[17] G.M. Lankhuijzen and L.D. Noordam; Opt. Commun. **129**, 361 (1996).

[18] P.M. Koch and D.R. Mariani, Phys. Rev. Lett. **46**, 1275 (1981).

[19] T. Ebata, Y. Anezaki, M. Fujii, N. Mikami and M. Ito, J. Phys. Chem. **87**, 4773 (1983).

[20] S.T. Pratt, J.L. Dehmer and P.M. Dehmer, J. Chem. Phys. **90**, 2201 (1989).

[21] S.T. Pratt, J. Chem. Phys. **98**, 9241 (1993).

[22] C.R. Mohon, G.R. Janik and T.F. Gallagher, Phys. Rev. A **41**, 3746 (1990).

[23] F. Merkt, H.H. Fielding and T.P Softly, Chem. Phys. Lett, **202**, 153 (1993).

[24] A. Giusti-Suzor and Ch. Jungen, J. Chem. Phys. **80**, 986 (1984).

[25] F. Fujii an N. Morita, J. Chem. Phys. **98**, 4581 (1993).

[26] A. Fujii an N. Morita, Laser Chem. **13**, 259 (1994).

[27] M.J.J. Vrakking, J. Chem. Phys. **102**, 8818 (1995).

[28] M.J.J. Vrakking, J. Chem. Phys. **105**, 7336 (1996).

[29] Y. Anezaki, T. Ebata, N. Mikami and M. Ito, Chem. Phys. **97**, 153 (1985).

[30] M. Bixon and J. Jortner, J. Phys.Chem. **99**, 7466 (1995).

[31] M. Bixon and J. Jortner, J. Chem. Phys. **105**, 1363 (1996).

[32] F. Remacle and R.D. Levine, J. Chem.Phys. **105**, 4649 (1996).

[33] F. Remacle and M.J.J. Vrakking, J. Phys. Chem. A **102** 9507 (1998).

[34] F. Robicheaux, C. Wesdorp and L.D. Noordam, Phys. Rev. A **60**, 1420 (1999); **60**, R3377 (1999).

[35] D.A. Harmin, Phys. Rev. A **24**, 2491 (1981); **26**, 2656 (1982).

[36] D.J. Armstrong and C.H. Greene, Phys. Rev. A. **50**, 4956 (1994).

[37] E.S. Chang and U. Fano, Phys. Rev. A **6**, 173 (1972).

[38] C.H. Greene and C. Jungen, Adv. At. Mol. Phys. **21**, 51 (1985).

[39] D.T. Biernacki and S.D. Colson, J. Chem. Phys. **89**, 2599 (1988).

[40] R. Engleman Jr. and P.E. Rouse, J. Mol. Spec. **37**, 240 (1971).

[41] W.G. Mallard, J.H. Miller and K.C. Smith, J. Chem. Phys. **76**, 3483 (1982).

[42] S.N. Dixit, D.L. Lynch, V. McKoy and W.M. Huo, Phys. Rev. A **32**, 1267 (1985).

[43] W.L. Glab and K. Qin, J. Chem. Phys. **99**, 2345 (1993).

[44] Chr. Bordas, P. Brevet, M. Broyer, J. Chevaleyre and P. Labastie, Europhys. Lett. **3**, 789 (1987).

[45] T.P. Softley, A.J. Hudson and R. Watson, J. Chem. Phys. **106**, 1041 (1997).

[46] H.H. Fielding and T.P. Softley, Phys. Rev. A **49**, 969 (1994).

[47] C.A. Raptis and S.T. Pratt, Chem. Phys. Lett. **303**, 281 (1999); Chem. Phys. **112**, 2815 (2000); Phys. Rev. Lett. **84**, 5078 (2000).

[48] J.A. Bacon and S.T. Pratt, J. Chem. Phys. **112**, 4153 (2000); J. Chem. Phys. **113**, 7188 (2000).

[49] S.R. Langford, A.J. Orr-Ewing, R.A. Morgan, C.M. Western, A. Rijkenberg, C.R. Scheper, W.J. Buma, C.A. de Lange, J. Chem. Phys. **108**, 6667 (1998).

[50] K. Müller-Dethlefs and E.W. Schlag, Ann. Rev. Phys. Chem. **42**, 109 (1991).

[51] W. Habenicht, G. Reiser and K. Müller-Dethlefs, J. Chem. Phys. **95**, 4809 (1991).

[52] G. Reiser, W. Habenicht and K. Müller-Dethlefs, J. Chem. Phys. **98**, 8462 (1993).

[53] R.G. Tonkyn, J.W. Winniczek and M.G. White, Chem. Phys. Lett. **164**, 137 (1989).

[54] L. Zhu and P.M. Johnson, J. Chem. Phys. **94**, 5769 (1991).

[55] G.P. Bryant, Y. Jiang, M. Martin and E.R. Grant, J. Phys. Chem. **96**, 6875 (1992).

[56] H. Dickinson, D. Rolland and T.P. Softley, Phil. Trans. R. Soc. Lond. A, **355**, 1585 (1997).

[57] D.H. Mordaunt, M.N.R. Ashfold, R.N. Dixon, J. Chem. Phys. **104**, 6460 (1996); **104**, 6472 (1996)

[58] T. Nishiya, J. Chem. Phys. **96**, 4276 (1992).

[59] J.P. Reid, R.A. Loomis, S.R. Leone J. Phys. Chem A **104**, 10139 (2000).

[60] D. Edvardsson, P. Baltzer, L. Karlsson, B. Wannberg, D.M.P. Holland, D.A. Shaw and E.E. Rennie, J. Phys. B **32**, 2583 (1999).

[61] M.N.R. Ashfold, R.N. Dixon and R.J. Stickland, Chem. Phys. **88**, 463 (1984).

[62] M.J. Schultz and J. Wei, J. Chem. Phys. **92**, 5951 (1990).

[63] M.N.R. Ashfold, C.L. Bennett, R.N. Dixon, P. Fielden, H. Rieley and R.J. Stickland, J. Mol. Spec. **117**, 216 (1986).

[64] B. Broers, J. F. Christian, J. H. Hoogenraad, W. J. van der Zande, H. B. van Linden van den Heuvell and L. D. Noordam, Phys. Rev. Lett. **71**, 344 (1993)

[65] G.M. Lankhuijzen and L.D. Noordam, Phys. Rev. A **52**, 2016 (1995).

[66] D.T. Cramb and S.C. Wallace, J. Chem. Phys. **101**, 6523 (1994).

[67] F. Zernike, J. Opt. Soc. A **54**, 1215 (1964).

[68] A. Kohlhase and S. Kita, Rev. Sci. Instrum. 57, 2925 (1986).

[69] A.T.J. Eppink and D.H. Parker, Rev. Sci. Instrum. **68**, 3477 (1997).

[70] C. Nicole, I. Sluimer, F. Rosca-Pruna, J.B.M. Warntjes, M. Vrakking, C. Bordas, F. Texier and F. Robicheaux; Phys. Rev. Lett. **85**, 4024 (2000).

[71] L. Wang and R.D. Knight, Phys. Rev A **34**, 3902 (1986).

[72] K. Maeda, K. Ueda and K. Ito, J. Phys. B **26**, 1541 (1993); Phys. Rev. A **45**, 527 (1992).

[73] M.J.J. Vrakking and Y. T. Lee, J. Chem. Phys. **102**, 8833 (1995).

[74] W.E. Ernst, T.P. Softley and R.N. Zare, Phys. Rev. A **37**, 4172 (1988).

[75] A. Fujii and N. Morita, J. Chem. Phys. **103** 6029 (1995); **98** 4581 (1993); Laser Chem. **13** 259 (1994).

[76] S.T. Pratt, J. Chem. Phys. **108,** 7131 (1998).

[77] X. Wang and W.E. Cooke, Phys. Rev. Lett. **67**, 976 (1991); Phys. Rev. A, **46**, 4347 (1992); Phys. Rev. A, **46**, R2201 (1992).

[78] A. ten Wolde, L.D. Noordam, H.G. Muller, A. Lagendijk and H.B. van Linden van den Heuvel, Phys. Rev. Lett. **61**, 2099 (1988).

[79] W.E. Cooke *et al*, Phys. Rev. Lett. **40**, 178 (1978).

[80] L.D. Noordam, A. ten Wolde, A. Lagendijk and H.B. van Linden van den Heuvel, Phys. Rev. A **40**, 6999 (1989).

[81] J.E. Thoma and R.R. Jones, Phys. Rev. Lett. **83,** 516 (1999).

[82] J.G. Story and H.N. Ereifej, Phys. Rev. Lett. **86**, 612 (2001).

[83] M.D. Lindsay, C.J. Dai, L.T. Cai, and T.F. Gallagher, Phys. Rev. A, **46**, 3789 (1992); see Eqs. (14) and (16).

[84] M.D. Lindsey, C.J. Dai, B.J. Lyons, C.R. Mahon and T. F. Gallagher, Phys. Rev. A, **50** 5058 (1994).

[85] F. Robicheaux and W.T. Hill, Phys. Rev. A **54**, 3276 (1996); see Eqs. (4) and (7).

[86] G. Tanner, K. Richter and J.-M. Rost, Rev. Mod. Phys. **72**, 497 (2000).

[87] H. Chi and K. Huang, Phys. Rev. A **50**, 392 (1994).

[88] W. Huang, X. Xu, C. Xu, P. Xue, M. Xue and D. Chen, Phys. Rev. A **54**, 5423 (1996).

[89] U. Eichmann, P. Brockmann, V. Lange and W. Sandner, J. Phys. B **22**, L361 (1989); Phys. Rev. Lett. **64**, 274 (1990).

[90] S. Cohen, P. Camus and A. Bolovinos, J. Phys. B **26**, 3783 (1993).

[91] M. Seng, M. Halka, K.-D. Heber and W. Sandner, Phys. Rev. Lett. **74**, 3344 (1995).

[92] C. Rosen, M. Dörr, U. Eichmann and W. Sandner, Phys. Rev. Lett. **83**, 4514 (1999).

[93] H. Kjeldsen, J.B. West, F. Folkmann, H. Knudsen and T. Andersen, J. Phys B **33**, 1403 (2000).

[94] C.J. Dai, G.W. Schinn, and T.F. Gallagher, Phys. Rev. A **42**, 223 (1990); G.W. Schinn, C.J. Dai, and T.F. Gallagher, Phys. Rev. A **43**, 2316 (1991).

[95] J.G. Story, D.I. Duncan, and T.F. Gallagher, Phys. Rev. Lett. **71**, 3431 (1993).

[96] N.J. van Druten and H.G. Muller, J. Phys. B **29**, 15 (1996).

[97] L.D. Noordam, H. Stapelfeldt, D.I. Duncan, and T.F. Gallager, Phys. Rev. Lett. **68**, 1496 (1992).

[98] B.J. Lyons, D.W. Schumacher, D.I. Duncan, R.R. Jones, and T.F. Gallager, Phys. Rev. A **57**, 3712 (1998).

[99] R.R. Jones, Phys. Rev. A **57**, 446 (1998).

[100] F. Robicheaux, Phys. Rev. A **62**, 033406.

[101] J. H. Hoogenraad and L.D. Noordam in *Super-Intense Laser-Atom Physics*, edited by B. Pireaux; Plenum Press, New York, 269 (1993) .

[102] G. M. Lankhuijzen, M. Drabbels, F. Robicheaux, and L. D. Noordam, Phys. Rev. A **57**, 440 (1998).

[103] V.L. Jacobs, J. Davis, and P.C. Kepple, Phys. Rev. Lett. 37, 1390 (1976); V.L. Jacobs and J. Davis, Phys. Rev. A **19**, 776 (1979).

[104] A. Müller, D.S. Belic, B.D. DePaola, N.Djuric, G.H. Dunn, D.W. Mueller and C. Timmer, Phys. Rev. Lett. **56**, 127 (1986).

[105] F. Robicheaux and M.S. Pindzola, Phys. Rev. Lett. **79**, 2237 (1997); T. Bartsch, A. Müller, W. Spies and J. Linkemann, Phys. Rev. Lett. **79**, 2233 (1997).

[106] L. Ko, V. Klimenko, and T.F. Gallagher, Phys. Rev. A, **59,** 2126 (1999).

[107] N.O. Body, C. Hecks, T. Hese, R.E. Ferences, A. Nyway, Phil. Trans. R. Soc. Lond. A, **5**, 581 (1837).

[108] L.D. Noordam, M.P. de Boer, and H.B. van Linden van den Heuvel, Phys. Rev. A **41**, 6267 (1990).

[109] Spectrometer resolutions can be found on the webpages of the numberous synchrotron radiation facilities. Examples of a description of a grazing incidence vacuum spectrograph e.g.: F.G. Meijer, J. Phys. E, **12**, 129 (1979); F.G. Meijer, Meas. Sci. Technol. **10**, 367 (1999); Z. Hussain, W. R. A. Huff, S.A. Kellar, E. J. Moler, P.A. Heimann, W. McKinney, H.A. Padmore, C.S. Fadley and D.A. Shirley, J. Elec. Spec **80**, 401 (1996).

[110] L. Nugent-Glandorf, M. Scheer, M. Krishnamurthy, J.W. Odom and S.R. Leone, Phys. Rev. A **62**, 023812 (2000).

[111] J. Larsson, E. Mevel, R. Zerne, A. L'Huillier, C.G. Wahlström and S. Svanberg, J. Phys. B **28**, L53 (1995).

[112] Ph. Balcou, P.Salières, K.S. Budil, T. Ditmire, M.D. Perry and A. L'Huillier, Z. Phys. D. **34**, 107 (1995).

[113] J. Larson, E. Mevel, R. Zerne, A. LHuillier, C.G. Wahlstrom and S. Svanberg, J. Phys. B **28**, L53 (1995); A. L'Huillier and Ph. Balcou, Phys. Rev. Lett. **70**, 774 (1993).

[114] H.J. Bakker, W. Joosen and L.D. Noordam, Phys. Rev. A **45**, 5126 (1992).

[115] G.C. Bhar, P. Kumbhakar, U. Chatterjee, A.M. Rudra, A. Nagahori, Opt. Comm. **176**, 199 (2000).

[116] S. Sayama, M. Ohtsu, Opt. Comm. **137**, 295 (1997).

[117] U. Morgner, F.X. Kärtner, S.H. Cho, Y. Chen, H.A. Haus, J.G. Fujimoto, E.P. Ippen, Opt. Lett. **24**, 411 (1999).

[118] D.H. Sutter, G. Steinmeyer, L. Gallmann, N. Matuschek, F. Morier-Genoud, U. Keller, V. Scheuer, G. Angelow, T. Tschudi, Opt. Lett. **24**, 631 (1999).

[119] L.D. Noordam, H.J. Bakker, M.P. de Boer and H.B. van Linden van den Heuvell, Opt. Lett. **15**, 1464 (1990).

[120] J. Zhou, J. Peatross, M.M. Murnane, H.C. Kapteyn and I.P. Christov, Phys. Rev. Lett. **76**, 752 (1996).

[121] F. Robicheaux, C. Wesdorp and L. D. Noordam, Phys. Rev. A **62**, 043404 (2000).

[122] Z. Jiang, F.G. Sun and X.C. Zhang, Opt. Lett. **24**, 1245 (1999).

[123] C.W. Rella, A.F.G. van der Meer and L.D. Noordam, Opt. Comm. **180**, 141 (2000).

[124] G.M. Drabbels and L.D. Noordam, Opt. Lett. **22**, 1436, (1997).

[125] M. Lankhuijzen and L.D. Noordam, Nucl. Instrum. Methods Phys. Res. A, **375**, 651 (1996); M. Drabbels, G.M. Lankhuijzen and L. D. Noordam, IEEE J. QUANTUM ELECT. **34**, 2138 (1998).

[126] Very good results are achieved by commercial companies like Hamamatsu.

[127] H. Shiraga, N. Miyanaga, M. Heya, M. Nakasuji, Y. Aoki, H. Azechi, T. Yamanaka and K. Mima, Rev. Sci. Instrum. **68**, 745 (1997).

[128] J. Larsson, Z. Chang, E. Judd, P.J. Schuck, R.W. Falcone, P.A. Heimann, H.A. Padmore, H.C. Kapteyn, P.H. Bucksbaum, M.M. Murnane, R.W. Lee, A. Machacek, J.S. Wark, X. Liu and B. Shan, Opt. Lett. **22**, 1012 (1997).

[129] Z. Chang, A. Rundquist, J.Zhou, M.M. Murnane, H.C. Kapteyn, X. Liu, B. Shan, J. Lui, L.Niu, M. Gong and X. Zhang, Appl. Phys. Lett. **69**, 133 (1996).

[130] R. Shepherd, R. Booth, D. Price, M. Bowers, D. Swan, J. Bonlie, B. Young, J. Dunn, B. White and R. Steward, Rev. Sci. Instrum. **66**, 719 (1995).

[131] M.M. Murnane, H.C. Kapteyn and R.W. Falcone, Appl. Phys. Lett. **56**, 1948 (1990).

[132] E. Constant, V.D. Taranukhin, A. Stolow and P.B. Corkum, Phys. Rev. A **56**, 3870 (1997).

[133] W.C. Wiley and I.H. McLaren, Rev. Sci. Instr. **26**, 1150 (1955).

Nederlandse samenvatting.

In de poging om de wereld om ons heen te begrijpen en uit dit begrip voorspellende modellen te distilleren gaat de natuurkundige onderzoeker meestal van de meest simpele situatie uit. Deze sterk vereenvoudigde situatie wordt dan opgelost en gaandeweg gecompliceerder gemaakt zodat het meer en meer op de echte (moeilijke) situatie gaat lijken. Voor het vinden van het antwoord op de vraag 'Hoeveel melk produceert een koe?' zal de natuurkundige zich de koe voorstellen als een bol die overal melk uitwazemt. Heeft hij eenmaal het antwoord op 'Hoeveel melk wazemt een bol uit?', dan perturbeert hij het systeem zodat de melk maar uit een deel van de bol wazemt; de bol poten krijgt en een koevorm, etc. Het antwoord zal het echte, experimentele, antwoord steeds beter benaderen.

Hetzelfde gebeurt in het begrijpen van de dynamica van de kleinste ondeelbare deeltjes, de atomen. Eerst probeert men de dynamica van het meest eenvoudige systeem, één proton met één elektron, ofwel het waterstof atoom, op te lossen. Een goed model is het proton voor te stellen als een positieve puntlading waar het negatief geladen elektron in banen omheen cirkelt. Klassiek gezien kan het elektron iedere willekeurige baan beschrijven net als een planeet om de zon. In de quantum mechanica, echter, wordt het elektron voorgesteld als golf. Voor een stabiele omloopbaan is, voor een golf, de *fase* belangrijk. Als namelijk de fase van de elektron golf bij het einde van zijn omloopbaan precies gelijk is aan de fase van het begin van de omloopbaan zal de elektron golf zichzelf versterken. Als de fase van de elektron golf bij het einde van zijn omloopbaan precies tegenovergesteld is aan de fase van het begin van de omloopbaan zal de elektron golf zichzelf uitdoven. Door het golfkarakter van het elektron zijn er dus alleen bepaalde, *gequantiseerde*, banen van het elektron om het proton mogelijk. Het is het makkelijkst dit te vergelijken met een touw aan de muur dat op en neer geslingerd wordt. Er ontstaat een staande golf met één of meerdere buiken. Hoeveel buiken je ook in het touw slingert, het is altijd een geheel aantal en nooit halftallig, de heeltallige versterken zichzelf, de halftallige doven zichzelf uit.

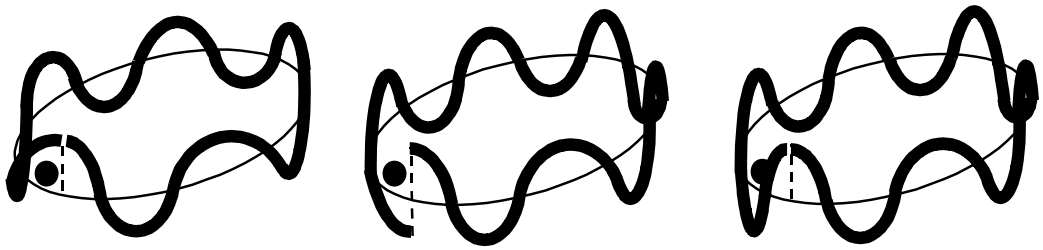

a. De fase aan het begin van de golf is gelijk aan de fase aan het eind van de golf.

b. De fase aan het begin van de golf is tegenovergesteld aan de fase aan het eind van de golf.

c. Door de faseverschuiving bij de kern is de fase aan het begin van de golf gelijk aan de fase aan het eind van de golf.

Hetzelfde geldt voor een gesloten lus van dat touw. In de bovenstaande figuur is dit uitgelegd. In het linker plaatje beschrijft het elektron een golfbeweging om de kern (de zwarte stip) waar de fase aan het eind van zijn omloopbaantje gelijk is aan de fase aan het begin. In deze baan met deze energie versterkt het elektron zichzelf en aldus geeft deze baan een *resonantie*. In het middelste plaatje komt de fase juist precies verkeerd uit en dooft het elektron zichzelf uit. Deze baan kan niet bestaan en op deze energie is dus geen resonantie.

De gequantiseerde elektronbanen van waterstof zorgen ervoor dat het emissie- of absorbtie spectrum van het element niet diffuus is maar uit lijnen bestaat wat Balmer al in 1885 zag. Rydberg heeft zijn en latere observaties geklassifiseerd en realiseerde zich dat de energie E_n van een energierijke elektron baan n algemeen beschreven kan worden als:

$E_n = E_{binding} - \frac{R}{2n^2}$

waar n het hoofd quantum getal is, $E_{binding}$ de bindings energie van het elektron aan het proton en R de Rydberg constante. Als n oneindig groot is, is $R/2n^2$ nul en dus is de energie van het elektron gelijk aan zijn bindings energie. Dit betekent dat het elektron vrij is en het atoom bestaat uit een ion en een vrij elektron. Als n een groot getal is, is het elektron zwak gebonden in een hoge baan en tenslotte, als n gelijk is aan 1, zit het in zijn laagste energietoestand, de grondtoestand, met energie nul. Het frappante van Rydbergs formule is dat het geldt voor ieder atoom, met een kleine aanpassing (van bol naar koe):

$E_n = E_{binding} - \frac{R}{2(n-\delta)^2}$

waar δ , het quantum defect, een constante is voor iedere serie binnen een atoomspectrum. De δ kan worden uitgelegd als een *faseverschuiving* van de elektrongolf bij de kern door interaktie met de binnenelektronen van het atoom. Deze faseverschuiving zorgt ervoor dat stabiele elektronbanen om atomen zich op ander energieën bevinden dan in waterstof. In de figuur beschrijft het elektron in het rechterplaatje dezelfde golf als die in het middelste plaatje maar omdat de golf sneller gaat bij de kern (de zwarte stip) is de fase aan het eind toch weer gelijk aan de fase aan het begin van de golf.

Tot nu toe hebben we het gehad over stabiele elektronenbanen in één gesloten kanaal. Een kanaal bestaat uit de hele set van stabiele elektronenbanen en het continuum daarboven waar het elektron niet langer gebonden is aan het ion. Als het elektron een stabiele baan beschrijft (negatieve energie), dan is het kanaal gesloten; als het elektron vrij is van het ion (positieve energie), dan is het kanaal open. De binnenelektronen van de kern zorgen naast een faseverschuiving ook voor een koppeling tussen verschillende kanalen. Zo kan een elektron na een baantje om de kern in een gesloten kanaal plotseling verstrooien naar een baan in een open kanaal, zodat het elektron ontsnapt.

Dit proefschrift is gewijd aan de dynamica van het aangeslagen elektron, ofwel de competitie tussen de aanwezige kanalen. De dynamica kan op twee manieren worden ontrafeld: Ten eerste door het meten van de energieën van de stabiele banen van het geëxciteerde elektron, de resonanties, en de energiebreedte van iedere resonantie. Hoe vaker de elektrongolf zijn omloopbaantje maakt, namelijk, hoe preciezer de energie van die baan gedefiniëerd is. De levensduur van een baan is dus omgekeerd evenredig met de energiebreedte van die baan. Ten tweede kunnen we het tijdstip meten wanneer een elektron precies verstrooit van een gesloten kanaal naar een open kanaal, ofwel, wanneer het elektron van het achterblijvende ion afvalt. Het probleem met deze metingen is dat de verstrooiing op superkorte tijdschaal gebeurt, in de orde van picoseconden (10^{-12} seconde). De verhouding van een picoseconde met een seconde is dezelfde als de verhouding van een seconde met bijna 32000 jaar. Voor het meten van elektronemissie op deze tijdschalen is de *streak camera* ontwikkeld.

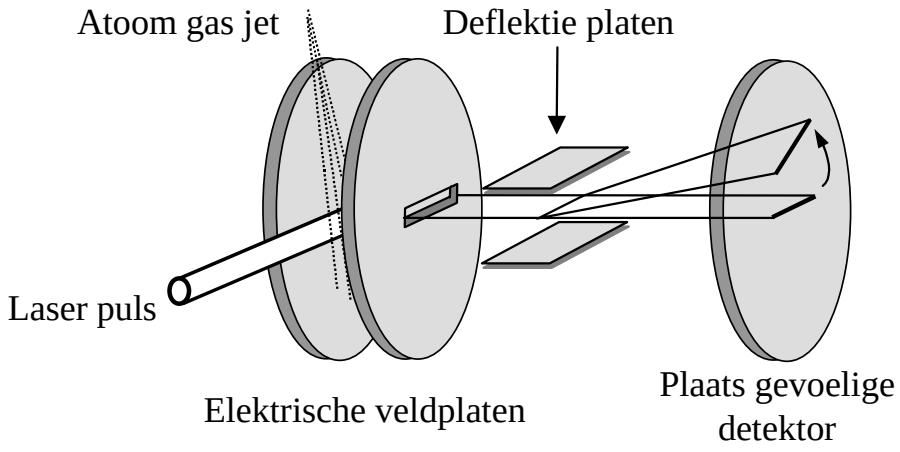

De werking van de streak camera is schematisch uitgelegd in de bovenstaande figuur. De laser puls exciteert de atomen tussen de elektrische veldplaten. De elektronen die ioniseren worden versneld richting de plaats gevoelige detector. In de baan van de elektronen staan twee deflektie platen waarvan het elektrische veld snel verandert van positief naar negatief. Dit deflektie veld buigt de elektronen naar boven of naar beneden, al naar gelang het teken van het deflektie veld. Op deze manier wordt de tijd dat een elektron langs komt vertaalt in een hoogte op plaats gevoelige detector.

Als de deflektieplaten maar snel genoeg veranderen kunnen we hoogteverschillen op de detector meten die corresponderen met een picoseconde. Net zoals het beeld van een snel bewegend objekt op een foto scherper wordt met een kortere belichtingstijd, leren we meer details van de dynamica van het hoogaangeslagen elektron als we op steeds kortere tijdschaal meten.

In het eerste deel van dit proefschrift wordt er gekeken naar de competitie tussen drie vervalskanalen in een molecuul: het elektron kan van het molecuul afgetrokken worden door een elektrisch veld, veldionisatie, óf de energie van het elektron wordt geabsorbeerd door de molecuulkern die vervolgens uitelkaar spat, predissociatie, óf het elektron krijgt juist (rotationele) energie van de molekuulkern zodat het elektron weggeschoten wordt, rotationele autoionisatie. In dit deel is de molecuulkern een 'harde pit' die alleen de eigenschap heeft dat het rotationele of vibrationele energie kan absorberen of doneren. In de competitie tussen de drie vervalskanalen blijkt de veldionisatie dominant: bij hoge energie wordt het elektron *altijd* door het veld van het molecuul getrokken en is er geen predissociatie of rotationele autoionisatie. De laatste vervalskanalen spelen alleen mee bij dieper gebonden elektronen. Het blijkt dat we achter de snelheid van het verval in alle drie kanalen kunnen komen door alleen het veldionisatie kanaal te meten.

In het tweede deel is de configuratie van de binnenelektronen om de atoomkern belangrijk. Het geëxciteerde elektron heeft interaktie met een binnenelektron die de dynamica flink verandert. Zo kan het binnenelektron energie geven aan het geëxciteerde elektron dat vervolgens van het atoom afgeschoten wordt. In dit deel meten we zowel in energie als in de tijd. Op korte tijdschaal zijn er allerlei afwijkende dingen te zien die op een grotere tijdschaal uitgemiddeld zouden zijn. Zo zien we bijvoorbeeld in hoofdstuk 5 in één geval dat het elektron *stapgewijs* van het achterblijvend (magnesium) ion afvalt na een korte laserpuls en in een ander geval dat het elektron *oscillerend* geëmiteerd wordt.

In het derde en laatste deel draaien we de situatie om: We bestuderen niet langer de atomen met een bekende laserpuls maar we meten deze laserpuls met het ons bekende gedrag van atomen. In de laatste twee hoofdstukken van dit proefschrift meten we de golflengte en de tijdsduur van een laserpuls in het verre ultraviolet met behulp van neon atomen. Het begrip van de atomen is zo ver gekomen dat we betrouwbaar aan hun gedrag kunnen zien wat voor laserpuls ze gekregen hebben, hoeveel energie daarin zat en hoelang deze puls duurde. En zo hebben we ons begrip uitgebreid van het eenvoudigste systeem van waterstof naar een willekeurig element onder invloed van een sterke lichtpuls. Er zijn vele interessante stappen tussen bol en koe.

Nawoord.

Promoveren is een hele goede tijd. Onderzoeksmogelijkheden zijn groot en het heeft tegelijkertijd nog een studentikoze vrijheid. Amolf is een unieke plek met een uitstekende ondersteuning en een goede sfeer. Mijn dank gaat uit naar mijn promotor Bart 'carsalesman' Noordam die vanaf het eerste moment dat ik op Amolf verscheen veel tijd aan mij besteed heeft en die uit alle mogelijke data publiceerbare resultaten wist te krijgen. Daarnaast natuurlijk wijlen mijn groep femtofysica met Kees 'boeien!' Wesdorp, Anouk 'met carnaval ben ik weg' Wetzels en Andreas 'well, in principle' Gürtler. De laatste heeft een dergemate afhankelijkheid van espresso veroorzaakt dat ik daar in ieder geval niet meer zonder kan. Medeverantwoordelijke aan de Lavazza terreur is Adrea 'Minka' Fera. Ik weet nog steeds het fijne niet van het 'grabing the concept and shaking it' gebaar. In de groep zijn vele gasten langsgekomen, waarvan Francis 'parallel brains' Robicheaux veruit de beste en prettigste contributie heeft geleverd. Veel goede samenwerking heb ik genoten van E&I, met name Dennis 'faster software' Driessen en Duncan 'faster hardware' Verheijde, de tekenkamer, de werkplaats, met vooral Jan 'zonder braampjes' van der Linde en laserspecialist Anton 'damagethreshold' Buyserd. Niets was mogelijk geweest zonder de technische ondersteuning van Rob 'ruim dat op' Kemper en vooral Hinco 'motor stuk' Schoenmaker. Hinco heeft alle losse eindjes van het Technobase project verbonden, maar dan ook echt alle.

De tijd als voorzitter van de personeelsvereniging van Amolf was een heel leuke en leerzame, bedankt Paul, Jan, Thea, Christiaan, Ad, Marco, Igor en Arjan. Ik ben blij te zien dat de PV nog steeds een aktieve koers vaart.

En natuurlijk bedank ik iedereen die bezig is of is geweest, binnen de muren van het FOM instituut (vrij naar 'friend of Amolf' Richard 'folks' Thomas), vooral de groepsleden en groepsleiders binnen de atoomfysica, voor een goede en fijne collegialiteit. Ook in minder goede tijden waren er velen tot steun. Daarbuiten had ik veel aan mijn familie en vrienden, die voor de nodige afwisseling zorgden.

Als laatste maar eigenlijk belangrijkste wil ik Stasia bedanken; voor je steun, je uithoudingsvermogen en je liefde.

Marcel Warntjes, maart 2001.

All's well that ends.